

# The use of colour-magnitude diagrams in studies of low-mass star formation

Benjamin G. Burningham

Submitted by Benjamin G. Burningham, to the University of Exeter as a thesis for the degree of Doctor of Philosophy in Physics, October 2005. This thesis is available for Library use on the understanding that it is copyright material and that no quotation from the thesis may be published without proper acknowledgment. I certify that all material in this thesis which is not my own work has been identified and that no material has previously been submitted and approved for the award of a degree by this or any other University.

Signed: .....  
(Benjamin G. Burningham)

Date: .....

# Abstract

The use of colour-magnitude diagrams (CMDs) has been central to the study of stellar evolution since the first time such a diagram was plotted. Today, nearly one hundred years later, their use is still as fundamental to uniting theory with observation as it was then. In this thesis the use of CMDs in the study of PMS evolution and star formation is explored.

By combining archival X-ray data with *VI* CMDs low-mass PMS stars are identified in Vela OB2 and the young cluster Collinder 121 (Cr 121). In the latter of these, the number and location of the PMS stars on the CMD in conjunction with models of PMS evolution are used to help resolve a long standing controversy over the nature of Cr 121. Cr 121 is confirmed as a young cluster at a distance of just over 1 kpc.

The use of CMDs for selecting unbiased samples of low-mass PMS stars in OB associations is then explored. Radial velocities are used to assess membership of the  $\sigma$  Orionis young group across a sample drawn from a broad region of colour-magnitude space. It is found that samples selected from the expected PMS region of an *RI* CMD along this sight-line will not exclude significant numbers of bona-fide association members that fall outside the selection region. It is also found that such selections will not be subject to severe contamination by non-members at magnitudes brighter than  $I = 17$ .

Finally, simulations on *RI* and *VI* CMDs are used to assess the importance of photometric variability on timescales of 1-4 years, binaries and photometric uncertainty in the production of apparent age spreads on the CMDs of 2 OB association-like environments: the  $\sigma$  Orionis young group and the Cep OB3b association. It is found that such effects can account for about half of the observed spread in the case of the  $\sigma$  Orionis young group, but only about one twentieth of the observed spread in the Cep OB3b association.

# Acknowledgments

## For support and guidance

Firstly I'd like to thank my family for reminding me that madness is relative. I would also like to thank my dear Katie for helping me through many of the interesting times that post-graduate study can bring. Obviously, my supervisor, Tim Naylor, has my gratitude for guiding me through this PhD and being understanding of my sometimes slow progress. I would like to thank Rob Jeffries for numerous useful comments and suggestions regarding much of this thesis. A huge 'thank you' goes to Dr Alasdair Allan for his constant assistance with my endless computer problems, and patience in the face of my ridiculous ignorance of all things Unix. The comments and suggestions made by the anonymous referees on each of the papers that have been published from work in this thesis have had a significant impact on its quality. So, thank you, whoever you are.

## For data

Rob Jeffries and Tina Devey obtained the data used in Chapters 2 and 3 at Cerro Tollo Inter-american Observatory, Chile, which is operated by the Association of Universities for Research in Astronomy, Inc., under contract to the US National Science Foundation. I thank Nigel Hambly for useful comments regarding the use of proper motions from the SuperCosmos sky surveys, and Mike Watson for alerting us to the existence of the XMM-Newton data for WR 6 and S308. The research presented in this thesis made use of *ROSAT* data obtained from the Leicester Database Archive Service at the Department of Physics and Astronomy, Leicester University, UK; of the SIMBAD database operated by the Centre de Données Astronomiques (Strasbourg, France). I obtained the optical photometry of Cep OB3b and  $\sigma$  Orionis at the Isaac Newton Telescope (INT) with the assistance of Tim Naylor. The second epoch data for Cep OB3b were obtained by Stuart Littlefair and Eric Saunders. The spectra of targets near  $\sigma$  Orionis were obtained using AF2/WYFFOS fibre spectrometer on the William Herschel Telescope (WHT). Configuration files for AF2/WYFFOS were compiled by Stuart Littlefair, who also obtained first night's observations with Tim Naylor. The second night's observations were carried out by myself and Tim Naylor. The WHT and INT are operated on the island of La Palma by the Isaac Newton Group in the Spanish Observatorio del

Roque de los Muchachos of the Instituto de Astrofísica de Canarias. The astrometry in Chapters 2 and 3 made use of catalogues obtained from the SuperCosmos sky survey, operated by the Wide Field Astronomy Unit, Institute of Astronomy, Royal Observatory, Edinburgh. The astrometry described in Chapter 5 utilised the Two Micron All Sky Survey, which is a joint project of the University of Massachusetts and the Infrared Processing and Analysis Center/California Institute of Technology, funded by the National Aeronautics and Space Administration and the National Science Foundation.

# Contents

<b>Abstract</b> . . . . .	<b>2</b>
<b>Acknowledgments</b> . . . . .	<b>3</b>
<b>1 Introduction</b> . . . . .	<b>9</b>
1.1 The birth of the most powerful plot in modern astronomy . . . . .	12
1.2 Colour-magnitude diagrams and the modern theory of stellar evolution . . . . .	19
1.3 An overview of low-mass star formation . . . . .	25
1.4 PMS evolution and the H-R diagram . . . . .	30
1.5 Identifying PMS stars . . . . .	35
1.5.1 H $\alpha$ emission . . . . .	37
1.5.2 X-ray emission . . . . .	38
1.5.3 Lithium absorption . . . . .	39
1.5.4 Kinematic methods . . . . .	40
1.6 OB associations . . . . .	43
<b>2 Investigation of a comparison field for the <math>\gamma</math> Velorum cluster</b> . . . . .	<b>46</b>
2.1 Introduction . . . . .	46
2.2 Optical Data . . . . .	47
2.2.1 Observations . . . . .	47
2.2.2 Data Reduction and Optimal Photometry . . . . .	47
2.2.2.1 Finding the offsets between the frames . . . . .	49
2.2.2.2 Object Detection . . . . .	50
2.2.2.3 Optimal photometry . . . . .	52
2.2.2.4 Final stages . . . . .	53
2.3 X-Ray Data . . . . .	61
2.4 Identification of X-ray sources . . . . .	63
2.5 Discussion . . . . .	63
2.6 Conclusions . . . . .	66
<b>3 On the nature of Collinder 121: insights from the low-mass pre-main sequence</b> <b>67</b>	<b>67</b>
3.1 Introduction . . . . .	67
3.2 Optical data . . . . .	69
3.2.1 Observations . . . . .	69
3.2.2 Data reduction and optimal photometry . . . . .	71
3.3 X-Ray data . . . . .	74
3.3.1 ROSAT data . . . . .	74
3.3.2 XMM-Newton data . . . . .	74
3.4 Identification of X-ray sources . . . . .	78
3.4.1 Cross-correlation of optical and X-ray source lists . . . . .	78
3.4.2 Inferred X-ray Luminosities . . . . .	80
3.4.3 Investigation of the proper motions of the X-ray selected PMS candidates . . . . .	80
3.5 Discussion: how far away and how old are the PMS stars? . . . . .	85
3.6 Conclusions . . . . .	89
<b>4 Contamination and exclusion in the <math>\sigma</math> Orionis young group.</b> . . . . .	<b>90</b>
4.1 Introduction . . . . .	90
4.2 Optical spectroscopy using AF2/WYFFOS . . . . .	94
4.2.1 Target selection . . . . .	94
4.2.2 Observations . . . . .	94

4.3	Data reduction . . . . .	98
4.3.1	Extraction of spectra . . . . .	98
4.3.2	Telluric correction and sky subtraction . . . . .	100
4.4	Selecting members by radial velocity . . . . .	103
4.4.1	Sample selection . . . . .	103
4.4.2	Cross correlation of spectra to obtain radial velocities . . . . .	104
4.4.3	Membership probabilities . . . . .	108
4.5	Discussion . . . . .	109
4.5.1	Are there members outside the “PMS” region? . . . . .	109
4.5.2	Contamination within the “PMS” region . . . . .	112
4.6	Conclusions . . . . .	115
<b>5</b>	<b>Can variability account for apparent age spreads in OB association colour-magnitude diagrams?</b> . . . . .	<b>117</b>
5.1	Introduction . . . . .	117
5.1.1	Slow star formation . . . . .	117
5.1.2	Rapid star formation . . . . .	118
5.1.3	Age spreads . . . . .	118
5.1.4	PMS variability . . . . .	121
5.1.5	PMS binaries . . . . .	122
5.2	Observations and data reduction . . . . .	123
5.3	Simulation of photometric spreads . . . . .	125
5.3.1	The $\sigma$ Ori subgroup . . . . .	125
5.3.2	Cep OB3b . . . . .	133
5.4	Discussion . . . . .	140
5.4.1	The nature of the variability . . . . .	141
5.4.2	Apparent age spread and absolute age . . . . .	144
5.5	Conclusions . . . . .	144
<b>6</b>	<b>Conclusions</b> . . . . .	<b>145</b>
6.1	Discussion and conclusions . . . . .	145
6.2	Future work . . . . .	147

## List of Figures

1.1	Fig. 1.1	10
1.2	Fig. 1.2	15
1.3	Fig. 1.3	17
1.4	Fig. 1.4	22
1.5	Fig. 1.5	23
1.6	Fig. 1.6	26
1.7	Fig. 1.7	27
1.8	Fig. 1.8	32
1.9	Fig. 1.9	36
1.10	Fig. 1.10	42
2.1	Fig. 2.1	48
2.2	Fig. 2.2	54
2.3	Fig. 2.3	54
2.4	Fig. 2.4	56
2.5	Fig. 2.5	58
2.6	Fig. 2.6	64
2.7	Fig. 2.7	65
3.1	Fig. 3.1	70
3.2	Fig. 3.2	79
3.3	Fig. 3.3	79
3.4	Fig. 3.4	82
3.5	Fig. 3.5	87
3.6	Fig. 3.6	88
4.1	Fig. 4.1	95
4.2	Fig. 4.2	96
4.3	Fig. 4.3	102
4.4	Fig. 4.4	102
4.5	Fig. 4.5	110
4.6	Fig. 4.6	110
4.7	Fig. 4.7	111
4.8	Fig. 4.8	114
5.1	Fig. 5.1	127
5.2	Fig. 5.2	128
5.3	Fig. 5.3	130
5.4	Fig. 5.4	132
5.5	Fig. 5.5	133
5.6	Fig. 5.6	135
5.7	Fig. 5.7	136
5.8	Fig. 5.8	137
5.9	Fig. 5.9	139
5.10	Fig. 5.10	140
5.11	Fig. 5.11	142
5.12	Fig. 5.12	142

## List of Tables

2.1	Table 2.1	49
2.2	Table 2.2	59
2.3	Table 2.3	60
2.4	Table 2.4	62
3.1	Table 3.1	71
3.2	Table 3.2	73
3.3	Table 3.3	76
3.4	Table 3.4	77
3.5	Table 3.5	83
3.6	Table 3.6	84
4.1	Table 4.1	98
4.2	Table 4.2	105
4.3	Table 4.3	106
5.1	Table 5.1	127

# 1 Introduction

The twentieth century witnessed tremendous progress in the formulation of a quantitative understanding of stellar evolution. It was the marriage of theoretical physics with observational astronomy that led this progress. This occurred first when gas laws were applied to stellar models, and culminated with the identification of the energy source for stars. Central to this process was the ability to compare theoretical predictions with the observable properties of stars.

The simplest observations that can be made of a star are its colour and its brightness. These can be plotted against each other in a colour-magnitude diagram (CMD). The analogue of a CMD in the theoretical plane is the Hertzsprung-Russell (H-R) diagram, which plots luminosity against effective temperature. It was these diagrams, constructed for large samples of stars, that provided the observational basis for theories of stellar evolution. As will be discussed later, when the first diagrams of this kind were plotted they immediately influenced the dominant theories of the day.

Figure 1.1 shows a schematic of the H-R diagram for a sample of stars at a range of ages. The line labelled main-sequence is now known to represent a line of hydrostatic equilibrium for hydrogen burning, when the pressure created by energy release in the core supports the stellar atmosphere against its own weight. The various other populations labelled on this plot represent different post-main sequence evolutionary states for different mass stars. A star's main-sequence life ends when it has consumed all the hydrogen in its core, and it ceases to be in hydrostatic equilibrium. A star's main-sequence life begins when it first reaches hydrostatic equilibrium as a result of core hydrogen fusion. This is when it arrives on the zero-age main sequence (ZAMS). Prior to this it is called a pre-main sequence (PMS) star, and it is the study of these objects on CMDs that will be the subject of this thesis.

As a PMS star ages, it moves across the H-R diagram toward the ZAMS. The nature of this progression will be discussed later in this chapter. For the time being it is sufficient to say that a PMS star is over-luminous for its temperature as compared to the ZAMS. The younger the PMS star, the more over-luminous it is. As such, a group of coeval PMS stars will be distributed to the right of the ZAMS on a H-R diagram or CMD. This property allows candidate PMS stars to be identified by their location on such a diagram. The confidence in such identifications may

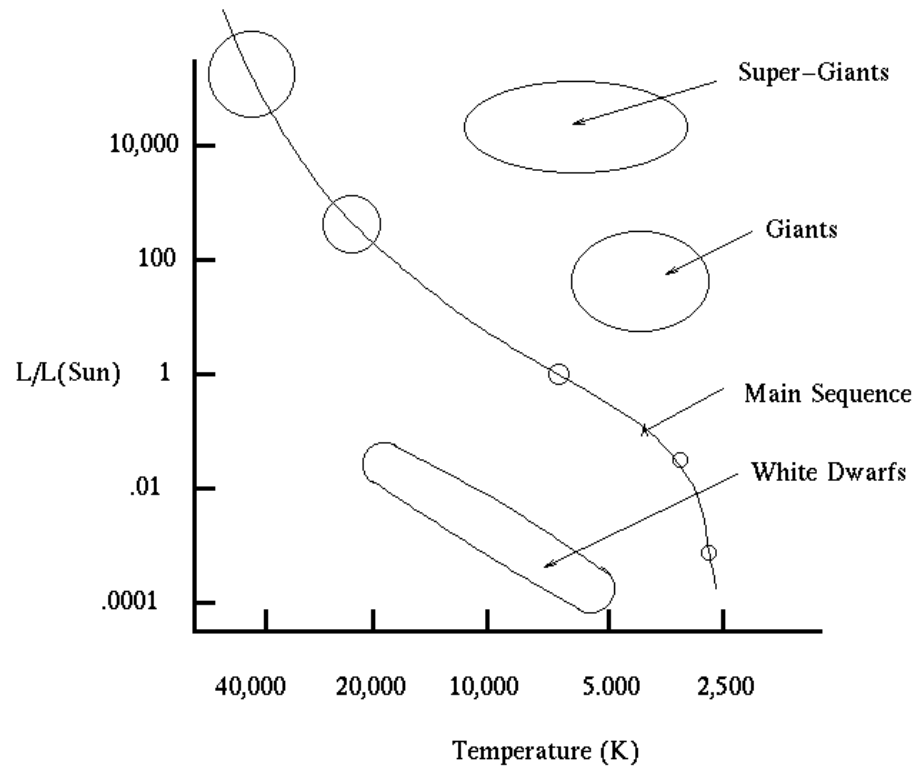


Figure 1.1: A schematic of a H-R diagram for a large number of stars at a range of ages. Taken from website URL:<http://zebu.uoregon.edu/~imamura/208/jan23/hr.html>.

be improved by combining this information with ancillary corroborating evidence, examples of which will be discussed later. By studying the distribution and location of PMS stars on a CMD, information regarding the age and distance of young groups of stars may be obtained. The CMD may also be used in the selection of samples for studying fundamental problems in star formation, such as measuring the initial mass function (IMF) or obtaining star formation histories.

This thesis will demonstrate that the CMD remains one of the most powerful tools for answering questions of stellar evolution, specifically those regarding the origins of stars. The remainder of the introduction will explore the early history of the H-R diagram, and how its use helped shaped the theories of the day. This will be followed by a brief overview of the earliest stages in the life of a low-mass star up to its emergence as a PMS star. The progress of a PMS star across the H-R diagram towards the ZAMS will then be described, and this chapter will conclude with a brief discussion regarding the different methods of identifying PMS stars.

Chapter 2 describes a short project in which X-ray data was used to identify likely PMS stars in the direction of the Vela OB2 association. The motivation for this work was to provide a control field to assess the significance of the discovery by Pozzo et al. (2000) of a group of PMS stars in the vicinity of  $\gamma$  Velorum. The number of PMS stars identified in this control field supports the suggestion that the PMS stars identified by Pozzo et al. (2000) represent a cluster centered on  $\gamma$  Velorum. The same technique is used again in Chapter 3 to identify candidate PMS stars, which trace the locus of a PMS along a sight-line towards Collinder 121 (Cr 121). In this case, the CMD is not only used to identify low-mass PMS stars, but also to discern their distance and age. By considering the higher mass stellar membership of the groups along this sight-line, and the number and distribution of low-mass PMS objects on the CMD, it is argued that Cr 121 is a compact young cluster at a distance of just over a kilo-parsec.

The latter part of the thesis concentrates on how CMDs can be used in the study of key questions in star formation. One of the great potential uses for the CMD in the study of star formation is that of selecting samples of PMS stars when constructing the IMF for young clusters and OB associations. However, before a sample of PMS members of a group can be selected by location on a CMD the degree of contamination within the selection region by non-members, and the number of members that lie beyond said region must be estimated. In Chapter 4 radial velocities are used to identify likely members and non-members of the  $\sigma$  Orionis young group in

a sample drawn from a broad region of an *RI* CMD. It is found that a sample selected from the expected PMS region of the CMD would not be subject to significant contamination, nor would it exclude a significant number of members. As part of this project the use of the Na I doublet at 8183,8195 Å as a two-pronged diagnostic for very low-mass PMS stars and brown dwarfs was investigated. The two ways in which this doublet can be used are: a) for deriving radial velocities; b) as a low-gravity indicator as the strength of the Na I absorption is gravity sensitive.

In Chapter 5 the focus moves away from sample selection and we consider the CMD's role in answering another key question of star formation. One of the significant unanswered questions in star formation is how long it takes. The presence of age spreads in young clusters and associations has been used as a key piece of evidence on both sides of a debate as to whether star formation is a rapid or slow process. The majority of observed age spreads are in fact, in their raw form, spreads in colour-magnitude space. Such spreads could arise as a result of a number of other factors, one of which is photometric variability. The results of Chapter 4 are used to make a photometric selection of PMS objects in the  $\sigma$  Orionis young group. By using 2 epoch observations of this sample and a sample of PMS objects in the Cep OB3b association the influence of photometric variability on the extent of the observed spreads on CMDs is assessed. The final chapter contains a discussion of the key results obtained in this thesis, and a description of future lines of enquiry that have been opened up by the projects described here.

## 1.1 The birth of the most powerful plot in modern astronomy

It is widely accepted that the Hertzsprung-Russell (H-R) diagram represents one of the most powerful syntheses of modern astronomy. The H-R diagram relates the luminosity of stars to their effective temperature, and was arrived at through the efforts of a number of astronomers in the early 20th century, including Ejnar Hertzsprung and Henry Russell. Also fundamental to this was the timely recognition that the differences in the spectra of stars could not be explained simply by varying chemical abundances. This was apparent in the continuous nature of the spectral type sequencing compared to the complexity of the optical spectra of atoms, now being understood in terms of Bohr's theory of spectra (Bohr, 1913). This provided the theoretical motivation for

identifying which stellar parameters were responsible for the continuous progression of optical spectra from early to late spectral types. This realisation, that the key quantities that determined the spectral type of a star were pressure and effective temperature, was crucial to the advancement of stellar astrophysics.

Shortly after 1895, whilst working under Pickering at Harvard, Annie Cannon was the first to order the spectra of stars into the sequence of spectral types that we use today. She sequenced them such that the changes were continuous with respect to nearly all lines, rather than sequenced by the strength of the hydrogen absorption lines (North, 1994). It became apparent that the change in the spectra was mirrored by a change in colour, and there was a strong suspicion that this reflected a change in temperature<sup>1</sup>. It was thought that the stars shone from gravitational contraction, and would cool over their lifetimes. So it made sense that those spectral types which corresponded to the bluest and thus youngest stars should be referred to as the early-types and those that corresponded to the reddest stars should be referred to as the late-types. It was also widely held at that time that stars might be expected to dim as they cooled, and such speculation motivated astronomers to try and relate the colours of stars to their intrinsic radiance. The greatest hurdle to such studies was the problem of obtaining reliable parallaxes for a sufficient number of stars. As a result a great proportion of the astronomical endeavour of the late nineteenth and early twentieth century was concerned with this problem.

In the late nineteenth century a number of astronomers had attempted to investigate the problem of stellar evolution through the use of spectral types, proper motions and parallaxes. In particular Monck (1892, 1895, 1898) identified that, on the whole, stars of earlier spectral type had smaller proper motions than those of later type. However, Monck had relatively few stars of late-type with known proper motions, and when the spectral types were listed in the order of their inferred brilliance (B,A,K,M,F,G; Monck, 1898), it contradicted the continuous sequence, and the current evolutionary paradigm. In addition to making one of the first attempts to find correlations between luminosity and spectral type, Monck also suspected the existence of two classes of later type star, “one dull and near us and the other bright and remote” (Monck, 1895). However, his

---

<sup>1</sup>That the different spectral types of stars were due to a temperature sequence, however, was not confirmed until 1921, through the application of Saha’s equation for ionisation in stellar atmospheres to the observed lines strengths in stellar spectra.

sample did not contain any faint M-type stars with known proper motions, and he did not trust the parallaxes of the time (Nielsen, 1963). As a result this discovery passed over Monck, and had to wait until good quality parallaxes were available for more stars.

This was not very long in coming: in 1905 and 1907, Ejnar Hertzsprung published tabulated data on the spectral types and luminosities of nearby stars that had well determined parallaxes, deriving his work from data that had already been published by other astronomers. He published these works in the *Zeitschrift für wissenschaftliche Photographie* (Journal of Scientific Photography), and these discoveries went nearly unnoticed by the astronomical community until they were republished in *Astronomische Nachrichten* in 1909. In these classic works he noted similar trends and correlations to those found by Monck, including the existence of two classes of stars, the giants and the dwarfs. This time, however, the sequencing of the spectral types in terms of brilliance matched the continuous sequence that had been arrived at by Annie Cannon. His subsequent work concentrated more on photometry, and spectrophotometry, utilising photographic plates he had taken using telescopes at Copenhagen, Urania-Observatory, Göttingen and Potsdam to obtain effective wavelengths and magnitudes. Hertzsprung had taken these plates with a diffraction grating placed in the optical path, such that each image of a star also had a crude spectrum associated with it. This was used to find the wavelength of peak brightness, which was referred to as the effective wavelength. It is not clear when he first started to plot data of this sort graphically, but certainly by 1908 he had a working version of a diagram, relating effective wavelength to magnitude for the Pleiades (Tassoul & Tassoul, 2004). Even so, it was not until 1911 that such a diagram was published, along with diagrams for the Hyades, Praesepe and the Coma Berenices cluster (Hertzsprung, 1911). This paper represents the first publication of a colour-magnitude diagram (CMD). Figure 1.2 shows Hertzsprung's CMDs for the Hyades and the Pleiades published in his paper of 1911.

At around the same time as Hertzsprung was constructing his first CMDs, Henry Russell was involved in a programme to obtain parallaxes for a large number of stars. In a paper of 1910 he published more than 50 new parallaxes, and equipped with new spectral types courtesy of Pickering and Cannon at Harvard, noted the relation between spectral type and absolute magnitude, and the existence of two luminosity classes of late type stars (Russell, 1910). At the time of writing this paper it would seem that Russell was unaware of the work that had been carried out on the other

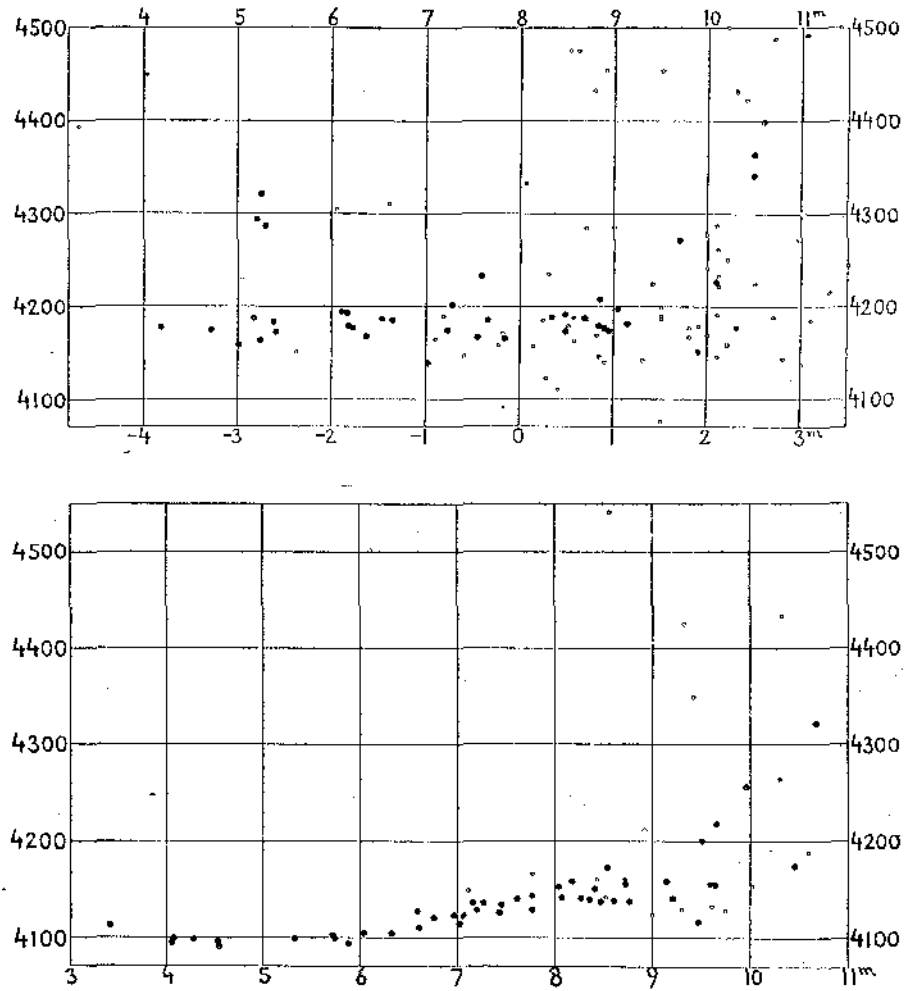


Figure 1.2: Hertzsprung's magnitude-effective wavelength diagrams for the Hyades (top) and the Pleiades (bottom). The abscissa for the Hyades plot are apparent magnitude (top) and absolute magnitude (bottom), and for the Pleiades it is just apparent magnitude. The ordinate axis in both cases is the effective wavelength in Ångströms (Hertzsprung, 1911).

side of the Atlantic relating the colours of stars to their intrinsic brightness. In the summer of 1910, a colleague of Hertzsprung's, one Karl Schwarzschild, attended a meeting of the Astronomical and Astrophysical Society of America at Harvard. It was at this meeting, where Russell presented his paper on parallaxes, that Russell first became aware of Hertzsprung's efforts, and he was soon supplied with reprints of Hertzsprung's work (Nielsen, 1963). Although Hertzsprung published his first CMD in 1911, it was not until June 1913 that Russell presented his first spectral type versus absolute magnitude diagram (Figure 1.3), at a meeting of the Royal Astronomical Society in London (Russell, 1913).

Both Hertzsprung and Russell interpreted the existence of two classes of late-type star in terms of evolutionary sequences, but in quite different ways. Hertzsprung interpreted the two sequences as two distinct series of evolution, one more luminous than the other. In both series the stars collapse from nebulae to form hot blue early stars, which then cool through the colour sequence to become red, late stars, and finally dim to extinction. This sequencing of evolution had its roots in the ideas of Zöllner, who proposed in 1865 that stars begin life as gaseous planetary nebulae, which then contract and cool to become hot young, blue, stars, which were believed to be liquid spheres with solid crusts (Tassoul & Tassoul, 2004). This was a purely phenomenological picture of stellar evolution. On the other hand, Russell's interpretation bore more resemblance to the evolution proposed by the likes of A. Ritter and Norman Lockyer.

Ritter (1883) had proposed a model for stellar evolution which was entirely rooted in theoretical considerations of the gas laws<sup>2</sup>. Within this model the evolution of a star could be considered as consisting of three principal stages. Initially the gravitationally contracting star is of sufficiently low density that it is essentially transparent to radiation. As such the luminosity increases with the temperature as the star contracts. During the second phase the opacity of the stellar gas is much higher, and Ritter now considered it as a sphere of ideal gas in convective equilibrium. As such the previously large red star dims as it continues to contract and becomes a small, hot, blue star. Ritter's model then requires the star to cease behaving as a perfect gas at some point, and the star enters the third phase of its evolution. During this phase the temperature of the star falls, so that the once hot, small, blue star cools and dims to a small, cool, red star and eventually

---

<sup>2</sup>A translation of this work was published in *Astrophysical Journal* in 1898 (Ritter, 1898)

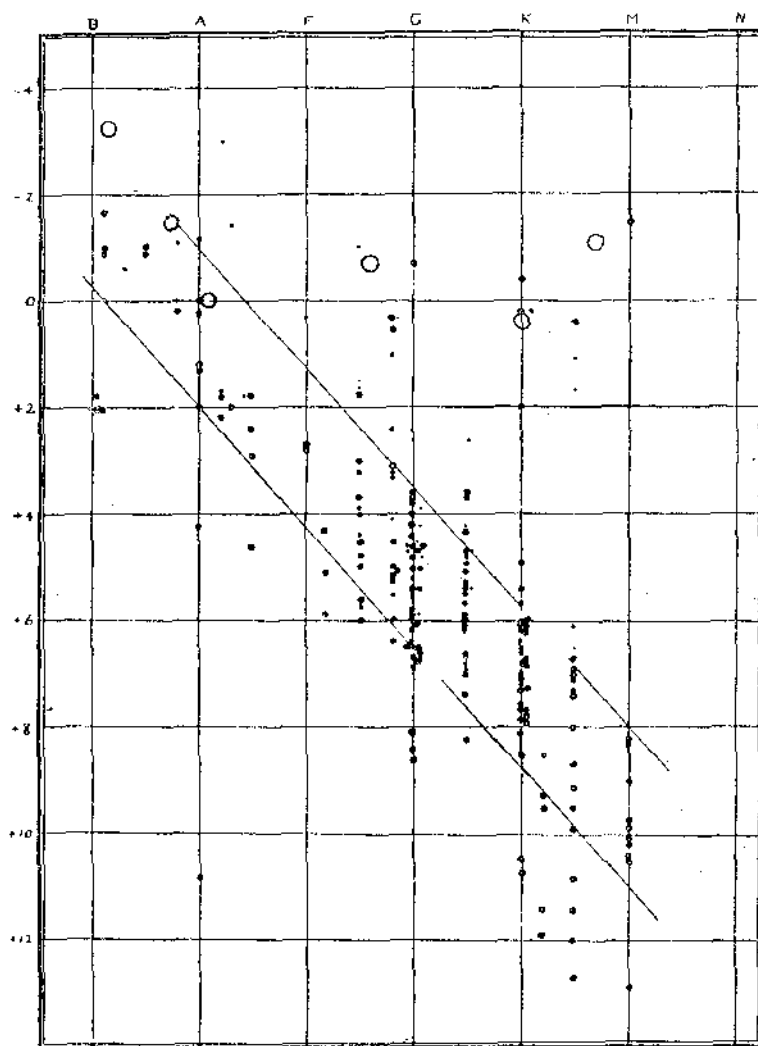


Figure 1.3: Henry Russell's first diagram plotting spectral types in the Harvard system on the abscissa and absolute magnitudes on the ordinate axis. The different symbols denote different quality parallaxes: large circles denote parallaxes with an uncertainty of less than 42%; small circles denote larger uncertainties; filled circles denote stars with multiple parallax determinations; open circles denote stars with single determinations (Russell, 1913).

becomes extinct. An interesting feature of Ritter's model, in the light of modern thinking, is that he connected the mass of a star to its maximum temperature with only the most massive stars achieving the highest temperatures. At around the same time Sir Norman Lockyer proposed a theory of stellar evolution that closely resembled that of Ritter, with two main differences (Lockyer, 1887). Firstly Lockyer held that all stars follow the same evolutionary path, regardless of their mass. Secondly Lockyer's theory incorporated within it an explanation as to the initial formation of stars. Like many of Lockyer's ideas, this one was, in many ways, far ahead of its time.

Lockyer (1887) proposed that stars form from the condensation of meteor swarms under gravity. As a swarm collapses, the heat generated by collisions within the distended young star causes its temperature to rise, and its colour to change slowly from red to blue. As the temperature rises the meteors are vapourised and dissociated into proto-elements<sup>3</sup>. Once the meteoritic material is vapourised, the heating due to collisions no longer heats the contracting star, and it begins to cool from blue to red, and eventually ceases to shine. As such Lockyer attempted to identify two types of red star, those that were contracting and heating (the giants), and those that were cooling (the dwarfs). His method, which proved unsuccessful, was to study minor details in their spectra (Nielsen, 1963).

In his paper of 1887 Lockyer noted many similarities in the spectra of meteors and comets when compared to the spectra of some late-type stars and some novae. He concluded that these stars were "not masses of vapour like our Sun, but clouds of incandescent stones", and represented "the first stage of meteoric condensation" (Lockyer, 1887). This so-called giant-and-dwarf theory of stellar evolution was widely opposed when it was first suggested, not least because the cold starting point seemed a needless complication, for which there was little credible evidence at the time. On the other hand, the prevailing theory of the day, that based on the ideas of Zöllner, had the sequencing of spectra and colours to support it.

The publication of Hertzsprung's and Russell's results in 1911 and 1913 proved to be a huge boost for the giant-and-dwarf theory of stellar evolution. The recognition by Russell (1914) that

---

<sup>3</sup>Another of Lockyer's great ideas was his dissociation hypothesis. Lockyer (1878b,a) proposed that at the high temperatures in stellar atmospheres, atoms would break down to become what he termed "proto-elements". This was the term he used to describe the originators of the many unidentified lines seen in the spectrum of the Sun. This insight is particularly impressive when one considers that at the time the atom was considered indestructible, and it was not until the 20th Century that the proto-elements were identified as ionised metals.

the average mass of the bluest stars was much higher than that of the redder type stars led him to re-iterate the suggestion by Ritter (1883) that the maximum temperature achieved by a star was determined by its mass, with only the most massive achieving spectral types A and B. This result also seriously damaged the case for the previously accepted theory, as it required stars to lose a great deal of mass as they cooled.

The final nail in the coffin of the previously accepted theory came from observations of eclipsing variable stars. The work of Shapley (1913) demonstrated that whilst nearly all the early-type stars observed had high density, the later type stars could be divided into two groups, those with density similar to the Sun, the dwarfs, and those with much lower density, the giants. Russell (1914) cited this as evidence that the giants were in a more primitive state, as expected by the giants-and-dwarfs theory. The proponents of the ideas of Zöllner were unable to incorporate these observations into their theory.

The old idea of a hot birth and a cool death for stars had been superseded by the new theory of a cold birth and cold death. The diagrams produced by Hertzsprung and Russell had played a key role in this change. However, this is not the revolution in stellar astrophysics with which the H-R diagram is usually credited. Indeed, it was soon to be shown that Russell's ideas on stellar evolution were fatally flawed, and a key tool in the continuing study of stellar evolution were the diagrams that Hertzsprung and Russell and pioneered.

## 1.2 Colour-magnitude diagrams and the modern theory of stellar evolution

Nearly ten years after Russell had published his first diagram, cracks were starting to show in his dwarf-and-giant model of stellar evolution. In 1922 Hertzsprung published data on 734 mostly northern hemisphere naked eye stars, which, for the first time, facilitated a more detailed investigation of the upper part of the H-R diagram (Hertzsprung, 1922). What was revealed was a dearth of stars in the region between the main sequence and the giant sequence. This region, now known as the Hertzsprung Gap, did not fit with the hitherto accepted giant-and-dwarf theory. For Russell's theory to survive, it required that the evolution across this region of the H-R diagram proceed very rapidly, so as to explain why few stars were observed there. This was an idea that

Hertzsprung was not terribly comfortable with (Waterfield, 1956).

If the identification of the Hertzsprung Gap had badly injured Russell's theory, it was the derivation by Eddington (1924) of the mass-luminosity relation for stars that finally buried it. Eddington's relationship between mass and luminosity assumed the star behaves as a perfect gas, an assumption which fitted well with the giant stage in Russell's stellar evolution. Recall that according to the giant-and-dwarf theory it is the departure from the perfect gas behaviour at very high densities that defines the transition from collapsing giant to static, cooling dwarf. Already studies of the masses and absolute magnitudes of stars in binary systems had given results that were hard to reconcile with this transition.

Both Russell et al. (1923) and Hertzsprung (1923) had found that both giant stars and dwarf stars appeared to form part of the same sequence when their masses were plotted against their absolute magnitudes. Whilst Russell interpreted this in terms of a statistical relation between the masses and absolute magnitudes of binary systems, Hertzsprung, who was already uneasy about the merits of the giant-and-dwarf theory (Waterfield, 1956), passed his data on to Eddington. Eddington (1924) re-plotted the data of Hertzsprung (1923) along with data from his own observations, and found that his relation could correctly predict the absolute magnitude of all the stars included in his test, regardless of giant or dwarf classification. He concluded that "under stellar conditions matter should be able to contract to an enormously high density before deviations from the laws of perfect gas become appreciable". The conclusion was that the decreasing luminosity that is observed as one moves from early to late type stars on the main sequence is due to decreasing mass, rather than decreasing compressibility, as was suggested by Ritter's theory. Thus, if it was to be assumed that the mass of a star remains the essentially the same for its lifetime, the old interpretation of the H-R diagram would have to be abandoned. Although Eddington accepted that the current sequence of evolution of a star on the H-R diagram could be saved if it was assumed that a star "burns itself away in liberating sub-atomic energy", the core assumptions of the associated theory were now untenable. Eddington could not offer a new explanation for the form of the H-R diagram, but he correctly identified that this would have to wait for an understanding of the energy source of the stellar interior (Eddington, 1924).

In the years following the publication of the first H-R diagrams a number of other astronomers began constructing similar diagrams for a wider selection of clusters. Of particular note was Harlow

Shapley, who published a series of 17 papers on the subject of stellar clusters between 1917 and 1921. His CMDs demonstrated the difference in populations between globular clusters and open clusters (Shapley, 1917a). They also showed differences between open clusters, with some showing an absence of bluer stars (Shapley, 1917b). Whilst Shapley's work focused predominantly on globular clusters, and in particular determining their distances, the seminal works on the classification of open clusters using H-R diagrams were to be written by Robert Trumpler.

In Trumpler's 1925 paper, 52 open clusters were investigated and classified by the forms of their H-R diagrams. Figure 1.4 shows Trumpler's diagram that illustrated his original classification scheme. The classification scheme used two principal classes based on whether or not giant stars were present in the cluster. Those without giants were type 1, whilst those which contained giant stars were type 2. These two classes were then subdivided based on the spectral type of the brightest dwarf stars. What Trumpler found was that there existed only certain subdivisions within each class. In his initial 1925 paper he found only types 1b, 1a, 2a and 2f. His observation that clusters that contained B stars did not contain giant stars, and that clusters that contained giant stars did not contain B stars seems obvious in terms of the modern theory of stellar evolution. Trumpler also recognised that his classification of clusters had something to say about stellar evolution.

Trumpler, whose understanding of stellar evolution was dominated by the model advocated by Russell, supposed that the reason that clusters containing B stars had no giants was that the massive B stars took so long to become dwarfs that no yellower giants remained by this stage. Trumpler recognised that the relationships he saw between his classes suggested that there could not be a single path of evolution for all clusters if Russell's model of stellar evolution were used. Instead Trumpler suggested that the evolution of the H-R diagram of a cluster depended on the mass of the most massive stars in the cluster. Figure 1.5 shows a diagram, from his 1925 paper, which indicates which classes had intermediate stages separating them, and thus may have been adjacent stages of evolution. It was based on these relationships that Trumpler attempted to devise an evolutionary sequence.

Firstly Trumpler suggested that only the clusters which contained the most massive stars would reach class 1b. He further contended that the most massive stars must evolve most slowly, and so it followed that where there were dwarf B stars, there were no yellow giants. His scheme of evolution was roughly as follows. The evolution of a massive cluster would pass from some

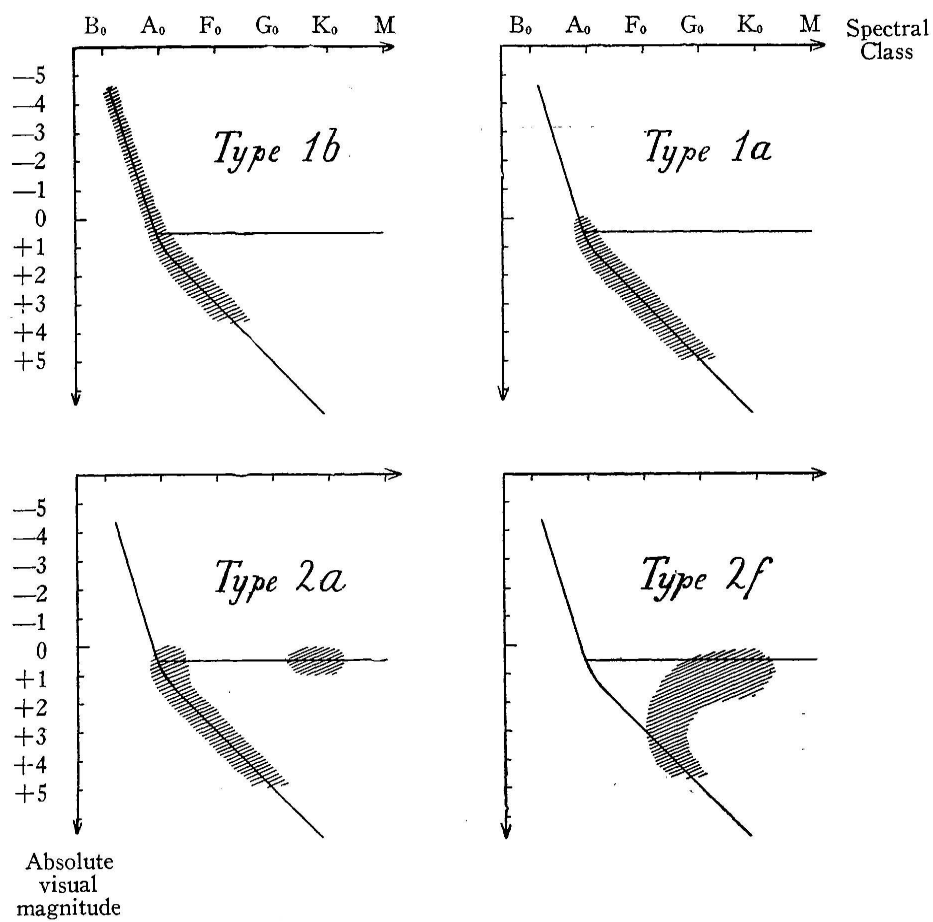


Figure 1.4: The scheme for the classification of open clusters by the form of their H-R diagrams as laid out by Trumpler (1925).

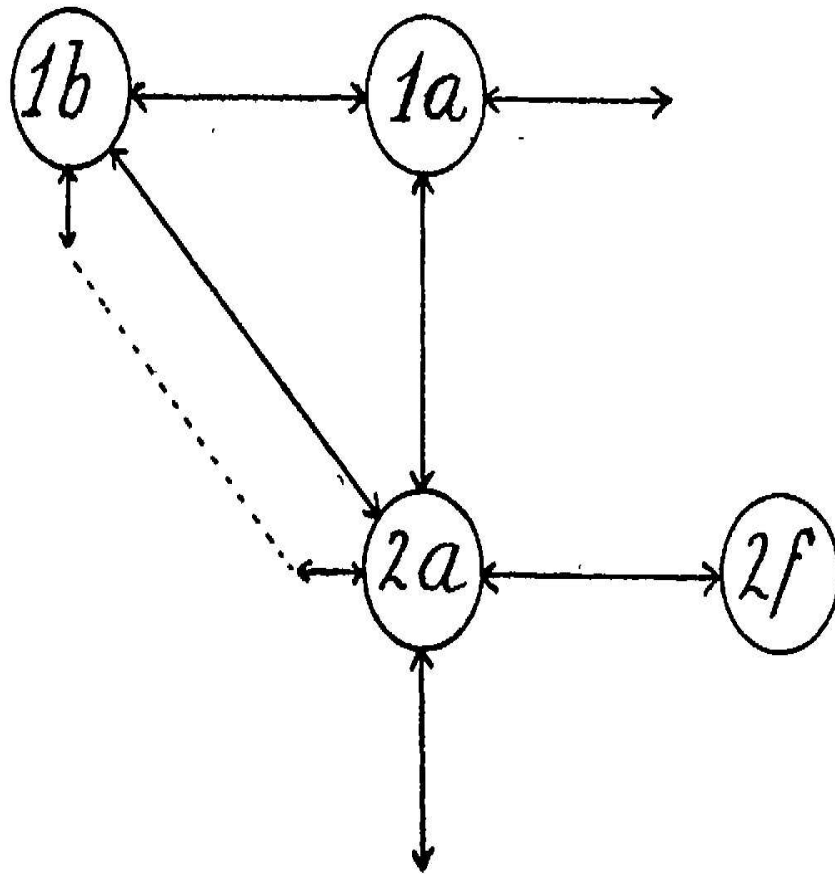


Figure 1.5: The diagram from Trumpler (1925) indicating which classes of cluster appeared to have intermediate stages between them.

as yet unidentified class 3 state through class 2a to 1b and thence toward 1a, 1f and so on. An intermediate mass cluster, on the other hand, would pass from state 3 through class 2a to class 1a and then towards 1f and so on. Clusters consisting of only low mass stars would be expected to pass through class 2f toward 1a or 1f and then toward cooler type 1's. Trumpler had few cases to support this latter progression however. He explains that his reluctance to accept the singular evolutionary path that might have been tempting under the contemporary ideas of stellar evolution, that is 2f-2a-1b-1a-1f, is because "the transition from 2a to 1a is speaking against such an interpretation, and this transition is indeed very gradual and well represented". Trumpler later extended the scheme by identifying class 3, where giants were more numerous than dwarfs, and by including sub-classes where the brightest spectral types were O and O-B (Trumpler, 1930). Trumpler's work represented the first time that the evolution of the stars was related to different forms of the H-R diagram for clusters. However, the paradigm within which he interpreted the relationships between the classes was already under attack when he had written his paper on the matter in 1925.

The pioneering work of Payne (1925) and Russell (1929) finally established that hydrogen was by far the most abundant element in the Sun and other stars<sup>4</sup>. This allowed Strömngren to begin constructing a quantitative theory of stellar evolution based on Eddington's theoretical considerations from 1924 (Strömngren, 1932, 1933). In his 1932 paper he found that the luminosities of stars could only be reproduced if the molecular weight were much lower than the value of  $\mu \approx 2.11$  used by Eddington, and nearer to that implied by the new abundances,  $\mu \approx 0.5$ .

In both papers Strömngren related the evolution of the properties of stars to their location on a H-R diagram. In his 1933 paper he identified that if a star slowly transformed hydrogen to helium, though the details were not known, it would gradually move away from the main sequence upwards and towards the right of a H-R diagram. This was in direct contradiction of the previously accepted model of how a star would move on the H-R diagram as it aged. Figure 1.6 shows the evolutionary tracks, or lines of equal mass derived by Strömngren (1933) along with lines of equal composition. It was thus concluded that rather than being very old, as had been thought by

---

<sup>4</sup>The balance of opinion at the time was against a high abundance of hydrogen and helium, due to what it implied for the current paradigm of stellar evolution. This was so much so that Cecilia Payne wrote off her results in this respect as an anomaly, as evidence in her conclusions: "the stellar abundance deduced for these elements is improbably high, and is almost certainly not real".

Trumpler, open clusters were in fact relatively young.

The theoretical work of Strömgren was finally united with the observational work of Trumpler by Kuiper (1937). Kuiper compared the theoretical tracks of Strömgren to the H-R diagrams for open clusters produced by Trumpler. Figure 1.7 shows the superposition of Trumpler's H-R diagrams used by Kuiper for this comparison. The sequences shown in Figure 1.7 bare a striking resemblance to the lines of equal composition in Figure 1.6. Kuiper thus demonstrated that the different Trumpler classes of open cluster were in fact related by differing compositions, and by implication different ages, but that the stars within a cluster all shared the same composition. Despite the fact that the theory behind these conclusions included no details as to *how* energy was produced in a star by transforming hydrogen to helium, it laid down a new sequence for stellar evolution that could be built upon. The power of the H-R diagram for bringing together theory and observation had been firmly established. When the modern models of stellar evolution were developed, in the light of the work of Bethe (1939) and Schönberg & Chandrasekhar (1942), during the second half of the twentieth century, it was the comparison of theoretical with empirical H-R diagrams that both constrained and drove the theories.

### 1.3 An overview of low-mass star formation

It should now be clear that very quickly after its conception, the H-R diagram became the principal observational tool in the study of stellar evolution. A particular strength of this tool was the fact that it allowed the observable properties of large groups of stars to be studied at once. It is just this kind of statistical study of PMS populations that will be explored in this thesis. For now though, the discussion will move on to examine how the early life of a low-mass star is thought to proceed. This discussion will focus on the observational characteristics of the phases of the star formation process. It will begin when the self-gravitating molecular cloud core has already formed, and will follow the process through to the low-mass star's arrival on the zero age main sequence (ZAMS). The discussion of what leads to the formation of the self-gravitating cloud core will be neglected, however a good review of the kinds of instability that warrant consideration may be found in Stahler & Palla (2004)

Starless, pre-stellar cores are generally considered as the earliest observable stage of star

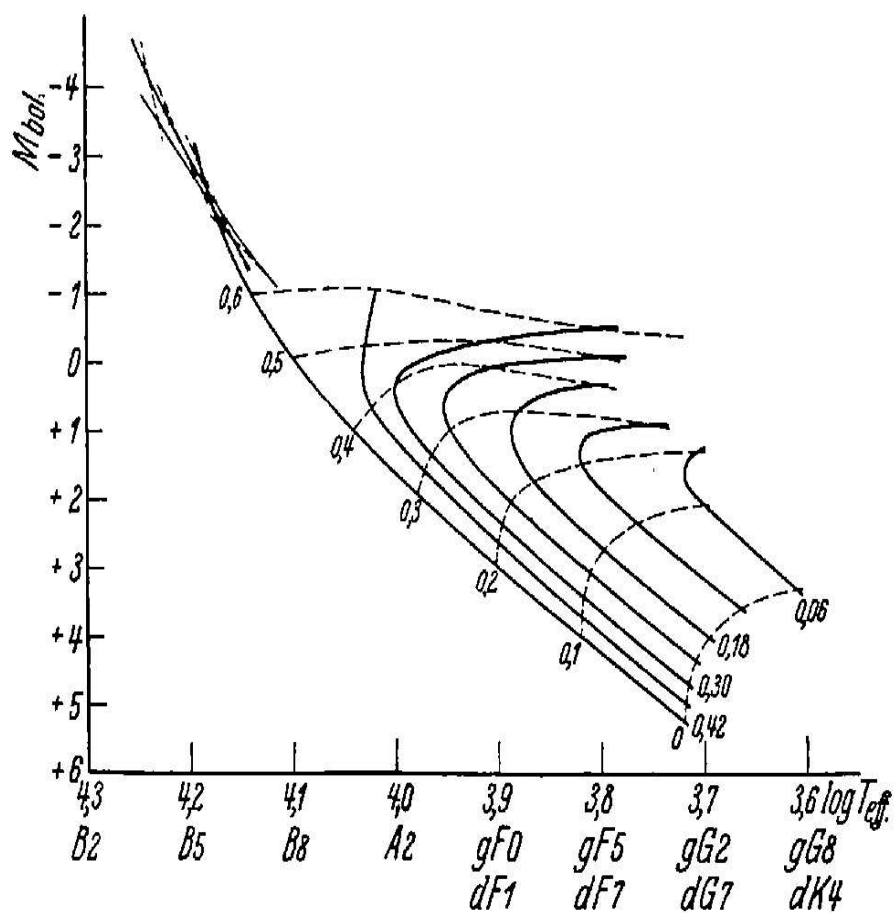


Figure 1.6: The diagram from Strömgen (1933) showing how a stars location on a H-R diagram might be expected to change as it converted hydrogen to helium. The solid lines are lines of equal hydrogen content, or isochrones, whilst the dashed lines are lines of equal mass, or evolutionary tracks.

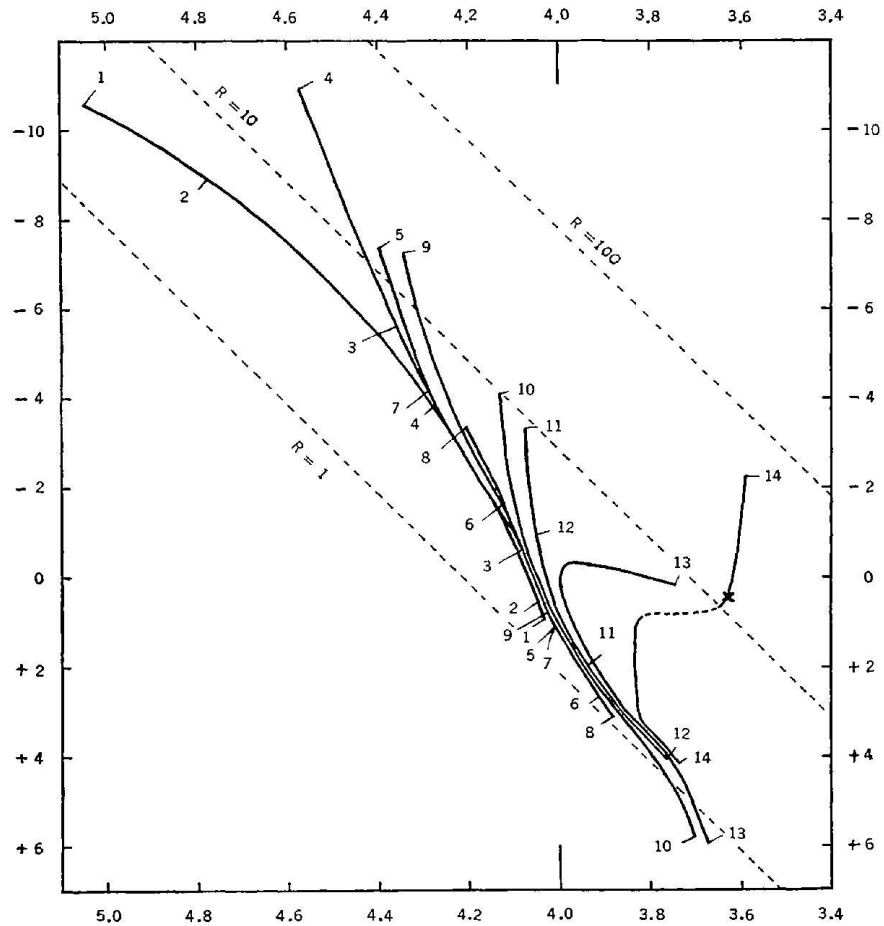


Figure 1.7: The superposition of Trumpler H-R diagrams presented by Kuiper (1937) for comparison to the lines of constant composition of Strömrgren (1933). The abscissae are  $\log T_{eff}$ ; the ordinates are absolute magnitudes.

formation, when the cloud core is evolving to some critical state prior to collapsing (and possibly fragmenting) into a protostellar object(s). These cores are cold, and are generally observed in molecular lines and dust emission. Many investigations into the physical properties and relative populations of these cores have been carried out with a view to understanding the processes which govern the formation of the cloud, define its lifetime and lead to the onset of protostellar collapse (e.g. Ward-Thompson et al., 1994; Andre et al., 1996; Ward-Thompson et al., 1997, 1999; Jessop & Ward-Thompson, 2000; Jijina et al., 1999). However, there is currently conflicting evidence as to whether the cores are long lived, and by implication supported by magnetic fields, or are short lived and transient objects. This conflict, and its context, is discussed in greater depth in Chapter 5. Although there is conflicting evidence as to the lifetimes of pre-stellar cores, some of their physical properties are well determined. The central densities of the pre-stellar cores lie in the range  $10^4 < n < 10^6 \text{ cm}^{-3}$  (e.g. Ward-Thompson et al., 1999), and they have kinetic temperatures of  $\sim 10\text{K}$ .

When the pre-stellar core becomes critical, it collapses isothermally under gravity. The isothermal collapse continues until escaping radiation becomes trapped when the gas and dust becomes optically thick. This is thought to take place when  $n(\text{H}_2) \approx 10^{10} \text{ cm}^{-3}$  in the central regions of the core. At this point the gas begins to heat up as the energy liberated by the collapse cannot radiate away. As the central region heats up the contraction of the core is halted. However, new material is still falling onto the central hydrostatic structure resulting in additional compression, which causes the central temperature to rise. The central temperature rises until it passes 2000K at which point  $\text{H}_2$  starts to be dissociated by collisional processes (Larson, 1969). This causes the temperature to level off as the dissociation of  $\text{H}_2$  absorbs the compressional energy due to gravity. The region of dissociated atomic hydrogen spreads until it becomes unstable against collapse, at which point the collapse of the core begins again. The continuing dissociation absorbs much of the liberated gravitational potential, and at first the temperature rises only slowly. When all of the  $\text{H}_2$  has been dissociated the temperature rises steeply again, so much so that much of the hydrogen is collisionally ionised, and the induced pressure gradients halt the collapse. There are no further internal transitions that can take place within this hydrostatic structure, and it is thus dynamically stable. This second hydrostatic structure is the true protostar.

The subsequent observational stages of the evolution of the protostar towards its arrival on

the ZAMS are commonly separated into four classes of young stellar object (YSO). These classes are class 0, I, II and III. The latter three are defined by the value of the infrared spectral index,  $\alpha_{IR}$ , as defined by equation 1.1 (Lada & Wilking, 1984; Adams et al., 1987).

$$\alpha_{IR} \equiv \frac{d \log(\lambda F_\lambda)}{d \log \lambda} \quad (1.1)$$

Where  $\lambda$  is the wavelength of the radiation, and  $F_\lambda$  is its specific flux. In practise the value of  $\alpha_{IR}$  is determined numerically from the spectral energy distribution (SED) between 2.2 and 10  $\mu\text{m}$ . Class I sources have  $\alpha_{IR} > 0$ ; their SED is rising as one moves from 2.2 to 10  $\mu\text{m}$ . Class II sources have  $-1.5 < \alpha_{IR} < 0$ , so their SED is nearly flat or falling slightly between 2.2 and 10  $\mu\text{m}$ . Class III sources have  $\alpha_{IR} < -1.5$ , and their SED is falling from 2.2 to 10  $\mu\text{m}$ .

The creation of the protostar heralds the beginning of the class 0 phase of evolution. Since YSOs in this phase of evolution are still embedded in their parent clouds, they are only detected in the sub-mm, and so the criterion for the classification used for the three later stages is not appropriate. Typically the peak of the SED for a class 0 source is  $\sim 100 \mu\text{m}$  (Adams et al., 1987). During this time the central protostar gains mass by accretion of material infalling from the outer regions of the original cloud core, this is also known as the main accretion phase. Since the free-fall time is smaller near the central protostar, the collapse proceeds in an inside out manner. Due to the initial rotation of the cloud core, the infalling matter rapidly forms a disk. High angular momentum material falls first onto this accretion disk, and is then transported inwards by viscous processes. During this phase the total luminosity is dominated by the accretion luminosity.

As the main accretion phase proceeds powerful protostellar outflows develop along the rotation axis, which act to clear out the residual envelope. Shocking of adjacent gas by protostellar outflows and jets has been proposed as a possible feedback mechanism, triggering further star formation in the local region of gas (Preibisch & Zinnecker, 1999). As the natal cloud is cleared the protostar and its accretion disk become visible in mid- and far-IR. At this stage the object is classified as a class I YSO. The peak of the SED for a class I YSO still lies at  $\sim 100 \mu\text{m}$ , however a greater portion of radiation escapes at shorter wavelengths than for a class 0 source. During this period the mass of the protostar exceeds that of the remnant natal envelope. The action of the infalling material and the outflows during this period also lead to the disruption of the remaining

cloud core and the main accretion phase comes to an end. Class I sources are often visible at optical wavelengths when viewed along the rotation axis.

The YSO now enters the class II phase. The natal envelope has disappeared through a combination of dispersal by outflows and accretion onto the central protostar. The protostar no longer gains appreciable mass through accretion and it begins to contract towards the ZAMS. A tenuous disk of gas and dust remains but its mass is low, typically  $10^{-3}$  times that of the PMS star. However, since the disk is still optically thick at  $\lambda < 10\mu m$ , it still provides a significant contribution to the SED, which is now dominated by the black body curve at optical wavelengths. The protostar proceeds to the class III stage when the remnant disk becomes optically thin at  $\lambda < 10\mu m$ , and thus provides little infra-red excess.

Because the spectra of class II and III sources are dominated by the photosphere of the central protostar, the evolution of their observed properties is dominated by their contraction toward the ZAMS. Class II and III objects are more commonly known as PMS stars and include classical T Tauri stars (CTTS) and weak-lined T Tauri stars (WTTS). Conventionally CTTS are considered to be class II sources, whilst WTTS are thought to be class III sources. Since this last phase in the formation of a star is of particular significance to the work presented in this document, it will now be discussed in detail, with particular emphasis on the progress of the PMS star across the H-R diagram.

## 1.4 PMS evolution and the H-R diagram

The PMS phase of evolution for a young star begins when it appears at the birthline on the H-R diagram. This is the point at which it becomes optically visible having shed its natal cloud. The PMS phase ends when hydrogen fusion in the core brings the star into hydrostatic equilibrium, and it arrives on the ZAMS. T Tauri stars are low-mass PMS stars ( $M_* \lesssim 2M_\odot$ ), whilst Herbig Ae/Be represent the PMS stage for intermediate mass stars ( $M_* \lesssim 10M_\odot$ ). High mass stars ( $M_* \gtrsim 10M_\odot$ ) are not thought to have an optical PMS phase as the rapid protostellar collapse of a massive core is expected to trigger hydrogen fusion while the main accretion phase is still in progress. As such the birthline for massive stars lies on the ZAMS. Since this thesis deals

almost exclusively with low-mass stars in OB association-like environments, this discussion will now focus on the PMS evolution of low-mass stars.

Figure 1.8 shows theoretical evolutionary tracks for PMS stars computed by D’Antona & Mazzitelli (1994). The tracks all begin at the birthline, and terminate at the ZAMS. Because hydrogen fusion has not yet started in the core of a PMS star, the luminosity is provided by the compressive work of gravity. As the star contracts it becomes less luminous due to a decreasing surface area, and it moves downwards across the H-R diagram away from the birthline. This occurs on the Kelvin-Helmholtz timescale,  $t_{KH}$ :

$$t_{KH} = \frac{GM_*^2}{R_*L_*} \quad (1.2)$$

The PMS stars shrinks by a factor two over a time interval of length  $t_{KH}$ , and this interval varies strongly with mass. This means that more massive PMS stars evolve towards the ZAMS much more quickly than lower mass stars. As such the isochrones, in the region where the evolutionary tracks are nearly vertical, are more widely spaced for the more massive PMS stars. Further, equation 1.2 also demonstrates that the contraction slows at later times when the radius and luminosity have decreased due to the contraction. As such motion across the H-R diagram is much faster at earlier stages of evolution than at later stages. This is reflected in the fact that the isochrones for younger ages are more widely spaced than the later isochrones in Figure 1.8.

During this almost vertical descent on the H-R diagram, along what are known as Hayashi tracks, the dominant energy transport mechanism within the PMS star is convection. As the temperature in the PMS star rises due to contraction, however, the energy transport in the core becomes radiative in nature, and the PMS stars depart from their Hayashi tracks, and move leftwards on the H-R diagram, along Henyey tracks. As Figure 1.8 demonstrates, this point is reached much sooner for higher mass stars, and the lowest mass stars ( $M_* < 0.4M_\odot$ ) are thought remain fully convective right through until they reach the ZAMS. The sharp downturn seen on the tracks for stars with  $M \approx 1M_\odot$ , just prior to arrival on the ZAMS, corresponds to the commencement of core hydrogen burning in these objects.

There are a number of different sets of models for PMS evolution for low and intermediate mass stars available (e.g. Baraffe et al., 1998; Chabrier et al., 2000; D’Antona & Mazzitelli, 1994,

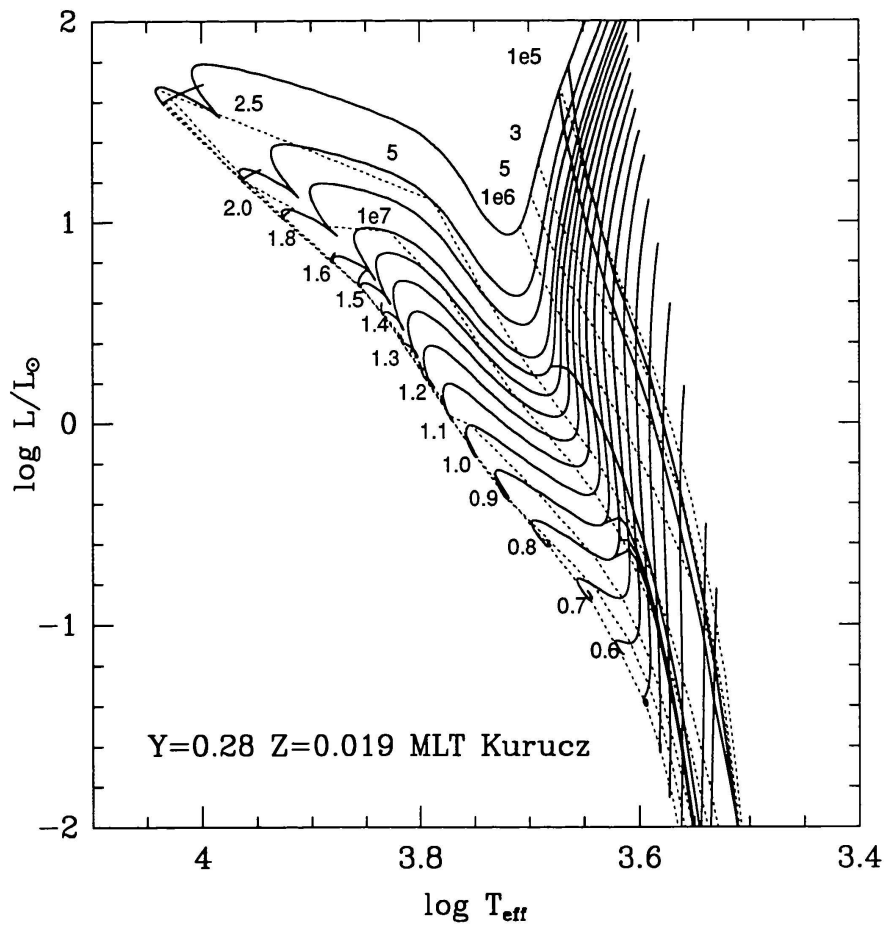


Figure 1.8: Theoretical evolutionary tracks on the H-R diagram from D'Antona & Mazzitelli (1994) for low-mass PMS stars. The dotted lines represent isochrones at  $10^5$  yrs through  $10^7$  yrs, solid lines are evolutionary tracks. The masses of the PMS stars are denoted at the left-hand end of the evolutionary tracks in units of  $M_{\odot}$ . These models are for solar metallicity.

1997; Siess et al., 2000). Because of the large uncertainties involved in placing PMS stars on the H-R diagrams it is not possible to establish if any one set is a significantly better representation of PMS evolution than any other. However, the use of certain group’s isochrones is more widespread as it allows for inter-comparison of results from different projects aimed at determining mass functions, star forming histories and so on. The most popular sets of evolutionary tracks at present appear to be those by Baraffe et al. (1998); Chabrier et al. (2000) (the “Lyon group”) and those by D’Antona & Mazzitelli (1994, 1997).

The principle differences between these two sets of models lie in their equations of state (EOS) and their treatment of convection. The evolutionary tracks computed by D’Antona & Mazzitelli (1994, 1997) use the MHD EOS set out by Mihalas et al. (1988) for low and intermediate masses, and that of Rogers et al. (1996) for high masses. The Lyon group, on the other hand, use the hydrogen-helium EOS of Saumon et al. (1995). The Lyon group, like other groups (e.g. Siess et al., 2000) treat convection using mixing length theory, with  $1 < \alpha_{mix} < 2$ . D’Antona & Mazzitelli (1994, 1997), however, instead use a Canuto-Mazzitelli formalism which, they argue, accounts more accurately for the nature of turbulent convection. A comparison of the evolutionary tracks produced by these groups and others is provided by Siess et al. (2000), in which the relative validity of these treatments is discussed.

One way to compare observations of PMS stars to the models is place the PMS stars on the H-R diagram in bolometric luminosity,  $L_{bol}$ , versus effective temperature,  $T_{eff}$ , space, i.e. in the same space as the evolutionary tracks in Figure 1.8. This method is used frequently to obtain ages for PMS stars in young clusters (e.g. Preibisch & Zinnecker, 1999; Preibisch et al., 2002; DeGioia-Eastwood et al., 2001) and to derive mass functions (e.g. Greene & Meyer, 1995; Briceño et al., 2002; Luhman et al., 2000). There are, however, potential problems with comparing observational data with theoretical models in the idealised plane of  $L_{bol}$  and  $T_{eff}$ .

The potential hurdles to comparing data with theory in the  $L_{bol}/T_{eff}$  plane arise when transforming data from the observational plane of colour-magnitude, or magnitude-spectral type, into the theoretical plane. Firstly there is the problem of converting observed magnitudes in a particular waveband to the bolometric luminosity,  $L_{bol}$ . Young PMS stars frequently emit excess radiation in the UV, due to accretion luminosity, and IR, due to circumstellar disks. As a result, it is not possible to derive the bolometric luminosity simply by integrated the flux across broadband

magnitudes. Instead authors convert magnitudes from filters selected to avoid contamination from non-photospheric sources to  $L_{bol}$ , such as the J-band (e.g. Kenyon & Hartmann, 1990) or I-band (e.g. Preibisch & Zinnecker, 1999). The bolometric corrections (BC) that are applied are frequently those of standard (MS) dwarfs of the same spectral type (e.g. Kenyon & Hartmann, 1995; Hartigan et al., 1994). This method, however, is suspect. For a given spectroscopic temperature measured in the red, PMS stars tend to be redder than main sequence stars due to their lower surface gravity. This means that dwarf bolometric corrections should not be applied to PMS objects. Furthermore, the  $T_{eff}$  scale for main-sequence cool stars is highly uncertain, and the situation is worse for cool PMS stars.

In addition to the uncertainties associated with obtaining  $T_{eff}$  and correct BCs for cool PMS stars, comparing observations to theory in the  $L_{bol}/T_{eff}$  plane requires a more costly observing programme. This is because spectroscopy is the best tool for obtaining  $T_{eff}$ . Studies of PMS populations, be they for the purpose of measuring the IMF, determining the star forming history of a young cluster or better constraining PMS models, are best carried out on a large number of objects so the impact of observational uncertainties may be minimised. Even with the use of modern fibre spectrographs, such as WYFFOS on the William Herschel Telescope (La Palma) and FLAMES on the Very Large Telescope (Paranal), obtaining enough spectra for determining spectral types for a large number of low-mass stars and brown dwarfs is time consuming, and hinges on the availability of sufficient observing time.

In this work PMS models will be compared to observations purely in the observational plane. To achieve this I have used theoretical isochrones that have been transformed into the relevant colour-magnitude planes by Dr Rob Jeffries, following the method described in Jeffries et al. (2001). Such a method has been used by a number of authors for similar reasons (e.g. Barrado y Navascués et al., 2002; Pozzo et al., 2003; Muench et al., 2002; Kendall et al., 2005; Sherry et al., 2004). The key to this method's success is the relation between colour and effective temperature. This is obtained roughly as follows. Firstly, it is assumed that a single colour- $T_{eff}$  relation holds for all stars of approximately the same age as the Pleiades, for which the following values are adopted: age = 120 Myr; distance modulus = 5.6;  $E(B - V) = 0.05$ ;  $E(V - I_c) = 0.04$ ;  $A_v = 0.13$ . BC-colour relationships are obtained from polynomial fits to the data in Flower (1996) for  $B - V$ , and a combination of data from Leggett et al. (1996) for  $V - I < 0.7$  and atmospheric models by Bessell

et al. (1998) for  $V - I > 0.7$ . Empirical isochrones are then fitted to both  $BV$  and  $VI$  CMDs for the Pleiades, ensuring that any upward biasing due to binary members is avoided. Absolute magnitudes and intrinsic colours are then found for 25 points along each isochrone. These are then converted to  $L_{bol}$  using the BC-colour relationships already derived. Thus,  $L_{bol}$  as a function of intrinsic colour is determined. By interpolating along a 120 Myr model isochrone,  $T_{eff}$  can then be determined for any appropriate value of  $L_{bol}$ . Hence, a set of intrinsic colour- $T_{eff}$  points may be defined, and used for converting other model isochrones.

## 1.5 Identifying PMS stars

The CMD plays a central role in identifying PMS stars for study in young clusters and OB associations. As can be seen in Figure 1.8, PMS stars are over-luminous for their effective temperatures, compared to ZAMS objects. By selecting an appropriate combination of colours for a CMD (e.g.  $I/R - I$  or  $V/V - I$ ), candidate low-mass PMS stars may be detected as lying redward of the Galactic background (e.g. Pozzo et al., 2003; Béjar et al., 1999; Barrado y Navascués et al., 2002). This is in part made simpler by the observation that the Galactic reddening vector often lies nearly parallel to the PMS isochrones (e.g. Preibisch & Zinnecker, 1999; Pozzo et al., 2003), reducing the likelihood of contamination from background main sequence stars. As has already been stated, the issue of contamination of the PMS region of a CMD is addressed in detail in Chapter 4. An example of a clearly visible PMS is shown in Figure 1.9.

Although candidate PMS stars may be selected by their location on an appropriate CMD, it is often necessary to obtain corroborating ancillary data if individual objects are to be confirmed as PMS stars, or if the existence of the cluster or association in question is in doubt. There are number of other properties of PMS stars that may be exploited by an observer to achieve this. One of these is to determine the spectral type of the object, which when combined with knowledge of the distance will indicate if the object is indeed over-luminous. A number of other popular distinguishing features are detailed below.

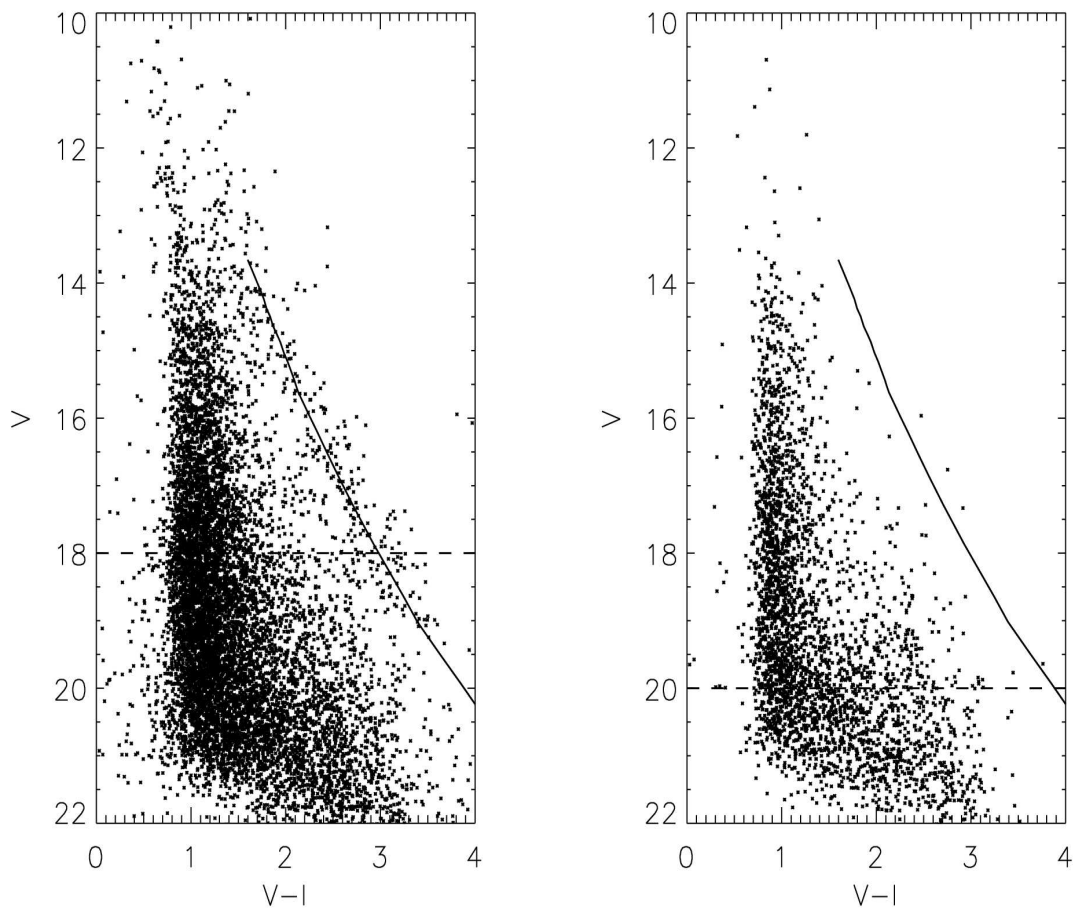


Figure 1.9: *Left*: The  $V$  vs.  $V - I$  CMD for a survey area in region of the  $\sigma$  Ori young group. The solid line is a 2.5 Myr isochrone (Baraffe et al., 1998, 2001) at a distance of 440 pc (Brown et al., 1994). The isochrone follows the expected PMS locus for the Orion OB1b association, of which  $\sigma$  Orionis is a member. *Right*: The same CMD but for a control field. In both cases the dotted line represents the completeness limit. Taken from Sherry et al. (2004).

### 1.5.1 H $\alpha$ emission

Amongst the first PMS stars to be identified as such were the T Tauri stars (Ambartsumian, 1947; Herbig, 1977; Walker, 1956). T Tauri stars display periodic and non-periodic variability on a variety of timescales. The origins of this variability are discussed in greater depth in Chapter 5. The sub-class of T Tauri star that displays the greatest degree of variability are the classic T Tauri stars (CTTS). One of the defining properties of a CTTS is broad H $\alpha$  emission, with an equivalent width of  $EW(H\alpha) < 10 \text{ \AA}$  (Appenzeller & Mundt, 1989). Another sub-class of T Tauri stars are the weak-lined T Tauri stars (WTTS). These are T Tauri stars which exhibit H $\alpha$  emission with  $EW(H\alpha)$  below the  $10 \text{ \AA}$  threshold. This can mean the H $\alpha$  emission is weak, or it may be absent. Since broad H $\alpha$  emission can be detected using relatively low-resolution spectra with poor signal-to-noise, this observational characteristic has been exploited as a diagnostic tool when seeking to identify PMS objects (e.g. Ogura et al., 2002). Since only CTTS display such strong emission, however, this diagnostic introduces a significant bias to any survey.

It is generally thought that the H $\alpha$  emission arises as a result of processes related to the magnetospheric accretion of material from a circumstellar disk on to the surface of the T Tauri star (e.g. Edwards et al., 1994; Muzerolle et al., 1998). This has led to a widely held belief that CTTS stars represent class II sources (with a circumstellar disk that is optically thick at  $\lambda < 10\mu m$ ), while WTTS are class III sources (with a disk that is optically thin at  $\lambda < 10\mu m$ ). This viewpoint is supported by correlations between infrared colour excesses and H $\alpha$  emission in T Tauri stars (Cabrit et al., 1990). As such, a survey which uses H $\alpha$  emission to identify PMS objects would be expected to preferentially select objects with circumstellar disks. However, recently this standard paradigm has been challenged by observations of possible high accretion rates in WTTS, leading to speculation that T Tauri stars might switch between weak-lined and classic states, depending on a variable accretion rate (Littlefair et al., 2004). This also implies that WTTS may have circumstellar disks. As a result it is no longer clear that the bias introduced by using the H $\alpha$  emission diagnostic is one toward selecting objects with disks, but rather objects with active accretion.

### 1.5.2 X-ray emission

It has long been observed that low-mass PMS stars are bright X-ray emitters (e.g. Montmerle et al., 1983; Strom & Strom, 1994). Inferred X-ray luminosities range from  $< 10^{28}$  to  $10^{31}$  erg s $^{-1}$  (Feigelson & Montmerle, 1999). This is considerably greater than is typical for main sequence objects. X-ray emission in main-sequence dwarfs is thought to be driven by magnetic activity arising from a dynamo action, similar in nature to that which drives the Sun's magnetic activity. X-ray emission in PMS stars is also thought to originate in the chromosphere, driven by magnetic activity, but the driving force for this activity is less clear (Feigelson et al., 2003; Stassun et al., 2004). One of the reasons for this is that high-levels of X-ray emission are observed in objects that are thought to be fully convective. This would be unexpected in the solar dynamo model since the magnetic field is thought to be generated and amplified at the boundary between the radiative core and convective zone, known as the tachocline. Another reason for this uncertainty is that a correlation between rotation and X-ray emission has not been well established. This is in contrast to main-sequence stars for which there is a well established correlation between rotation and magnetic activity indicators (e.g. Knobloch et al., 1981). Recent work has shed some light on these problems, and currently the favoured driving mechanism for magnetic fields in PMS stars is a combination of a turbulent dynamo distributed throughout the deep convective zone (distributed convective dynamo) for objects with no tachocline, and a solar type dynamo when a tachocline is present (Feigelson et al., 2003; Preibisch & Feigelson, 2005).

The X-ray observations have been used by a number of authors for the purposes of identifying PMS stars (e.g. Preibisch et al., 1996; Naylor & Fabian, 1999) It has been noted by some authors that WTTS appear to be brighter X-ray emitters (e.g. Neuhaeuser et al., 1995; Preibisch et al., 1996; Kastner et al., 2003) than the CTTS. If true this would introduce a significant bias to any sample of PMS objects selected by X-ray emission alone. On the other hand, it has been concluded by others that X-ray selection does not introduce any bias more significant than any other methods of PMS star selection (Flaccomio et al., 2000). Clearly this issue hinges on the relative X-ray properties of the two classes of objects, and how we divide them. Feigelson et al. (2003) performed a detailed study of the X-ray properties of 575 PMS stars in the Orion Nebula Cluster (ONC) and found no correlation between the presence, or lack thereof, of infrared circumstellar disks and X-ray levels.

Most recently, Preibisch et al. (2005) studied a similar number of objects also in the ONC and found that accreting objects were a factor 2-3 less X-ray active than non-accreting objects. These results support further questioning of the previously accepted paradigm that WTTS have shed their circumstellar disks. It is also clear, however, that whilst X-ray selection of PMS objects is efficient, as a method it is biased toward selecting non-accreting objects.

### 1.5.3 Lithium absorption

Another spectral feature that defines the T Tauri class is the presence of Li I absorption at  $\lambda 6708 \text{ \AA}$ . The dominant isotope of lithium in stars,  ${}^7\text{Li}$ , fuses with protons at temperatures greater than  $3 \times 10^6 \text{ K}$ , to form beryllium-8, which then decays to two helium nuclei. Since low-mass protostars do not achieve the necessary core temperature to burn lithium, they cross the birthline with its abundance at interstellar values. Although higher mass protostars do achieve sufficient central temperatures to burn lithium, it is only the lithium in the central region that gets destroyed. This is because by the time the central temperature reaches  $3 \times 10^6 \text{ K}$ , the protostar is already radiative in the centre-most regions. The base of the convective zone, however, is too cool to allow lithium burning. As the base of the convective zone moves outwards (and more of the star becomes radiative) its temperature remains below the ignition point for lithium, and so the surface abundance remains at the interstellar value. So all PMS stars arrive at the birthline with their surface abundance of lithium equal to its interstellar value.

As the PMS contraction proceeds the temperature at the base of the convective zone of a PMS star passes the ignition point for lithium burning. In PMS stars that are fully convective at this point, the lithium burning starts at the centre. As the tachocline retreats toward the surface, its temperature remains high enough to maintain lithium burning. The action of turbulent eddies in the convective stellar atmosphere keeps the region above the tachocline well mixed, which leads to the lithium abundance declining uniformly as the PMS evolution proceeds. When the tachocline has receded to a sufficient radius its temperature will fall below the ignition point for lithium. In stars with  $M < 0.9M_{\odot}$  this occurs after the lithium has been fully destroyed. For PMS stars with  $M > 0.9M_{\odot}$  such complete lithium depletion does not take place. This is because the tachocline retreats earlier in these cases, such that its temperature falls below  $3 \times 10^6 \text{ K}$  before all the lithium

has been destroyed. PMS stars with  $M > 1.2M_{\odot}$  do not deplete the lithium in their convective zone as the tachocline is already so shallow when the birthline is crossed that its temperature never rises above  $3 \times 10^6$  K. In the very low-mass regime lithium depletion ceases for objects with  $M < 0.06M_{\odot}$ , for which temperatures never exceed the ignition point for lithium burning (Chabrier & Baraffe, 1997).

It follows from the above explanation that the presence of strong Li I absorption in the spectra of stars and brown dwarfs with masses in the range  $0.06M_{\odot} < M < 0.9M_{\odot}$  is a strong indicator of youth and PMS status. Since masses are not trivial to determine, it is normally the colour or spectral type of an object that is used to assess if the presence of Li I is indeed indicative of youth. The degree of depletion can be used as an indicator of age for individual objects, and may be found by comparing the observed EW(Li I) at 6708 Å with those predicted from curves of growth for different abundances at the appropriate  $T_{eff}$ . Alternatively, finding the magnitude at which lithium depletion ceases to be evident can be used to estimate the age of a cluster or association (e.g. Jeffries & Oliveira, 2005). The success of such a method lies in the fact that more massive PMS stars deplete lithium more rapidly. This is because their convective regions both reach the ignition point for lithium burning sooner, and will have a greater portion above this temperature. The strength of Li I absorption has also been used as a PMS diagnostic for candidates selected on the basis of their positions on CMDs for young clusters and associations, and in conjunction with kinematic data that suggests membership of a cluster or association (e.g. Pozzo et al., 2003; Kenyon et al., 2005; Dolan & Mathieu, 1999).

#### 1.5.4 Kinematic methods

The final method for determining an object's PMS status, that will be discussed here, is to infer it by showing common motion with a young cluster or association. For such inferences to be made the object must also lie in the appropriate region of colour-magnitude space to form part of a PMS of the appropriate age and at the appropriate distance. The motions of stars are measured in two perpendicular directions. The motion of a star on the plane of the sky, relative to much more distant stars, or extra-galactic objects, is known as proper motion. The second direction in which the motion of a star may be measured is the radial direction, i.e. along the line of sight to the star.

This is called its radial velocity. Bound clusters share common motion through the Galaxy, and members can be identified as having the same peculiar motion. OB associations and some young clusters are not bound, however, since they are young their velocity dispersions are often small, so again members will share a common motion.

Proper motion has been used extensively to establish membership, and indeed the existence, of open clusters and OB associations for more than one hundred years. de Zeeuw et al. (1999) performed one of the most extensive studies to date of membership of nearby OB associations using proper motions obtained from the HIPPARCOS catalogue. They confirmed the existence of several previously known OB associations and young clusters, and identified one new moving group, within 1 kpc of the Sun. This represents the largest distance over which proper motions have been used to assess membership of such groups. Proper motions have not been used extensively to assess low-mass membership of young clusters and associations however. The reason for this seems to be that the high precision catalogue which would allow such determinations, HIPPARCOS, has relatively bright limiting magnitude, which excludes the lowest mass members of all but the most nearby associations. New high precision measurements must be taken over long temporal baselines in order to extend the use of proper motions to the fainter magnitudes required for studying the lowest mass stars and brown dwarfs.

Radial velocities can be obtained for very faint objects in a single observation. As a result, radial velocities have been used extensively for assessing membership of young clusters and associations (e.g. Dolan & Mathieu, 1999; Pozzo et al., 2003; Kenyon et al., 2005). Radial velocities are normally found, as will be demonstrated in Chapter 4, by cross correlating the spectra of target stars against those of radial velocity standards with a similar spectral type. The Doppler shift gives the radial velocity. When radial velocity data has been combined with other indicators of PMS status, it can provide a powerful diagnostic tool for identifying PMS stars with confidence. Figure 1.10 is taken from Dolan & Mathieu (1999). It plots EW(LiI) against radial velocity for a sample of stars in the  $\lambda$  Orionis region. PMS members are clearly visible as the objects with strong Li I absorption and a shared radial velocity, consistent with the radial velocities of other members of the Orion OB1b association. That study was able to identify 70 new PMS stars, which had not been previously identified by either H $\alpha$  or X-ray emission.

Figure 1.10 also demonstrates one of the limitations of kinetic methods of assessing member-

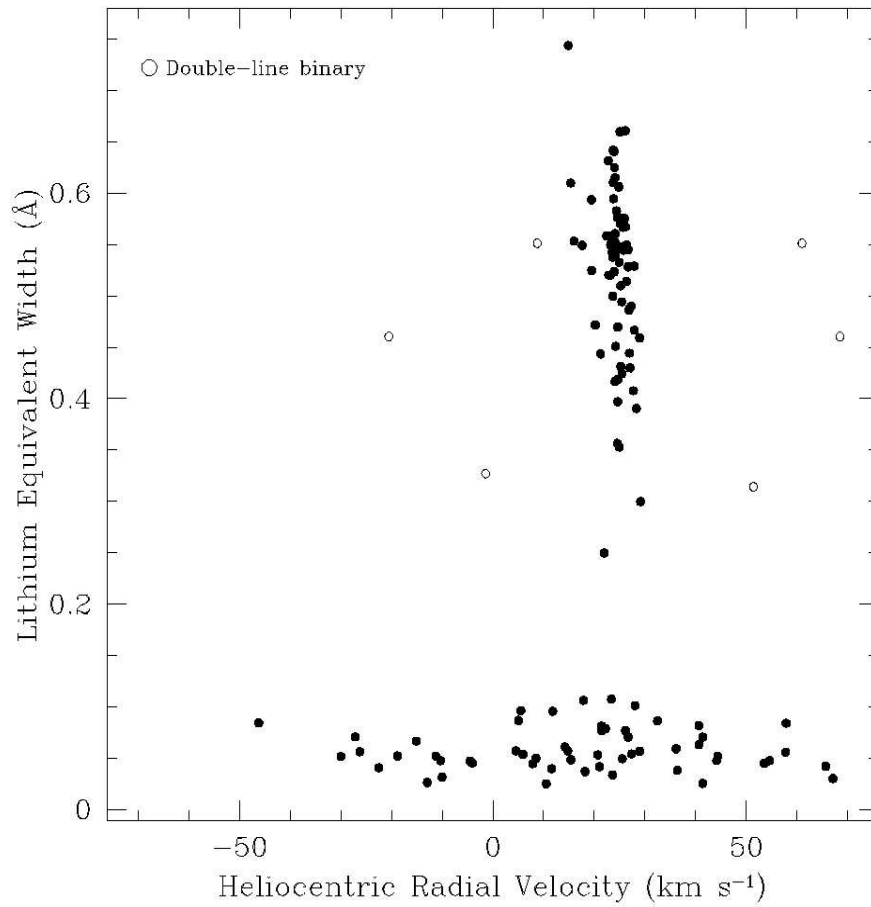


Figure 1.10: The EW(Li) vs. radial velocity plot from Dolan & Mathieu (1999). All stars with strong LiI absorption were accepted as members of the  $\lambda$  Orion association.

ship of associations and clusters. The problem arises as it is not possible to distinguish bona-fide members of a young cluster from objects that simply share their velocity without ancillary data. Those objects in Figure 1.10 with the appropriate radial velocity, but no strong Li I absorption are likely non-members of the group. If only radial velocity data were held this would be impossible to determine. The same effect can plague proper motion studies. Attention should be paid to potential contamination when assigning membership to individual objects based on kinematic data alone.

The presence of spectroscopic binaries can also hinder the use of radial velocity as a membership criterion. Double-lined binaries are easy to identify by virtue of the presence of duplicated absorption features in their spectra. Things are not so simple for single-lined binaries. These are binary systems in which the two stars have very different masses. This means that the spectrum of the secondary star is swamped by the spectrum of the primary. In such cases the measured velocity, of the primary, will vary as the stars orbit each other, and this provides a method of identification. In a single observation, however, this is not possible, and single-lined binaries would likely be excluded from any given membership selection on the basis of their measured velocities. As will be discussed briefly in Chapter 5, the mass ratio distribution for low-mass binary stars has a peak at a ratio,  $q$ , of 0.2. However, the distribution is not so strongly peaked that single-lined binaries outnumber double-lined binaries. In fact, there are typically three times as many double-lined binaries as there are single-lined binaries (e.g. Dolan & Mathieu, 2001).

## 1.6 OB associations

Due to their short lifetimes, O and B-type stars necessarily trace sites of recent star formation. As loose aggregations of massive stars, often containing tens of O-stars, OB associations have been important to the study of star formation since they were first identified as young structures in the middle of the twentieth century (Ambartsumian, 1947). Gravitationally unbound (Blaauw, 1952; Ambartsumian, 1955), these large clusters span a wide range of size scales, from a few tens to several hundreds of parsecs, apparently expanding and dissipating from their sites of formation, slowly becoming indistinguishable from the galactic field population. Due to the short lives of their defining characteristic, OB associations are always younger than about 30 Myrs, and the

youngest are frequently the most compact. Despite their large internal velocities, typically of around  $4 \text{ km s}^{-1}$ , it is common motion and, by implication, common origin that defines membership to a given OB association. Within OB associations in the solar neighbourhood, a great deal of substructure is seen, with star formation at different stages being observed within a single co-moving group. For example, the IC348 young cluster forms part of the Per OB2 association. Similarly, the Orion Nebula Cluster (ONC) forms the central part of the Orion OB1d, itself a subgroup of the Orion OB1 association. These two cases also exemplify the fact that most OB associations are adjacent to, or partially embedded in, giant molecular cloud complexes.

According to most estimates of the IMF, one can expect several hundred low-mass stars to be formed for each O or early B-star. As such, it is reasonable to suppose that most stars are formed as part of OB associations. The large number of low-mass stars that can be found in these groups, combined with low-extinction sight lines, presumably due to the effects of massive stars on local molecular gas, has made them fertile ground for studies of the low-mass part of the IMF.

Crucial to the study of the IMF is the reliable selection of members of the group that is being studied. For this purpose, amongst others, large surveys for low-mass PMS stars in OB associations have been carried out by a number of authors, using the techniques already described in this chapter for identifying PMS stars.

As the closest OB association, Upper Scorpius has been the subject of many observing campaigns, frequently aimed at identifying low-mass stars and brown dwarfs. Preibisch et al. (2002) performed an extensive study of the stellar population in the Upper Scorpius OB association. They used 2dF spectroscopy to select low-mass PMS objects on the basis of lithium absorption, finding 166 new PMS stars. Previous surveys for low-mass members of Upper Scorpius, by the same authors, had also used the combination of X-ray and photometric selection techniques (Preibisch & Zinnecker, 1999). A number of authors have also searched for low-mass members of Upper Scorpius using photometric selection criteria (e.g. Ardila et al., 2000; Costado et al., 2005). Béjar et al. (2001) also used photometric selection in the  $\sigma$  Orionis young group for the purpose of constructing an IMF. The validity of these photometric selection techniques is not well established, and the issues associated with such methods are discussed in greater depth in Chapter 4.

Kinematic methods have been used less frequently for identifying low-mass members of OB associations. This is partly because such faint objects have generally been excluded from large

scale proper motion studies. Radial velocities have been used to a limited extent, but normally in concert with other spectroscopic indicators such as lithium absorption or  $H\alpha$  emission. For example, Dolan & Mathieu (1999) used the combination of lithium absorption and radial velocities to select members of the  $\lambda$  Ori association (see Figure 1.10). Similarly, Pozzo et al. (2003) used lithium absorption,  $H\alpha$  emission and radial velocities to identify PMS stars in the Cep OB3b association. Measured values for  $EW(\text{Li I})$  at  $6708 \text{ \AA}$  in low-mass PMS stars are typically smaller than  $0.8 \text{ \AA}$ . The high signal-to-noise that is required to observe the weak lithium absorption also allows weak metal lines in the same spectral region to be used for measurement of radial velocity. Such a two-pronged observational tool for identifying member objects below the lithium burning threshold ( $M < 0.06M_{\odot}$ ) is yet to be demonstrated.

A promising candidate for such a tool is the gravity sensitive sodium doublet at  $8183, 8195 \text{ \AA}$ . As is discussed in greater detail in Chapter 4, this doublet was used to identify low surface gravity, and presumably young, low-mass objects in Upper Scorpius (Martín et al., 2004). This doublet is a much stronger feature in late-type spectra than the  $6708 \text{ \AA}$  lithium absorption. Added to which is the fact that the lowest mass objects are brighter at  $8190 \text{ \AA}$  than at  $6708 \text{ \AA}$ . This means that the doublet could be used to obtain radial velocities, and its  $EW(\text{NaI})$  used as a second diagnostic for selecting low-mass members of OB associations, an idea that is explored in detail in Chapter 4.

## 2 Investigation of a comparison field for the $\gamma$ Velorum cluster

### 2.1 Introduction

As discussed in Chapter 1, the use of CMDs in the study of young clusters and OB associations provides the possibility of identifying large numbers of candidate members economically. Further, in conjunction with ancillary data, such as X-ray observations, appropriate CMDs have been used to identify previously unknown PMS populations. In this chapter I will describe a brief experiment that I carried which uses this method. In this project X-ray data and a *VI* CMD are used to search for low-mass members of the Vela OB2 association.

Pozzo et al. (2000) reported the discovery of a group of low-mass, PMS stars around the Wolf-Rayet (WR) star  $\gamma^2$  Velorum. They used ROSAT X-ray observations to select X-ray bright objects on a *VI* CMD and identified those objects that were both X-ray bright and in the appropriate region of the CMD as PMS objects. Low-mass PMS stars are expected to be X-ray bright as result of high levels of coronal activity (e.g. Naylor & Fabian, 1999). In Pozzo et al. (2000), the authors conclude that the low-mass PMS objects are approximately at the same distance and age as  $\gamma^2$  Vel and were likely members of Vela OB2. What was not clear, however, was whether or not the PMS objects represented a increased concentration in the vicinity of  $\gamma^2$  Vel i.e. a subgroup of Vela OB2, analogous to the  $\sigma$  Orionis subgroup in Ori OB 1b association.

If the PMS stars observed towards  $\gamma^2$  Vel are merely low-mass members of Vela OB2, and not associated with  $\gamma^2$  Vel in any other way, we might expect to find a similar number of low-mass PMS stars along other sight lines towards Vela OB2. It is with this in mind that the ROSAT data archives were examined to identify Position Sensitive Proportional Counter (PSPC) pointings directed at other regions within Vela OB2. A 27 ks pointing towards the cataclysmic variable IX Velorum was carried out for Janet Drew in 1992 (ROSAT sequence number RP300289N00). This pointing was of comparable duration to that used by Pozzo et al. (2000) to identify the low-mass PMS in the vicinity of  $\gamma^2$  Vel (25 ks). The target of interest for this pointing, IX Vel, does not actually lie within the 20 arcmin radius of the central region of the PSPC where the point spread function (PSF) is well determined, but rather lies in the outer annulus. The reason for this appears

to be that the pointing was to be used for a timing experiment. Since the ROSAT spacecraft had a deliberate wobble, spurious variability could be introduced by the target source being occulted by the window support structures. By putting the source off-axis this could be avoided as the target's image would then be so large as to make any variation due such occultations negligible (Wood et al., 1995).

The pointing was directed at the coordinates  $(\alpha, \delta)$  08h 19m 26.4s,  $-49^\circ 18' 00.0''$ , which is within approximately  $2.5^\circ$  of  $\gamma^2$  Vel, and within the projected boundaries of Vela OB2 (de Zeeuw et al., 1999). This makes it ideal as a comparison field for checking whether the PMS stars observed by Pozzo et al. (2000) are indeed associated with  $\gamma$  Vel, or if they are in fact part of a more widely distributed PMS population in Vela OB2.

## 2.2 Optical Data

### 2.2.1 Observations

A *VI* imaging survey of 8 13.5-arcmin fields of view (FoVs) near IX Vel was carried out using the 0.9m telescope at the Cerro Tollo Interamerican Observatory (CTIO), Chile on the night of 2002 February 16/17 under photometric conditions. These observations were carried out by Dr. Rob Jeffries and Ms C. R. Devey. The survey fields were selected to cover the central region of the ROSAT PSPC pointing. Each field was observed using a short and a long exposure in each filter. These exposures were 6 and 60 seconds in the *I*-band; 10 and 120 seconds on the *V*-band. The short exposures were obtained to provide reliable photometry for the brighter stars that were saturated in the long exposures. The ROSAT central PSPC FoV is shown in Figure 2.1 along with our survey fields. In addition to the fields of interest a number of Landolt (1992) standard fields were also observed at several times during each evening and at a range of airmasses.

### 2.2.2 Data Reduction and Optimal Photometry

The data were reduced, and photometry was performed using the optimal extraction algorithm originally described by Naylor (1998), with its adaptation for constructing CMDs detailed by Naylor et al. (2002). The standard fields were reduced using the same method as that used for the

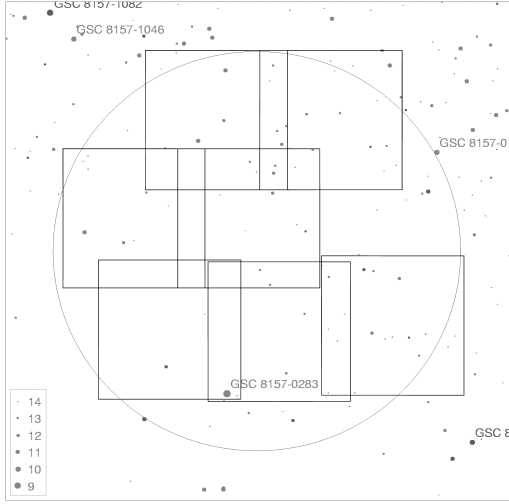


Figure 2.1: The layout of the fields observed near IX Vel. The square boxes outline the 13.5'x 13.5' CTIO 0.9m fields of view, whilst the large circle shows the region covered by the ROSAT PSPC central region.

data frames, which is described below. The instrumental magnitudes and colours for 114 standard star observations were compared to those given by Landolt (1992) to yield zero-points, colour terms and extinction coefficients. An additional magnitude independent uncertainty of 0.02 mags was introduced to the  $V$  band data to give a  $\chi^2$  of 142 for 114 points. No additional uncertainty was required for the  $V - I$  data. This level of uncertainty is consistent with the level of uniformity in the flatfields. The standard stars were drawn from Landolt field numbers SA 95, SA98 and fields centred on the stars G4427, G9742 and TPhe. The colour transformation equations were:

$$V - I = \Psi_{V-I}(v - i) + Z_{V-I} - K_{V-I}X \quad (2.1)$$

$$V - v = \Psi_V(V - I) + Z_V - K_V X \quad (2.2)$$

The lower case roman characters in these equations refer to instrumental magnitudes and colours, i.e. prior to transformation onto the standard system. These equations were solved to find parameters  $\Psi$ ,  $Z$  and  $K$ , where:  $\Psi$  is the colour term;  $Z$  is the zero point;  $K$  is the extinction

coefficient. The values found for these parameters are listed below in Table 2.1. The variable ‘ $X$ ’ is the airmass, as found by the expression  $X = \sec(z)$ , where  $z$  is the zenith distance angle.

Table 2.1: Colour transformation coefficients obtained for the  $VI$  survey in the region near IX Vel.

	$\Psi$	$Z$	$K$
$V$	0.022	22.21	0.132
$V - I$	1.000	1.01	0.0837

Each image was bias subtracted and flatfield corrected using files constructed from twilight sky flatfield images and bias frames taken at the beginning of the same evening as the observations. The subsequent data reduction consisted of a number of steps which are each detailed below. Firstly the offsets between different frames were found. These offsets were then used to allow the identification of stars upon which optimal photometry would be performed. The magnitudes thus obtained were then in the final stages of the data reduction.

### 2.2.2.1 Finding the offsets between the frames

The first stage is to find the offset in pixel space between a master-reference image and a series of other images. This is done by finding the difference in positions of stars between the secondary images and the reference image. During the first part of this process, the reference image is searched for stars by identifying pixels with counts above a given significance. These events are then consolidated into stars. This is done using several passes, the first detecting the most significant but unsaturated events, and the final pass detecting events close to the given significance limit. Positions and magnitudes are then found for 100 of the detected stars using an estimated point spread function (PSF), and an estimate of the seeing in pixels (the full width half maximum, FWHM, of the PSF). The PSF is estimated using the star with the highest non-saturated pixel value. Stars in the secondary images are found in the same way.

When the positions and magnitudes of 100 stars in a secondary image have been obtained, the offset and rotation with respect to the reference image is found by matching the pattern of

stars in the reference image. The detection and pattern matching process is then repeated for each of the remaining secondary images.

The reference image was chosen as the deep image which would be to detect stars. In this case this was the 60 s I-band exposure, since PMS stars we were interested in would be brighter in the redder waveband, and thus easier to detect.

In this case the deep, reference, image in the I-band consisted of a single exposure. However, in cases where the deep image was divided into several shorter exposures the sub-exposures were co-added to produce the reference image, which was then used for object detection (see Chapter 3 for example).

### **2.2.2.2 Object Detection**

After the offsets between the reference image and the rest of the images have been found, the next stage is to produce a list of stars upon which optimal photometry will be carried out. At this stage a list of candidate stars which will be used as a starting point for determining the PSF to be used for the optimal extraction is also obtained.

Initially the deep, reference, exposure, in this case the 60 second I-band frame is searched for stars. First the sky level is measured, and subtracted from each pixel. The sky is measured using sky boxes that are large enough that when the sky determination is subtracted from a star the uncertainty due to sky measurement is small. The sky determined in this manner is then subtracted from each pixel. The image is then smoothed using a top-hat filter with a width defined by the seeing in pixels. Next, all pixels that have values above a given significance threshold are counted and they are consolidated into stars. This is done in a series of passes, starting with the most significant pixels and ending with pixels at the lower threshold. At each pass a list of stars is produced by applying a north-south-east-west connectivity condition to the list of significant pixels, or events. A group of events is only added to the list of stars if it does not contain the central pixel of any other, previously identified, star. Duplicate detections are then removed by checking if any stars lie within a distance equal to the seeing of another star. When duplicates are identified, one of them is removed. As such it is crucial that the seeing is not under-estimated. This can result in the same star being detected twice, and having photometry carried out on both

detections, neither of which are likely to be correctly centred, which will give rise to suspect results.

Before moving on to the short exposure, stars which are likely to have suspect profiles are noted, or flagged. Such stars are unsuitable for use as PSF determining templates, or PSF stars. If a star contains a saturated pixel then it is given a flag that indicates this, a letter ‘S’ is written to its data quality column. When a star contains a pixel (or pixels) that is not saturated but is in the non-linear regime for the detector the data for that star is flagged with a letter ‘L’. Stars which contain pixels with negative counts are flagged with a letter ‘M’.

At this stage a ‘non-stellar’ flag, ‘N’, is introduced. This flag is applied to stars whose profiles are found to be not point-like, and thus whose photometry will be unreliable e.g. a star whose profile is affected by the presence of a close companion. This is determined by assessing if there are any deviations of the stellar profile beyond a certain threshold, as follows. Flux is measured through two masks, one with a FWHM equal to the seeing, and the other with a FWHM equal to half the seeing. The ratio of these fluxes must be within  $3\sigma$  of the median for the star to be accepted. Here,  $\sigma$  is equal to the sum in quadrature of the uncertainty in each measurement and the clipped RMS about the median. The profile used for these extractions is allowed to vary as a function of position on the CCD. The X and Y orders for the polynomial function of position that defines the shape parameter are supplied by the user. After examining the deep exposure, a short exposure is examined. Stars that were previously flagged as non-linear or saturated may offer reliable photometry in the short exposure, and if so they have the relevant data quality flag removed.

The final output of the object detection process consists of two files. One is a list of the positions of all stars detected upon which optimal photometry will be performed. Each star in this list also has a data quality flag associated with it, indicating if the data is likely to be reliable, and if not, why not. Individual pixels are also flagged for quality separately. Pixels that are either too close to the edge of the detector to be reliable or are in an unreliable portion of the detector, are flagged with the letters ‘E’ or ‘R’ respectively. Bad pixels are flagged with the letter ‘F’. Stars which contain pixels which contain any of these flags are also excluded from the list of potential PSF stars. The other file is a list of stars that are suitable for use as a PSF star when defining the mask to use for the optimal extraction. These are stars which are neither saturated nor have another suspect data quality flag associated with them. The principal reason for applying data

quality flags at this stage to allow for the selection of good PSF stars. Stars that are flagged at this stage may have good quality data in frames other than the reference frame, but since this is not known at this point they must be discarded from the list of candidate PSF stars.

### 2.2.2.3 Optimal photometry

Optimal extraction is performed using the algorithm described in detail in Naylor (1998). A brief description of its key features will be provided here for completeness. In optimal extraction each pixel is taken as an independent estimator of the flux in the profile. That is, assuming the profile is well estimated, by measuring the flux in a given pixel and comparing it to the fraction of the total flux expected in that pixel one can estimate the total flux in the profile. This extraction of the total flux is optimised by weighting the flux estimates from each pixel by the inverse of the square of their uncertainties before combining them. Naylor (1998) demonstrates that even if the model profile used for the extraction is not a precise description of the real profile the relative flux will still be correct, but some signal-to-noise will be lost.

The first step to determining the optimum weight mask for each star, and thus extracting the flux estimate, is determining the PSF. This process begins with selecting a star whose PSF will be fitted. The brightest 49 stars from the list of potential PSF stars (those that were unflagged in the reference frame) are selected and fitted with elliptical Gaussians. The star whose geometric mean FWHM is the median of that list is used for fitting the PSF. The PSF is then estimated by fitting a two dimensional Gaussian to the PSF star. This, in combination with estimates of the variance in the pixels, is used to construct the optimum weight mask for each star and the fluxes are then extracted for all stars that have been identified. The sky level is determined locally for each star by constructing a histogram of the distribution of sky pixel values. This histogram is then fitted to obtain the sky estimate, and its uncertainty.

At this stage a number of additional data quality flags can be applied to the data. Two of these are associated with sky determination that is required for estimating the variance of the pixels. These flags are the ill-determined sky flag (I), and the ‘background fit failed’ flag (B). The ‘I’ flag indicates that the stars photometry is likely to have been affected by a poorly determined sky histogram. This flag is invoked when the fit to the sky histogram has a reduced  $\chi^2 > 3$ . The

‘B’ flag is applied when the fit to the sky is has failed. This can happen for several reasons. For example, there may not have been enough data to fit, alternatively, all the sky counts may have fallen into a single bin on the histogram.

#### 2.2.2.4 Final stages

The final stages of the data reduction are profile correction; combining measurements from different images in the same group to arrive at instrumental magnitudes and colours for each star; applying the colour transformation coefficients; performing astrometry; combining catalogues from different FoVs to arrive at the final catalogue.

The purpose of profile correction is to correct for differences between the mask used for optimal extraction and true stellar profile. If the extraction mask were a completely accurate representation of the PSF then the profile correction would always be zero. However, since the true PSF is unlikely to be an elliptical Gaussian it is common that some correction will need to be made. The profile correction is measured by comparing the magnitude obtained using the optimal extraction mask with that obtained using a large aperture. The profile correction that is applied is modal value found from 80 candidate stars with good data quality and  $S/N > 10$ . A typical set of profile corrections for 80 candidate stars is shown as a function of x-position in Figure 2.2. As can be seen there, the profile correction is spatially variant. As such the profile corrections are fitted with a low-order polynomial function after removing those objects where the presence of a nearby star has given an anomalous correction. Figure 2.3 shows the residuals about a low-order polynomial fit to the profile corrections.

At this stage, photometry from each image has already been put into magnitude space. The 2-dimensional polynomial function described above is used to apply the profile correction to all stars from each image. Data from each image are then corrected to the mean airmass for the group using the coefficients derived at beginning of this section. The same magnitude independent uncertainty as that required for the standard stars is now introduced to the data, in this case an additional 0.02 mags uncertainty in the  $V$  band. Prior to combining the measurements from different images the relative transparency correction for each frame is determined. One of the frames in each waveband is arbitrarily assigned as the master frame. The transparency correction

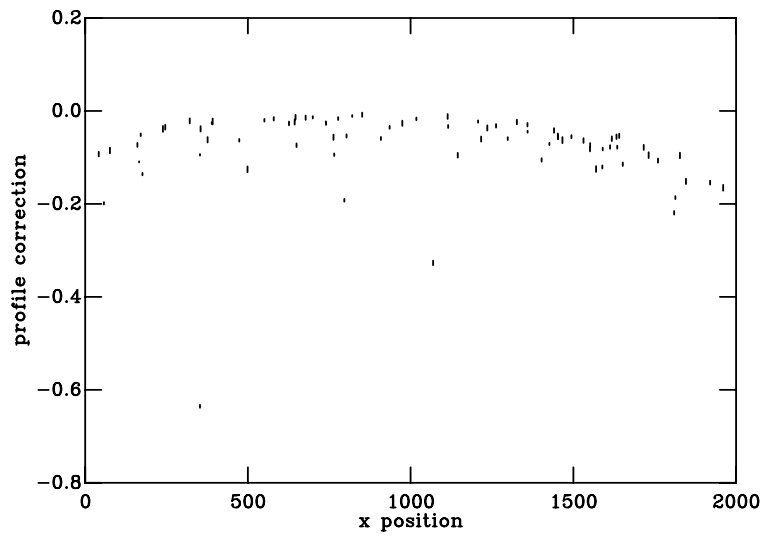


Figure 2.2: The typical profile corrections as a function of x-position on the CCD image. A variation of profile correction with position is apparent.

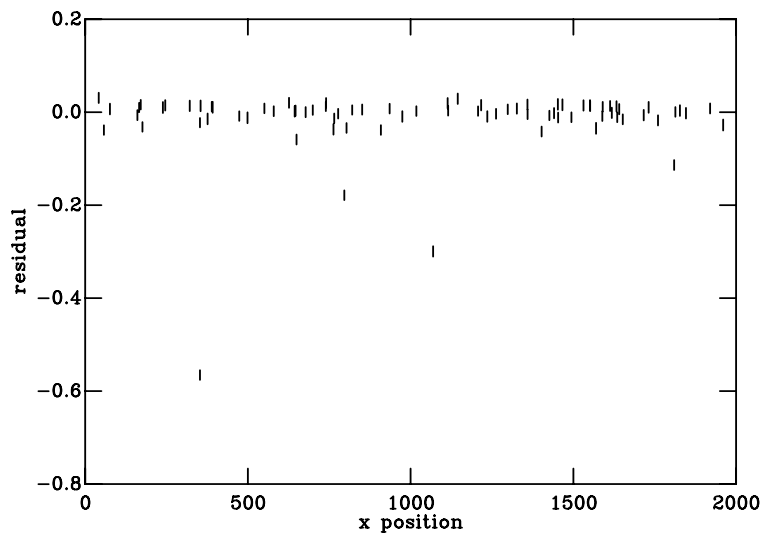


Figure 2.3: Typical residuals of profile corrections from a low-order polynomial fit.

for each frame is taken as the weighted mean of the differences between the magnitudes of good data quality stars in that frame and the master frame. Each frame is corrected by its relative correction multiplied by  $N/(N + 1)$ , where  $N$  is number of frames. The master frame is corrected by mean transparency correction. A data quality flag, ‘C’ (cloudy), may be applied to indicate when a large relative transparency correction has been used. The threshold for the application of this flag must be determined with reference to the conditions the data were taken under. Since the images for this project were taken close together under photometric conditions, and there were only two per waveband, this threshold was not set in this case, and the flag was neglected.

Measurements of each star from different images are combined by finding the weighted mean in flux space. As part of the same process the reduced  $\chi^2$  for each star is calculated, and these are plotted for the  $V$  band data as a function of S/N in Figure 2.4. In this case there was only a long and a short exposure in each waveband, so this plot is based only on two observations, but it does indicate that the calculated uncertainties a good reflection of the true uncertainties in the data. If the magnitude independent, systematic, uncertainty added earlier is set to the wrong value it can be diagnosed by inspection of this plot. If the value added is too small the distribution of points will rise to higher values of reduced  $\chi^2$  as one moves to higher S/N. Conversely, if the introduced systematic uncertainty is too large, the distribution will fall to lower values of reduced  $\chi^2$  at high S/N. Data for stars with a high value of  $\chi^2_{\nu}$  may need to be treated with caution, either due to cosmic ray hits on one of the images, or due to real, source, variability. As such, a data quality flag is sometimes applied to indicate which objects’ data indicate variability. Since this flag indicates possible variability, it is denoted with the letter ‘V’. This flag is applied when the value for  $\chi^2_{\nu}$  for an object falls above some given threshold.

The next task to be performed is that of obtaining an astrometric solution. Astrometry was performed by matching stars in the optical catalogues with those in reference catalogues of the same fields of view. In this case the SuperCosmos sky survey was used to provide the reference catalogues. A six coefficient model is then used to perform the transformation from pixel coordinates to J2000.0 equatorial coordinates. The RMS of the residuals about the six-coefficient were all less than 0.3 arcsec.

After celestial coordinates were obtained for all objects in each field, the individual catalogues could be combined to form the final optical catalogue. This process is referred to as normalisation.

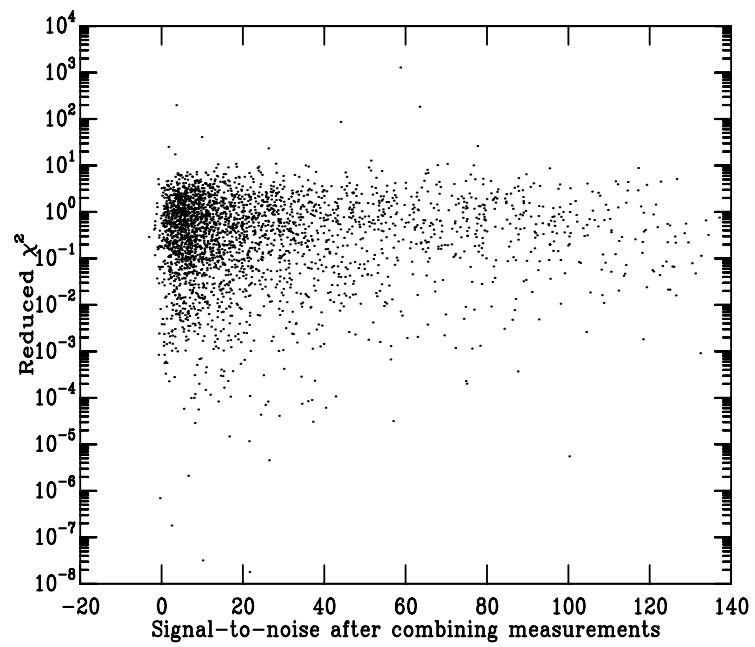


Figure 2.4: A plot of  $\chi^2$  for each star in the long and short  $V$  band exposures for field 1.

As can be seen in Figure 2.1 the different FoVs were directed such that there were overlap regions between the fields. These overlap regions facilitate the normalisation of all fields onto a single system, and also allow for a check of the internal consistency of the photometry. The normalisation is carried out as follows. Firstly the mean weighted difference between the stars in each overlap region is calculated. Then additional transparency corrections are applied to each field so as to minimise the RMS of the differences in the overlap regions, whilst keeping the mean of corrections zero. After this process it was found that the remaining RMS of the differences in the overlaps was 0.006 mag in this case. This is a measure of the internal consistency of the photometry. The mean magnitudes and colours for the overlap stars are then carried forward, while their co-ordinates are taken from only one field.

The catalogues for each field were thus combined to produce an optical catalogue for the entire region covered by our survey, listing positions,  $V$  magnitudes and  $V - I$  colours for 29 645 stars<sup>1</sup>. A sample of the full catalogue is given in Table 2.3. It can be seen that the uncertainties for many stars' magnitudes are smaller than the 0.02 magnitude systematic uncertainty that was added during data reduction. This is because the magnitudes, and uncertainties, listed in Table 2.3 have been obtained by combining measurements from more than one image, whilst the systematic uncertainty was introduced to the data for individual images. The CMD for this catalogue is shown in Figure 2.5. The densest region of this diagram corresponds to the population of galactic main-sequence background stars. Two 'fingers' branch out from this portion of the CMD toward bluer and brighter magnitudes and redder and brighter magnitudes. The bluer 'finger' corresponds to brighter main-sequence stars, whilst the redder 'finger' corresponds to the red giant branch. A summary of the data quality flags applied during the data reduction is shown in Table 2.2. The final column of this table indicates if a flag is strong or weak, i.e. if it will overwrite previous flags or not. The flags are listed with the data for a star as two characters, the first corresponds to the first waveband data (in this case  $V$ ), the second to the second waveband data ( $I$ ).

---

<sup>1</sup>The full catalogue is available from the cluster collaboration photometric catalogue page: <http://www.astro.ex.ac.uk/people/timn/Catalogues/description.html>

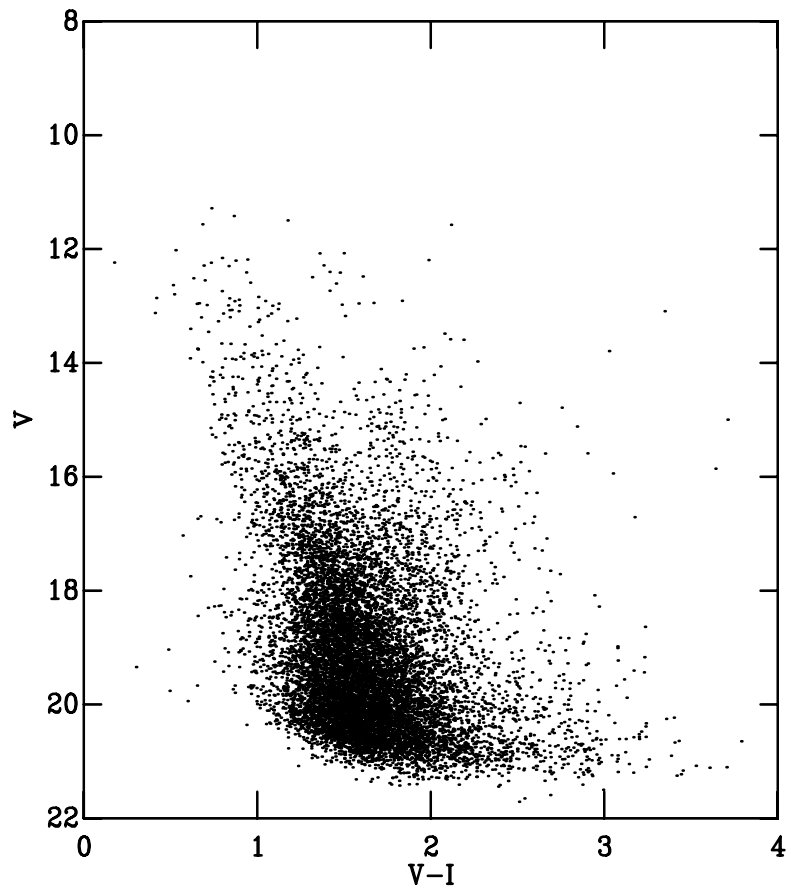


Figure 2.5: The CMD for the fields observed near IX Vel. Only stars with  $S/N > 10$  and good data quality are displayed.

Table 2.2: A summary of data quality flags and their meanings.

Flag	Flag Name	Algorithm	Type
O	O.K	N/A	N/A
S	Saturated pixel	Pixel flagging	Strong
L	Counts above pixel linearity limit	Pixel flagging	Strong
F	Bad pixel	Pixel flagging	Strong
R	Uncalibrated region	Pixel flagging	Strong
E	Too close to CCD edge	Position fitting	Strong
N	Non-stellar	Star shape estimator	Strong
B	Background fit failed	Sky determination	Strong
I	Ill-determined background	Sky determination	Weak
P	Position fit failed	Flux measurement	Weak
E	Too close to edge	Flux measurement	Strong
M	Negative (minus) counts	Flux measurement	Weak
A	Absent input data	Data input to calibration	Strong
H	Poor profile correction	Profile correction	Strong
V	Variable	Combining image catalogues	Strong
C	Large relative transparency correction (cloudy)	Combining image catalogues	Strong

Table 2.3: A sample of the full photometric catalogue for the survey region near IX Vel. The full catalogue is available from the cluster collaboration catalogue page<sup>3</sup>. Quality flags: 1<sup>st</sup> character is the quality flag for the star in the V band, the 2<sup>nd</sup> is for the I band. The meanings of the flags are: (O) O.K, (N) Non-stellar, (E) star too close to CCD Edge, (B) Background fit failed, (S) Saturated, (I) Ill determined sky, (V) Variable, (F) bad (Flagged) pixel, (M) negative (Minus) counts, (C) large relative transparency correction (Cloudy).

Field No.	Index No.	$\alpha$ (J2000)	$\delta$ (J2000)	X	Y	V	$\sigma_V$	Quality	V-I	$\sigma_{V-I}$	Quality
1.00	178	08 19 23.935	-49 31 3.50	709.124	1718.122	17.893	0.040	NI	2.482	0.048	NI
1.00	179	08 19 38.548	-49 31 26.83	354.439	1776.469	16.175	0.007	OO	1.453	0.010	OO
1.00	180	08 18 44.920	-49 31 29.59	1656.132	1784.012	16.849	0.011	OO	1.382	0.016	OO
1.00	181	08 19 27.347	-49 32 7.92	626.387	1878.698	15.429	0.009	OO	1.275	0.013	OO
1.00	182	08 18 39.392	-49 32 10.55	1790.090	1886.393	16.600	0.008	OO	1.385	0.011	OO
1.00	183	08 19 38.625	-49 32 21.97	352.723	1913.912	15.228	0.006	OO	1.255	0.009	OO
1.00	184	08 18 48.474	-49 32 21.96	1569.646	1914.382	16.300	0.010	OO	1.317	0.015	OO
1.00	185	08 18 32.246	-49 32 39.45	1963.321	1958.848	16.913	0.012	OO	1.712	0.016	OO
1.00	186	08 18 49.863	-49 32 44.52	1535.854	1970.539	17.128	0.012	OO	2.311	0.016	OO
1.00	187	08 18 43.783	-49 32 52.72	1683.333	1991.264	16.532	0.011	OO	1.251	0.016	OO
1.00	188	08 18 51.011	-49 32 53.30	1507.979	1992.367	17.180	0.012	OO	2.314	0.016	OO
1.00	189	08 19 26.395	-49 33 10.28	649.540	2034.127	16.511	0.022	NN	1.407	0.032	NN
2.00	91	08 18 33.469	-49 19 36.07	257.355	73.092	17.015	0.012	OO	1.464	0.017	OO
2.00	245	08 18 30.150	-49 19 35.41	338.244	71.349	18.201	0.016	OO	1.433	0.024	OO
5.00	554	08 19 25.915	-49 19 39.01	1125.708	1699.977	18.195	0.050	OO	1.827	0.052	OO
5.00	555	08 19 9.944	-49 19 38.47	1515.005	1699.057	18.354	0.017	OO	1.422	0.025	OO
5.00	558	08 19 25.800	-49 19 44.90	1128.495	1714.635	18.493	0.044	OO	1.722	0.046	OO
5.00	559	08 18 47.700	-49 19 45.57	2057.147	1717.961	18.290	0.012	OO	1.680	0.017	OO
1.00	198	08 18 44.936	-49 19 46.39	1659.046	31.365	16.915	0.012	OO	1.262	0.017	OO
1.00	199	08 18 37.711	-49 19 46.35	1835.119	31.642	18.073	0.016	OO	1.272	0.025	OO
1.00	200	08 18 55.789	-49 19 47.78	1394.575	34.394	18.424	0.013	OO	1.483	0.019	OO
1.00	201	08 19 4.701	-49 19 50.41	1177.373	40.701	17.021	0.009	OO	1.332	0.012	OO
1.00	202	08 19 51.134	-49 19 50.10	45.861	40.372	22.206	0.254	OV	5.427	0.254	OV

## 2.3 X-Ray Data

The ROSAT data set was retrieved from the public archives via the LEDAS website (<http://ledas-www.star.le.ac.uk/rosat/>) hosted by Leicester University. The data were reduced using Asterix Version 2.3-b1, a suite of X-ray reduction programs available from the University of Birmingham (via URL <http://www.sr.bham.ac.uk/asterix/>). The data were cleaned (using the supplied house-keeping files) so that events recorded during periods of high background or poor aspect quality were excluded from the data used to construct the final image. The data were then sorted into a 20 arcminute radius image cylinder (spectral data was retained at this stage), selecting corrected pulse height (PHA) channels 11 to 201. The resulting image cylinder, with an effective exposure time of 26.4 ks, was then visually inspected and obvious sources masked in duplicate images, which was then used to create a background image cylinder. This was then used, along with the other calibration files supplied with the data set, to create a background model. This, and the unmasked image cylinder, were then projected to create a 2-d image and background model, which were used to search for sources using Cash-statistic maximisation in the PSS algorithm (Saxton et al., 2000). The resulting source list was then used to further mask sources in the background spectrum to produce a refined background model, and the image was searched for sources again. This process identified 27 sources in the ROSAT PSPC FoV. These sources are listed in Table 2.4.

Table 2.4: The ROSAT source list. X and Y are positions in the PSPC FoV.

Index No.	$\alpha$ (J2000)	$\delta$ (J2000)	X	Y	Raw Flux (counts)	Optical counterpart field no.	Star no.
1	08 18 14.80	-49 27 14.00	-0.190	-0.150	147.045	2.00	55
2	08 18 15.90	-49 13 22.00	-0.190	0.080	298.360	*.**	****
3	08 18 22.60	-49 08 19.00	-0.170	0.160	187.905	8.00	66
4	08 18 33.50	-49 24 13.00	-0.140	-0.100	300.960	1.00	27
5	08 18 46.90	-49 09 50.00	-0.110	0.140	38.912	8.00	231
6	08 18 50.30	-49 32 42.00	-0.100	-0.250	75.712	1.00	186
7	08 18 51.50	-49 02 33.00	-0.100	0.260	116.235	8.00	24
8	08 18 53.60	-49 12 22.00	-0.090	0.090	75.712	5.00	27
9	08 18 58.60	-49 21 16.00	-0.080	-0.050	67.744	1.00	92
10	08 18 59.30	-49 30 44.00	-0.070	-0.210	56.900	1.00	1243
11	08 19 7.90	-49 19 19.00	-0.050	-0.020	45.582	5.00	190
12	08 19 11.60	-49 07 9.00	-0.040	0.180	37.574	7.00	50
13	08 19 13.10	-49 35 1.00	-0.040	-0.280	241.856	*.**	****
14	08 19 15.90	-49 09 15.00	-0.030	0.150	34.794	8.00	70
15	08 19 27.00	-49 19 56.00	0.000	-0.030	45.351	5.00	4085
16	08 19 30.90	-49 09 1.00	0.010	0.150	288.562	7.00	59
17	08 19 31.20	-49 28 46.00	0.010	-0.180	77.948	1.00	417
18	08 19 46.10	-49 32 51.00	0.050	-0.250	246.063	1.00	71
19	08 19 58.30	-49 27 10.00	0.090	-0.150	101.015	3.00	55
20	08 20 18.80	-49 24 5.00	0.140	-0.100	40.602	3.00	2741
21	08 20 19.00	-49 35 12.00	0.140	-0.290	131.579	*.**	****
22	08 20 21.90	-49 33 0.00	0.150	-0.250	265.171	3.00	4470
23	08 20 31.60	-49 30 54.00	0.180	-0.220	90.579	3.00	609
24	08 20 52.00	-49 22 24.00	0.230	-0.070	1107.584	3.00	36
25	08 20 53.90	-49 27 38.00	0.240	-0.160	101.850	3.00	519
26	08 21 6.80	-49 16 24.00	0.270	0.030	308.753	4.00	47
27	08 21 7.70	-49 11 52.00	0.280	0.100	109.222	4.00	28

## 2.4 Identification of X-ray sources

The optical catalogue was cross-correlated with the X-ray catalogue to produce a catalogue of optical sources with counterparts on the X-ray catalogue. A bore-sight correction of +2 arcseconds in right ascension and +3 arcseconds in declination was applied. Using a search radius of 10 arcseconds 24 out of the 27 X-ray sources were correlated with the optical catalogue. This is a similar proportion to that found by Pozzo et al. (2000), who found that 77 out of 83 sources correlated. The optical counterparts for the matched X-ray sources are shown below in Figure 2.6. Only those counterparts with good photometry and a signal-to-noise ratio above 10 are shown.

## 2.5 Discussion

Inspection of Figure 2.6 indicates that there appears to be a group of PMS stars at a similar age and distance to that seen in Figure 2.7 for the  $\gamma$  Vel field. However, they are far fewer in number than those observed by Pozzo et al. (2000). The low number of X-ray detected PMS stars, in addition to no visible PMS on the CMD makes it unfeasible to fit isochrones in this case. However, a 5 Myr D’Antona & Mazzitelli (1997) isochrone is overlaid on Figure 2.6 to demonstrate that the location of the X-ray selected objects is consistent with age and distance of Vela OB2.

There are 19 X-ray bright stars in the expected PMS region of the CMD for this survey compared with 57 in the same region of the  $\gamma$  Vel CMD. These X-ray detected stars are found to be evenly distributed across the field of view, with no indication of structure. Only 17 of the likely PMS objects are displayed in Figure 2.6. This is because one (7.00-50) has a suspect data quality flag (F), and the other (3.00-4470) has large uncertainties due to its faintness ( $V = 23.53 \pm 0.58$ ). As can be seen in Table 2.4, the latter of these has the 5th highest X-ray flux in the sample.

For the purposes the following discussion I will assume the distance to Vela OB2 is 410 pc as found by de Zeeuw et al. (1999). I will also assume that it has the age of the PMS stars identified by Pozzo et al. (2000), 4 Myrs. The de Zeeuw et al. (1999) study identified 81 B star members of Vela OB2 in a region with a  $5^\circ$  radius. If we assume a Salpeter (1955) IMF, we can use the B star count to estimate how many PMS stars in a given mass range we would expect to find in our survey region if stars were distributed uniformly across the association. At the adopted distance and age

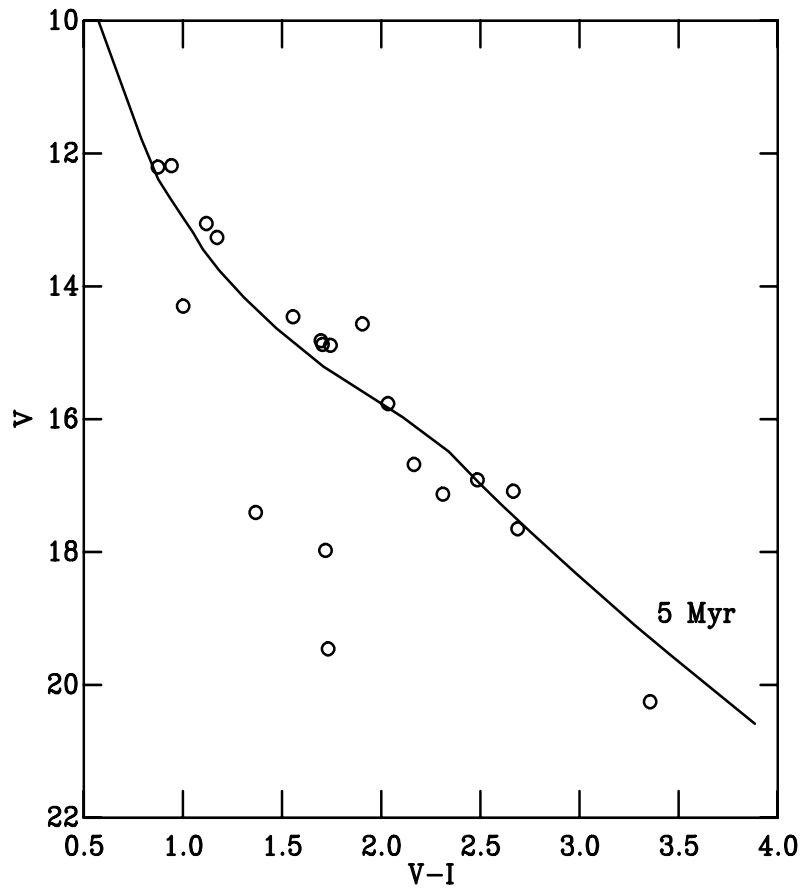


Figure 2.6: CMD for the optical counterparts to the X-ray objects identified in the ROSAT PSPC data. A 5 Myr D'Antona & Mazzitelli (1997) isochrone, scaled to the Hipparcos distance to Vela OB2 of 410 pc (de Zeeuw et al., 1999) is also shown.

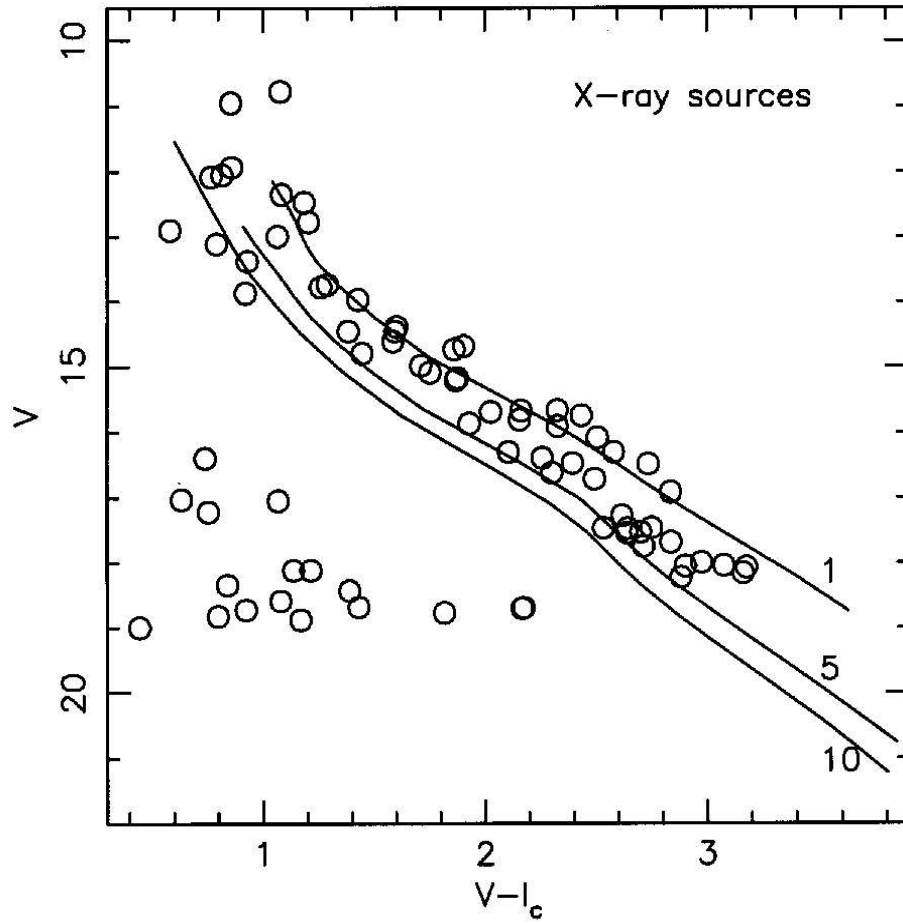


Figure 2.7: From Pozzo et al. (2000). The location on a  $VI$  CMD of X-ray sources matched with stars in the optical catalogue centred on  $\gamma$  Vel.

the magnitude range  $15 < V < 18$  corresponds to a mass range of roughly  $0.3M_{\odot} < M < 0.75 M_{\odot}$ , using the isochrones of D’Antona & Mazzitelli (1997). We would expect to find 5 PMS stars in this mass range in our survey region. In reality there are 6 X-ray bright stars in the appropriate region of our CMD. The equivalent plot by Pozzo et al. (2000) shows 27 X-ray bright PMS stars in the appropriate region of their CMD. This suggests that the objects identified in this study form part of the general population of PMS stars from the Vela OB 2 group. This is further supported by their proximity to the 5 Myr D’Antona & Mazzitelli (1997) isochrone scaled to the Hipparcos distance to Vela OB2 (see Figure 2.6. It would seem fair to suppose that the higher number of PMS stars observed by Pozzo et al. (2000) represent a concentration of stars in the region of  $\gamma^2$  Vel. Concentrations of low-mass members of OB associations in the vicinity of high mass members have been observed elsewhere. For example, in the Orion OB1b association, a significant concentration of low-mass PMS objects has been identified in the vicinity of the O-star  $\sigma$  Orionis (e.g. Wolk, 1996). Similar concentrations have also been found in the vicinity of  $\alpha$  Persei (e.g. Lodieu et al., 2005) and  $\lambda$  Orionis (Dolan & Mathieu, 2001).

## 2.6 Conclusions

An optical *VI* imaging survey of a region coincident with a 25 ks ROSAT PSPC pointing within the Vela OB2 association was carried out with a view to searching for PMS objects, and comparing the number found here with that found by Pozzo et al. (2000). Nineteen possible PMS stars were identified by their X-ray emission and their location on a CMD, compared to 57 identified by Pozzo et al. (2000). Using a Salpeter IMF it was concluded that the number of PMS stars identified here was consistent with expected PMS population of Vela OB2. In contrast, by the same reasoning the number identified in the vicinity of  $\gamma^2$  Vel by Pozzo et al. (2000) represents a high concentration of PMS stars. This supports the proposal that there is a low-mass PMS association surrounding  $\gamma^2$  Vel.

## 3 On the nature of Collinder 121: insights from the low-mass pre-main sequence

### 3.1 Introduction

In Chapter 2 the use of the *VI* CMD in conjunction with X-ray observations to identify PMS objects was explored. In this chapter this theme will be extended. Here a *VI* CMD and X-ray observations are used to identify low-mass PMS objects. Their distribution in colour-magnitude (C-M) space is then compared to theoretical isochrones for different ages to discern information regarding age and distance. The following work has been published as a paper in the Monthly Notices of the Royal Astronomical Society (MNRAS) (Burningham et al., 2003).

Collinder 121 (Cr 121) is listed in the New List of OB Associations (Melnik & Efremov, 1997) as an OB association at a distance of 540 pc. However, since its first identification as an open cluster of about  $1^\circ$  diameter by Collinder (1931), Cr 121 has had its membership re-assessed a number of times. In this chapter we use the low-mass pre-main sequence (PMS) to resolve the long standing controversy over the nature of Cr 121, and demonstrate the power of the using the low-mass PMS to pick apart structure in OB associations. We also illustrate the difficulties associated with using proper motion and parallax data of limited range in isolation.

The cluster was first discovered as a group of 18-20 main-sequence B stars found within a  $40 \times 60$  arcminute box. Collinder (1931) used the cluster diameter, along with mean separation of stars within it, to derive a distance of 1260 pc. Feinstein (1967) studied the cluster using UBV photometry and extended the membership to 40 stars brighter than  $V = 7$  within a  $10^\circ \times 10^\circ$  box. This group was characterised as an OB association and the position of the zero age main sequence (ZAMS) indicated a distance of 630 pc. Already, two very different structures had been described by different authors. Eggen (1981) suggested that the original compact group and the larger OB association may be distinct. Using intermediate band and  $H\beta$  photometry Eggen (1981) placed the compact group, which he referred to as Cr 121, at a distance of 1.17 kpc at an age of 1.5 Myrs. The more diffuse group, which Eggen referred to as CMa OB2, was found to be at a distance of 740 pc.

More recently emphasis has been placed on the use of common motion criteria for defining

cluster and association memberships. de Zeeuw et al. (1999) used Hipparcos proper motion and parallax data to select a moving group in the direction of Cr 121. They selected 103 stars in a region  $13^\circ \times 16^\circ$  in extent, and find a mean distance of  $592 \pm 28$  pc. The presence of an O-star, a Wolf-Rayet (WR) star and early type B stars in the membership list led to an estimated age of  $\sim 5$  Myr. Since stars were selected from a large region of sky compared to the original boundaries of the distant interpretation of Cr 121, and the fact the Hipparcos parallaxes become unreliable at about 1 kpc, this selection method is biased to detecting a larger, more diffuse foreground association rather than the distant compact cluster of Collinder (1931). If both groups were present, as suggested by Eggen (1981), only the foreground association would be detected as this would represent a large number of stars with common motion at a similar distance, within the reliable domain of Hipparcos parallaxes. Dias et al. (2001) used data from the Tycho2 catalogue to re-determine the mean proper motion of Cr 121, amongst other clusters. This study was restricted to open clusters within 1 kpc, so again was biased to only detecting the foreground group, and would have been insensitive to any more distant cluster along the same line of sight. Apparently working within the assumption of the de Zeeuw et al. (1999) view of Cr 121 and the Dias et al. (2001) membership list, Dias et al. (2002) determine the distance to Cr 121 as 470 pc with an age of 11 Myr.

Kaltcheva (2000) carried out Strömrgren and  $H\beta$  photometry of bright B stars within a  $5^\circ$  radius of the classical centre  $(l, b) = (235.4^\circ, -10.4^\circ)$  of Cr 121. This revealed a group of stars at 660-730 pc, with characteristics similar to an OB association, and a more compact group of stars at a distance of 1085 pc, which she calls Cr 121. This would indicate that the original cluster Cr 121 is situated at a distance of over 1 kpc, whilst the Cr 121 selected by de Zeeuw et al. (1999) is a less distant OB association.

Inspection of the ROSAT Position Sensitive Proportional Counter (PSPC) catalogue revealed a number of X-ray point sources in the vicinity of WR 6, near the centre of the region studied by Kaltcheva (2000) and the original centre of Collinder's cluster. WR 6 is listed as a member of Cr 121 by de Zeeuw et al. (1999), but not by Kaltcheva (2000). The Hipparcos parallax for WR 6 of  $\pi = 1.74 \pm 0.76$  mas, puts it at a distance of 575 pc.

As described in Chapter 1, since low-mass PMS stars are expected to be X-ray bright due to high levels of coronal activity, X-ray data can be used as a diagnostic tool for identifying low-mass PMS stars (e.g. Naylor & Fabian, 1999; Pozzo et al., 2000). The presence of low-mass PMS stars

would allow us to fit isochrones to the PMS in a CMD, constraining the distance and age of the PMS. With this in mind we have obtained deep  $VI$  imaging photometry of a region  $20'$  in radius, covering the central region of the ROSAT PSPC field of view (FoV) for the pointings carried out towards WR 6. Since the optical data were obtained, XMM-Newton data for this region of sky became available, allowing us to perform a more sensitive X-ray selection of PMS stars.

The layout of our optical survey is shown in Figure 3.1, along with the location of the B stars identified as being members of the more distant group by Kaltcheva (2000) and WR 6. Although our survey region coincides with only two of the B stars identified by Kaltcheva (2000) as members of the more distant cluster, and lies towards the edge of the region enclosed by them, we would still expect to find a significant number of low-mass PMS stars from that group within our survey. Studies of other young clusters and OB associations have always revealed O and B stars located within a sea of low-mass PMS stars, not low-mass PMS stars just within a region enclosed by higher mass stars (e.g. Dolan & Mathieu, 2001; Pozzo et al., 2003).

## 3.2 Optical data

### 3.2.1 Observations

The  $VI$  CCD imaging of 8  $13.5'$  FoVs centred on WR 6 was carried out using the 0.9m telescope at CTIO in Chile on the night of 12/13 February 2002. These observations were carried out by Dr. Rob Jeffries and Ms C. R. Devey.

The FoVs were selected to cover the central region of the ROSAT PSPC pointings. Each field was observed with short (10, 6 seconds) and long exposures (300, 180 seconds) in the  $V$  and  $I$  bands in photometric conditions. The short exposures were aimed at capturing the brighter stars in each field, which would be saturated in the long exposures. To reduce the number of cosmic ray hits in any one image the long exposures were split into three parts, of 100s in  $V$  and 60s in  $I$ . The fields were overlapped with each other to provide a check for the internal consistency of the photometry (see section 2.2). A number of Landolt (1992) standard star fields, containing standards with  $-0.6 \leq V - I \leq 5.8$ , were also observed at several times during the night. This ensured adequate calibration over the colour range of interest.

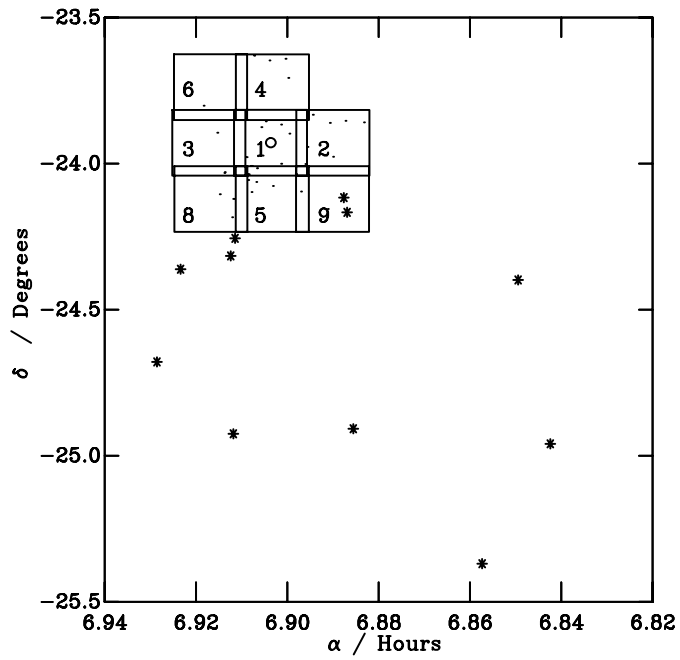


Figure 3.1: The Layout of the fields observed towards WR 6. The square boxes outline the 13.5'x 13.5' CTIO 0.9m fields of view. The 11 B stars listed as members of the more distant association described by Kaltcheva (2000) are marked as asterisks. WR 6 is marked with a circle. The PMS objects discovered here are marked with dots.

### 3.2.2 Data reduction and optimal photometry

The data were reduced, and photometry was performed using the optimal extraction algorithm originally described by Naylor (1998) with its application for constructing CMDs described in depth by Naylor et al. (2002). The software used to perform this task is described in Chapter 2. The standard star fields were reduced using the same algorithm. The instrumental magnitudes and colours for 116 standard star observations were compared to those given by Landolt (1992) to yield zero-points, colour terms and extinction coefficients using equations 2.1 and 2.2. The values for the coefficients are listed below in Table 3.1. We found that an additional, magnitude independent, uncertainty of 0.02 mag was required to give a  $\chi^2$  of 116 for the  $V$  band calibration. No such adjustment was required for  $V - I$ .

Table 3.1: Colour transformation coefficients obtained for the  $VI$  survey towards Cr121.

	$\Psi$	$Z$	$K$
$V$	0.0283	22.12	0.128
$V - I$	0.998	0.947	0.0834

The data reduction method used here is described in detail in Chapter 2. Each image was bias subtracted and flatfield corrected, using files constructed from twilight sky flatfield images and bias frames taken at the beginning of the same evening as the observations. The I-band images were combined (after determining their offsets) before using the deep co-added image for object detection. Optimal photometry was then carried out on the list of stars produced by the detection software to produce an optical catalogue for each FoV. Although the I-band images were combined for object detection, photometry was carried out on the individual frames. This ensured that good signal-to-noise in one frame was not swamped by poor signal-to-noise in another when the images are combined. The individual measurements of each star were combined later, weighting each measurement according to its signal-to-noise.

An astrometric solution was obtained through comparison of the optical catalogues with SuperCosmos catalogues (Hambly et al., 2001) of the same FoVs. The RMS of the 6-coefficient

fit were approximately 0.2 arcsec. The resulting catalogues were then combined to produce an optical catalogue for the entire region covered by our survey, listing a position, a  $V$  magnitude, a  $V - I$  colour and a data quality flag (see Chapter 2) for 26104 stars. The overlap regions between the fields were used to assess the internal consistency of the optimal photometry, which was found to be consistent at the 0.005 mag level. A sample of the final catalogue given as Table 3.2, with the full catalogue available via the CDS online database and the cluster collaboration catalogue page<sup>1</sup>. The resulting CMD is shown below in Figure 3.2. As was seen in Figure 2.5, the galactic background main-sequence population is visible on this diagram, as is the red giant branch. The main-sequence background is visible as the bluer of the two ‘fingers’ that emerge from the densest region of the diagram, whilst the red giant branch is the redder ‘finger’. A population of PMS stars is clearly visible on the CMD of the optical catalogue, lying redward of the background contamination.

---

<sup>1</sup><http://www.astro.ex.ac.uk/people/timn/Catalogues/description.html>

Table 3.2: A sample of the full photometric catalogue, which is available on-line from the CDS and the cluster collaboration catalogue page. Quality flags: 1<sup>st</sup> character is the quality flag for the star in the V band, the 2<sup>nd</sup> is for the I band. The meanings of the flags are: (O) O.K, (N) Non-stellar, (E) star too close to CCD Edge, (B) Background fit failed, (S) Saturated, (I) Ill determined sky, (V) Variable, (F) bad (Flagged) pixel, (M) negative (Minus) counts.

Field No.	Index No.	$\alpha$ (J2000)	$\delta$ (J2000)	X	Y	V	$\sigma_V$	Quality	V-I	$\sigma_{V-I}$	Quality
9.00	3061	06 52 59.493	-24 08 58.44	1940.396	1271.814	21.660	0.933	MO	0.987	0.986	MO
2.00	2224	06 52 59.504	-23 52 0.84	1886.245	434.454	21.023	0.511	OO	0.574	0.539	OO
2.00	1028	06 52 59.506	-23 53 15.15	1885.973	619.683	18.706	0.088	OO	0.790	0.095	OO
2.00	1201	06 52 59.506	-23 55 37.23	1885.625	973.810	19.854	0.040	OO	1.044	0.059	OO
9.00	988	06 52 59.515	-24 05 17.67	1940.311	721.652	19.131	0.018	OO	0.857	0.034	OO
9.00	1600	06 52 59.534	-24 00 56.51	1940.473	70.826	24.385	2.898	OO	4.619	2.892	OO
9.00	930	06 52 59.541	-24 04 12.70	1939.621	559.756	21.411	3.731	NN	0.670	3.882	NN
9.00	2814	06 52 59.545	-24 07 26.56	1938.916	1042.858	24.520	1.007	OV	4.934	1.007	OV
2.00	4088	06 52 59.548	-24 02 37.41	1883.104	2021.075	21.370	0.706	NN	1.462	0.911	NN

### 3.3 X-Ray data

#### 3.3.1 ROSAT data

Nine pointings of the ROSAT PSPC were made towards WR 6 between 1991 and 1992, totalling 28 ks. The data set for each pointing was retrieved, sorted and a refined background model constructed for each as described in Chapter 2. The refined background models were then co-added. The images for each pointing were also co-added to produce an image for source detection with an effective exposure time of 25.8 ks. This image and the background model were then used to search for sources using the PSS algorithm, returning 39 X-ray sources. The archival release of XMM-Newton observations of this region of sky means that much of the data in this source list has been superseded in sensitivity and positional accuracy. As a result we retrieved the XMM-Newton data and removed from the ROSAT PSPC source list those objects that appeared in both sets of data.

#### 3.3.2 XMM-Newton data

Data from two XMM-Newton observations using the European Photon Imaging Camera (EPIC) were used to make the X-ray source catalogue. One directed at WR 6 with 12864 second total integration time during revolution 346 (Skinner et al., 2002), and another of 52496 seconds directed at the north-west quadrant of the ring nebula S308 carried out during revolution 343 (unpublished). Skinner et al. (2002) investigated the possible existence of a close companion to WR 6. They make note of one other source in their FoV, 57.4" south of WR 6, which they fail to correlate with a SIMBAD counterpart. This source correlates with a star in our photometric PMS selection (field 1, star 73, see Table 3.6). Other than this they do not discuss the other sources in the FoV. The final EPIC source lists were retrieved from the ESA XMM-Newton Science Data Archive (<http://xmm.vilspa.esa.es/>) and filtered to remove sources with detection likelihood values of less than 20. This was to allow for an error in the calculation of detection likelihoods by the XMM-SAS pipeline, in versions 5.4.1 and earlier (see XMM-Newton news #29). The two source lists were then cross-correlated with one another to remove duplicates. In each case of a duplicate source the observation with best signal to noise was used. The source list was then further restricted to cover

just the region covered by the optical survey. A sample of the resulting source list, which contained 138 sources, is given as Table 3.3. The complete version is available via the CDS online database. Listed for each source are the XMM-Newton source number, right ascension, declination, error in position, count-rate and error in count-rate. For those X-ray sources that correlate with an optical counterpart (see section 4) the field number and star index are also listed.

It can be seen in Table 3.3 that occasionally the uncertainty in the Epic count rate is larger than the measured count rate. This does not indicate a non-detection, as source detection is not reliant on the count rate being larger than some multiple of the uncertainty. Instead source detection relies on the result of a likelihood determination, similar to that used for the ROSAT data.

Of the 39 ROSAT PSPC sources, 13 lay within the optical survey region and did not appear in the XMM-Newton source list. We will refer to this set of sources as the reduced ROSAT PSPC source list. This source list is given as Table 3.4. For each source we list and index number, right ascension, declination and the flux. Again, for those sources that correlate with an optical counterpart we also list the field number and star index.

Table 3.3: A sample of the XMM-Newton source list. The full version is available on-line from the CDS.

Index No.	$\alpha$ (J2000)	$\delta$ (J2000)	$\sigma_{pos}$ (arcsec)	Epic count rate( $s^{-1}$ )	$\sigma_{CR}$	Optical counterpart field no.	Star no.
1	06 54 13.040	-23 55 41.64	5.000	0.616	0.008	1.00	16
2	06 54 24.750	-23 50 31.56	5.000	0.034	0.005	1.00	10
4	06 54 28.460	-24 00 27.36	5.000	0.019	0.004	1.00	283
5	06 54 42.730	-24 07 14.18	5.000	0.048	0.015	8.00	20
6	06 54 17.530	-24 09 1.63	5.000	0.025	0.012	5.00	75
7	06 54 11.710	-23 56 39.57	5.000	0.011	0.005	1.00	73
8	06 53 48.930	-24 04 18.21	5.000	0.012	0.019	9.00	2086
9	06 53 13.220	-24 04 39.28	5.000	0.013	0.021	* **	****
10	06 54 55.290	-23 53 38.18	5.000	0.013	0.019	3.00	62

Table 3.4: The reduced ROSAT source list. X and Y are positions in the PSPC FoV.

Index No.	$\alpha$ (J2000)	$\delta$ (J2000)	X	Y	Raw Flux (counts)	Optical counterpart field no.	Star no.
1	06 53 1.200	-23 51 21.00	-0.270	0.070	73.169	2.00	2096
2	06 53 12.800	-23 53 53.00	-0.230	0.030	35.155	2.00	1070
3	06 53 13.200	-23 52 31.00	-0.220	0.050	36.431	2.00	143
5	06 53 19.600	-24 06 1.00	-0.200	-0.170	35.931	9.00	1029
8	06 53 28.800	-24 09 15.00	-0.160	-0.220	54.406	9.00	84
11	06 53 46.100	-24 07 17.00	-0.100	-0.190	39.062	9.00	23
15	06 53 52.900	-24 06 40.00	-0.070	-0.180	38.606	9.00	20
17	06 54 1.800	-24 11 42.00	-0.040	-0.270	48.397	5.00	3692
29	06 54 26.000	-23 43 49.00	0.050	0.200	28.123	4.00	216
33	06 54 38.300	-24 02 43.00	0.100	-0.120	19.837	8.00	343
35	06 54 43.200	-24 10 58.00	0.120	-0.250	34.905	8.00	26
36	06 54 49.100	-24 01 54.00	0.140	-0.100	23.722	8.00	116
39	06 55 12.400	-23 51 32.00	0.230	0.070	33.225	*.**	****

## 3.4 Identification of X-ray sources

### 3.4.1 Cross-correlation of optical and X-ray source lists

XMM-Newton source list and the reduced ROSAT PSPC source list were cross-correlated against the optical catalogue. XMM-Newton sources were matched using a search radius of 5 arcseconds, except in cases where the error in the position given in the EPIC source list was greater than this. In these cases the radius of the position error circle given in the XMM-Newton data was used. Since the accuracy of their positions was poorer, a search radius of 10 arcseconds was used to match the ROSAT sources. A bore-sight correction of +3 arcseconds in declination was applied to the ROSAT co-ordinates. This was based on the offset between the co-ordinates of the brightest X-ray source in the original ROSAT PSPC source list and the co-ordinates of WR 6 in the optical catalogue. Of the 151 X-ray sources in optical survey region (138 XMM-Newton sources and 13 ROSAT PSPC sources) 103 correlate with stars in the optical catalogue (91 XMM-Newton sources and 12 ROSAT PSPC sources). The positions in C-M space of the stars in the optical catalogue with X-ray correlations are shown in Figure 3.3. We have excluded stars with data quality flags other than “OO”, and those with signal-to-noise less than 10. It is clear from this plot that the majority of the correlated stars lie the region of the diagram occupied by the PMS. In fact, of the 68 sources plotted in Figure 3.3, 43 lie in the PMS region of the diagram. It is interesting to note that there is an apparent over-density of X-ray selected candidate PMS objects centered at the coordinates  $(V - I, V)$  1.1, 15. This corresponds roughly to where the PMS is expected to meet the galactic background main-sequence. This may indicate contamination of the sample by X-ray active main-sequence stars.

We estimated how many chance correlations we would expect to find in different regions of the CMD by performing the cross-correlation procedure for 8 different offsets of 30 arcseconds in each axis between the catalogues. We find that we would expect up to 5 of the correlations in the PMS region of the CMD to spurious, whilst essentially all of the correlations in the background region would be spurious.

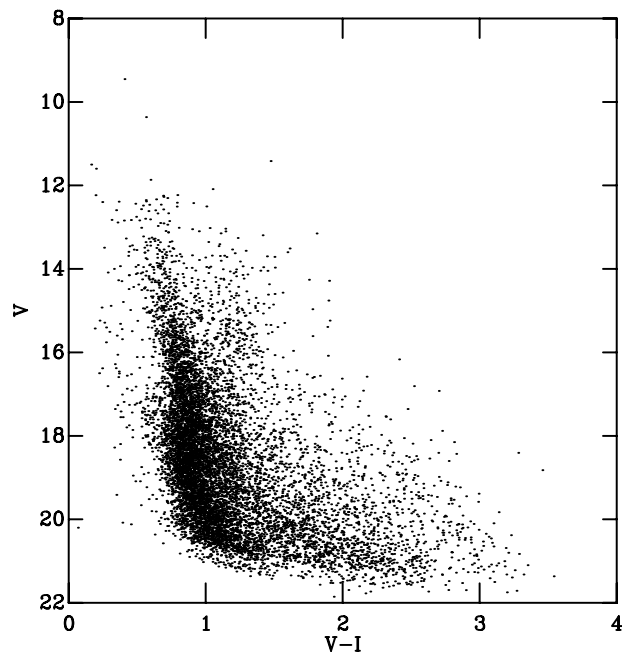


Figure 3.2: The CMD for the optical survey region for all unflagged objects with signal-to-noise  $> 10$  in V and V-I.

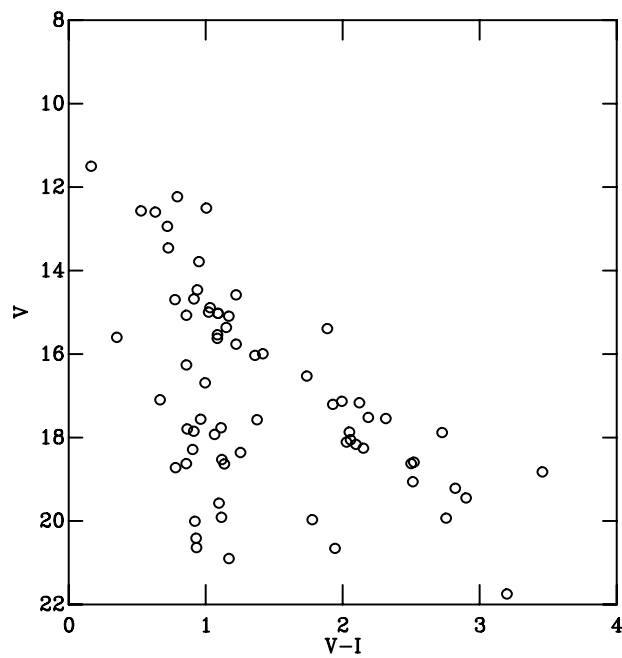


Figure 3.3: The CMD for X-ray correlated stars. Of the 103 stars correlated, 35 have been excluded from this plot due to low signal-to-noise (13) or for poor quality photometry (22).

### 3.4.2 Inferred X-ray Luminosities

It is important to verify that the observed count rates for the X-ray selected PMS candidates are consistent with what is expected for PMS stars. As mentioned in Chapter 1, the X-ray luminosities of low-mass PMS stars are expected to range from  $< 10^{28}$  to  $10^{31}$  erg s $^{-1}$  (Feigelson & Montmerle, 1999). Feigelson et al. (1993) used ROSAT observations to identify PMS stars in the Chameleon I dark cloud. They used a conversion factor of  $1 \text{ count ks}^{-1} = 3 \times 10^{28} \text{ erg s}^{-1}$  to obtain X-ray luminosities from ROSAT count rates. This assumed a distance of 140 pc to their targets. Since any low-mass PMS stars identified along this sight-line would be expected to be at a distance of roughly 600 pc or 1 kpc, this conversion factor becomes either: a)  $1 \text{ count ks}^{-1} = 5.4 \times 10^{29} \text{ erg s}^{-1}$ ; or b)  $1 \text{ count ks}^{-1} = 1.5 \times 10^{30} \text{ erg s}^{-1}$ . Inspection of Table 3.4 indicates that the raw fluxes for all the ROSAT X-ray sources lie approximately between 20 and 80 counts. Since the total effective exposure time was 25.8 ks, this corresponds to count rates ranging from 0.8 to 3.1 counts ks $^{-1}$ . As such, the inferred X-ray luminosities lie in the range  $4.3 \times 10^{29} \text{ erg s}^{-1}$  to  $1.7 \times 10^{30} \text{ erg s}^{-1}$  for a distance of 600 pc, or the range  $1.2 \times 10^{30} \text{ erg s}^{-1}$  to  $4.7 \times 10^{30} \text{ erg s}^{-1}$  for a distance of 1 kpc. In both cases inferred X-ray luminosities for these objects are consistent with their status as PMS stars.

### 3.4.3 Investigation of the proper motions of the X-ray selected PMS candidates

To remove objects that were not members of the group of interest, we refined our selection to remove objects that do not share common motion. We obtained SuperCosmos proper motions for 52 stars in our X-ray selected PMS (we did not exclude stars with poor photometry flags or low signal-to-noise for this experiment). A mean proper motion was calculated from the data, with each star being given a weight inversely proportional to the square of its error. Stars which contributed a  $\chi^2 > 4$  were removed from the selection and the weighted mean recalculated. This was repeated until no stars in the sample contributed a  $\chi^2$  above this value. In total 17 stars were removed from the sample, and these are marked on Figures 3.5 and 3.6 with faint circles. A value of  $\chi^2 > 4$  was chosen as the de-selection criterion since, for a sample of 52 stars, a  $2\sigma$  clip would be expected to remove 2 or 3 bona-fide members of the group. It is thought that all of the

stars removed from the sample were non-members. The distribution of the proper motions for the final selection are shown in Figure 3.4. The width of the distribution is consistent with the mean errors and an internal velocity dispersion which is close to zero. Those objects that were classified as PMS members of an association along this sight-line by both photometric and proper motion criteria are listed in Table 3.5. Those that were deselected based on their proper motions are listed in Table 3.6.

An interesting experiment would be to compare the proper motions of the confirmed members of this group of PMS stars with those measured by other surveys for stars along this sight-line. Unfortunately systematic error in the SuperCosmos proper motions is large at galactic latitudes  $|b| \leq 30^\circ$  (Hambly et al., 2001). As such, SuperCosmos proper motions for stars within our survey region with  $b \approx -10^\circ$  will have a large systematic error. This is both magnitude and survey plate dependant.

We have assessed this issue by calculating the weighted mean of the SuperCosmos proper motions for a broad selection of background field stars in our survey. The proper motion we find is  $(\mu_{\alpha\cos\delta}, \mu_\delta) = (2.43 \pm 0.26, -2.07 \pm 0.27)$  mas/yr. We calculate that the proper motion that would be expected due to galactic rotation and solar reflex for stars at 1 kpc distance in the direction of our survey should be approximately  $(\mu_{\alpha\cos\delta}, \mu_\delta) = (-2, 1)$  mas/yr. Since, for a random selection of field stars, one would expect the mean proper motion to coincide with the proper motion of the LSR and solar reflex, it is clear that whilst the SuperCosmos proper motions are sufficiently internally consistent for crude membership selection, they are not suitable for drawing comparisons with proper motions obtained from other surveys.

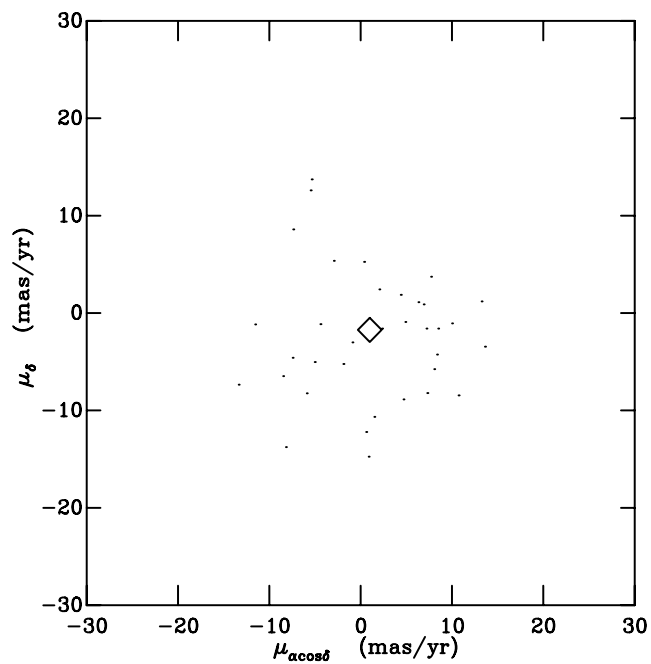


Figure 3.4: The proper motions for our X-ray selected PMS. Black dots show SuperCosmos proper motions for individual stars (Hambly et al., 2001), whilst the black error diamond indicates their weighted mean. The mean error in the SuperCosmos proper motions is 9.7 mas/yr in  $\mu_{\alpha \cos \delta}$  and 8.3 mas/yr in  $\mu_{\delta}$ .

Table 3.5: The Catalogue of X-ray selected PMS stars which were also proper motion members. Quality flags: 1<sup>st</sup> character is the quality flag for the star in the V band, the 2<sup>nd</sup> is for the I band. The meanings of the flags are: (O) O.K, (N) Non-stellar, (E) star too close to CCD Edge, (B) Background fit failed, (S) Saturated, (I) Ill determined sky, (V) Variable, (F) bad (Flagged) pixel, (M) negative (Minus) counts.

Field No.	Index No.	$\alpha$ (J2000)	$\delta$ (J2000)	X	Y	V	$\sigma_V$	Quality	V-I	$\sigma_{V-I}$	Quality
1.00	283	06 54 28.382	-24 00 28.33	523.465	1702.193	17.519	0.040	OO	2.187	0.040	OO
8.00	20	06 54 42.700	-24 07 14.57	1690.619	1010.048	13.786	0.006	OO	0.951	0.008	OO
3.00	62	06 54 55.245	-23 53 38.92	1278.492	679.337	14.680	0.006	OO	0.914	0.008	OO
8.00	114	06 54 49.326	-24 01 45.58	1465.167	190.009	17.544	0.010	OO	2.315	0.012	OO
1.00	241	06 54 23.176	-23 58 27.34	701.341	1400.640	15.763	0.018	OO	1.222	0.019	OO
1.00	217	06 53 44.112	-23 56 33.98	2036.446	1119.018	17.868	0.038	OO	2.049	0.038	OO
1.00	103	06 53 53.358	-24 02 6.55	1719.630	1947.546	14.996	0.003	OO	1.022	0.005	OO
1.00	142	06 54 17.023	-23 51 19.34	911.908	333.942	17.132	0.009	OO	1.994	0.012	OO
5.00	146	06 54 30.847	-24 03 21.67	416.553	414.314	15.993	0.006	OO	1.417	0.009	OO
1.00	270	06 54 4.895	-24 00 1.90	1325.816	1636.559	16.527	0.024	OO	1.738	0.025	OO
5.00	155	06 54 24.476	-24 03 46.10	634.082	475.192	17.206	0.008	OO	1.928	0.011	OO
5.00	175	06 54 28.227	-24 05 50.53	506.052	785.303	15.538	0.006	OO	1.086	0.009	OO
5.00	377	06 54 11.396	-24 04 35.61	1080.652	598.685	18.591	0.013	OO	2.520	0.015	OO
9.00	65	06 53 49.227	-24 05 44.12	243.212	786.842	15.093	0.004	OO	1.169	0.006	OO
1.00	669	06 54 23.934	-24 00 56.84	675.375	1773.234	18.256	0.008	OO	2.151	0.010	OO
2.00	610	06 53 23.910	-23 58 34.80	1051.277	1415.663	18.623	0.080	OO	2.500	0.090	OO
2.00	128	06 53 26.487	-23 51 38.56	963.496	378.178	17.167	0.033	OO	2.122	0.033	OO
8.00	59	06 54 53.249	-24 06 16.99	1330.721	866.268	15.025	0.006	OO	1.090	0.008	OO
1.00	711	06 54 30.531	-24 02 11.12	450.042	1958.374	19.059	0.012	OO	2.512	0.014	OO
1.00	421	06 54 20.499	-23 52 31.25	792.979	513.154	19.931	0.031	OO	2.755	0.033	OO
2.00	28	06 53 45.803	-24 00 4.24	303.310	1638.443	13.306	0.012	FO	0.711	0.016	FO
2.00	310	06 53 39.902	-23 49 58.21	504.650	127.940	19.901	0.249	IO	2.729	0.264	IO
6.00	26	06 55 5.986	-23 48 6.44	886.951	1570.648	12.598	0.008	OO	0.632	0.009	OO
1.00	243	06 54 32.055	-23 58 39.95	397.960	1432.076	15.624	0.017	OO	1.085	0.018	OO
2.00	123	06 53 14.140	-23 51 12.99	1385.775	314.702	18.053	0.054	OO	2.057	0.055	OO
1.00	50	06 54 4.958	-23 51 58.68	1324.456	432.186	14.461	0.013	OO	0.939	0.014	OO
2.00	126	06 52 59.607	-23 51 31.79	1882.788	362.056	17.881	0.048	OO	2.726	0.048	OO
1.00	62	06 53 58.401	-23 53 50.12	1548.458	710.112	14.581	0.013	OO	1.222	0.015	OO
4.00	367	06 54 1.454	-23 38 28.39	1416.782	120.055	18.109	0.018	OO	2.028	0.020	OO
4.00	18	06 53 59.247	-23 42 24.56	1491.916	708.767	10.623	0.011	IN	0.015	0.015	IN
4.00	343	06 54 26.122	-23 37 49.12	571.728	21.888	19.264	0.142	OO	2.538	0.142	OO
4.00	380	06 54 14.114	-23 38 48.92	983.074	171.002	19.447	0.023	OO	2.901	0.025	OO
9.00	84	06 53 28.076	-24 09 18.79	965.046	1321.824	14.888	0.006	OO	1.032	0.008	OO
8.00	26	06 54 43.492	-24 11 0.44	1663.026	1572.877	11.588	0.011	NN	0.138	0.016	NN
8.00	116	06 54 49.690	-24 01 54.07	1452.693	211.155	16.031	0.007	OO	1.360	0.008	OO

Table 3.6: The Catalogue of X-ray selected PMS stars which were not proper motion members. Quality flags: 1<sup>st</sup> character is the quality flag for the star in the V band, the 2<sup>nd</sup> is for the I band. The meanings of the flags are: (O) O.K, (N) Non-stellar, (E) star too close to CCD Edge, (B) Background fit failed, (S) Saturated, (I) Ill determined sky, (V) Variable, (F) bad (Flagged) pixel, (M) negative (Minus) counts.

Field No.	Index No.	$\alpha$ (J2000)	$\delta$ (J2000)	X	Y	V	$\sigma_V$	Quality	V-I	$\sigma_{V-I}$	Quality
1.00	10	06 54 24.926	-23 50 32.22	641.610	216.465	12.291	0.011	NN	0.974	0.016	NN
5.00	75	06 54 17.359	-24 09 2.91	876.917	1264.800	13.457	0.006	OO	0.727	0.008	OO
1.00	73	06 54 11.668	-23 56 39.46	1094.679	1131.870	15.363	0.006	OO	1.150	0.009	OO
1.00	54	06 54 38.612	-23 52 46.11	173.600	550.238	14.697	0.005	OO	0.776	0.006	OO
4.00	32	06 54 25.237	-23 48 13.95	602.029	1579.247	10.399	0.011	II	0.530	0.015	II
9.00	10	06 53 47.900	-24 04 14.41	288.466	563.284	12.941	0.008	OO	0.720	0.011	OO
1.00	527	06 54 34.361	-23 56 31.49	319.100	1111.931	19.216	0.019	OO	2.822	0.021	OO
5.00	474	06 54 15.829	-24 07 41.69	929.199	1062.385	19.367	0.145	OO	2.456	0.158	OO
1.00	198	06 54 2.020	-23 55 24.62	1424.525	945.530	18.823	0.014	OO	3.458	0.016	OO
8.00	825	06 54 35.539	-24 01 26.02	1936.076	141.717	21.748	0.087	OO	3.199	0.089	OO
8.00	45	06 55 1.219	-24 03 24.50	1058.879	436.294	15.070	0.006	OO	0.859	0.009	OO
4.00	25	06 53 47.103	-23 44 23.71	1907.386	1006.131	12.502	0.011	OO	1.005	0.016	OO
2.00	51	06 53 1.832	-23 51 36.62	1806.706	373.990	15.391	0.016	OO	1.888	0.017	OO
4.00	28	06 54 1.644	-23 46 13.73	1409.453	1279.888	11.039	0.011	II	1.214	0.015	II
4.00	29	06 53 48.959	-23 46 15.28	1843.567	1284.157	12.570	0.011	OO	0.528	0.013	OO
9.00	23	06 53 46.731	-24 07 19.32	328.471	1024.081	12.231	0.005	OO	0.793	0.007	OO
5.00	3692	06 54 2.434	-24 11 47.66	1385.935	1675.635	20.010	0.275	NI	4.027	0.278	NI
4.00	216	06 54 26.372	-23 43 44.89	563.172	908.619	18.164	0.011	OO	2.097	0.014	OO

### 3.5 Discussion: how far away and how old are the PMS stars?

The fitting of theoretical isochrones to the observed PMS can yield distances and ages for stars found there. However there is a degeneracy between distance and age for low-mass stars. As such any estimates of distance and age must be made within the context of the estimates of the distances to the higher mass stars, as well as the constraints that higher mass stars place on the age of any associations that may be present.

Isochrones in  $V/V - I$  were generated from the solar metallicity models of D'Antona & Mazzitelli (1997) in the same manner as described by Jeffries et al. (2001). Empirical colour- $T_{eff}$  conversions were obtained by fitting a 120 Myr isochrone to the Pleiades at a distance modulus of 5.6,  $E(B - V)=0.04$ ,  $E(V - I_c)=0.05$ .

We scaled the resultant isochrones for a distance of 600 pc, in keeping with the distance derived for Cr 121 by de Zeeuw et al. (1999) of  $592 \pm 28$  pc. In addition to shifting the isochrones for distance, they were also shifted for an extinction of  $A_V = 0.17$  (Kaltcheva, 2000). This corresponds to a reddening of  $E(V - I) = 0.07$  (if we assume a galactic reddening law), though this has little effect on the results as the reddening vector lies along the isochrones. If the low-mass PMS stars are located within the association at the distance found from the Hipparcos data, the best fitting isochrones are those corresponding to ages between 20 and 50 Myrs (see Figure 3.5). These imply a median age of 30 Myrs, with an age spread of about 30 Myrs. Such an age spread is not considered likely for an association of this age (Jeffries & Tolley, 1998, and references therein). Additionally, as was noted by de Zeeuw et al. (1999), the presence of an O-star and early B-stars indicates that this moving group is young, about 5 Myrs old. For such a large number of PMS stars to be found within such a small survey region would also be surprising if they were associated with the group described by de Zeeuw et al. (1999). Assuming a Salpeter initial mass function (IMF), we calculate that we would expect to find 3900  $0.20-0.73 M_{\odot}$  ( $14 \leq V \leq 20$  at 592 pc) stars for the 85 B stars selected as members by de Zeeuw et al. (1999). If we assume that these would be distributed evenly over a region at least as large as the  $13^{\circ} \times 16^{\circ}$  region occupied by the B stars, then we would expect to find fewer than five  $0.20-0.73 M_{\odot}$  stars within the region observed here. As such, the PMS found here would represent quite a concentration of the low-mass stars of the association. It

should be noted that a more realistic IMF would predict even fewer stars in this mass range, since several observational studies have found that the IMF in young clusters flattens out at masses below  $\sim 0.8 M_{\odot}$  (e.g. Preibisch et al., 2002; Briceño et al., 2002, and references therein).

The three lines of argument described above lead us to reject the scenario in which the low-mass PMS stars are associated with the moving group detected using the Hipparcos data. Instead, we use the presence of early-type main sequence B-stars in the membership lists for both interpretations of Cr 121 to constrain the age to less than 15 Myrs. Such a young age is also more in keeping the scatter of stars in the PMS region of the diagram. Scaling sets of isochrones for ages of less than 15 Myrs for distance until they fitted as much of the data as possible gave a distance of 1050 pc, and a modal age of between 1 and 10 Myrs, applying the same extinction as before. This is consistent with the distance given by Kaltcheva (2000) for a compact group of stars at  $1085 \pm 41$  pc. Figure 3.6 shows that the age spread implied by fitting isochrones for this distance is less than 10 Myrs, much more in keeping with age spreads observed in other young clusters and associations (e.g. Pozzo et al., 2003), than the 30 Myr age spread suggested by the fit for 600 pc. Isochrones for 1 and 20 Myr, scaled for the same distance as the 5 and 10 Myr ones, are included in Figure 3.6 for comparison.

If we carry out a similar calculation to the one above, using a Salpeter IMF, we find that we would expect there to be around 540 stars in the  $0.29\text{-}0.98 M_{\odot}$  mass range ( $14 \leq V \leq 20$  at 1050 pc) for the 11 B-type members of the more distant cluster suggested by Kaltcheva (2000). If we assume an even distribution of stars over the  $\approx 1^{\circ}$  radius surveyed there, then we would expect to find, at most, 130 stars in this mass range in the region covered by our optical survey. This is consistent with the population of the PMS observed here. This would indicate that the PMS we have identified consists of stars in the  $\approx 1$  kpc distant cluster identified by Collinder (1931); Eggen (1981) and Kaltcheva (2000). To avoid confusion we shall refer to this distant cluster as Cr 121, and we shall refer to the association at approximately 600 pc as CMa OB2, following Eggen (1981).

As can be seen in Figure 3.6, several of the candidate PMS objects that were rejected on the basis of their proper motions lie about a magnitude above the isochrones fitted for Cr 121. It is possible that these objects may in fact be foreground members of CMa OB2.

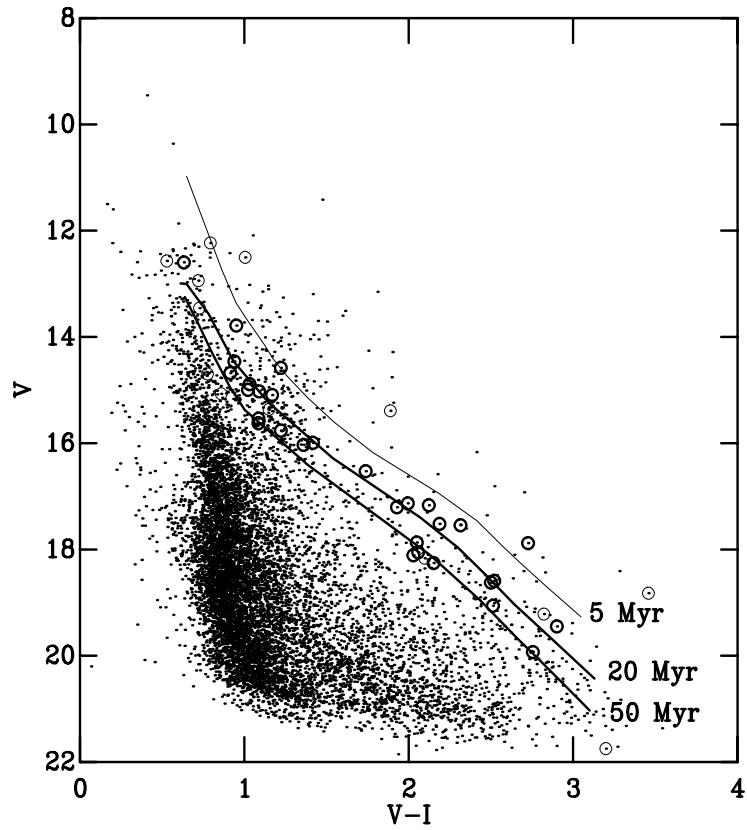


Figure 3.5: The CMD for the fields centred on WR 6 with 5, 20, and 50 Myr isochrones overlaid for (intrinsic)  $dM=8.9$  and  $A_V=0.17$ . Circled points indicate X-ray correlated stars. Points marked with faint circles are those cut from the sample in section 4.2.

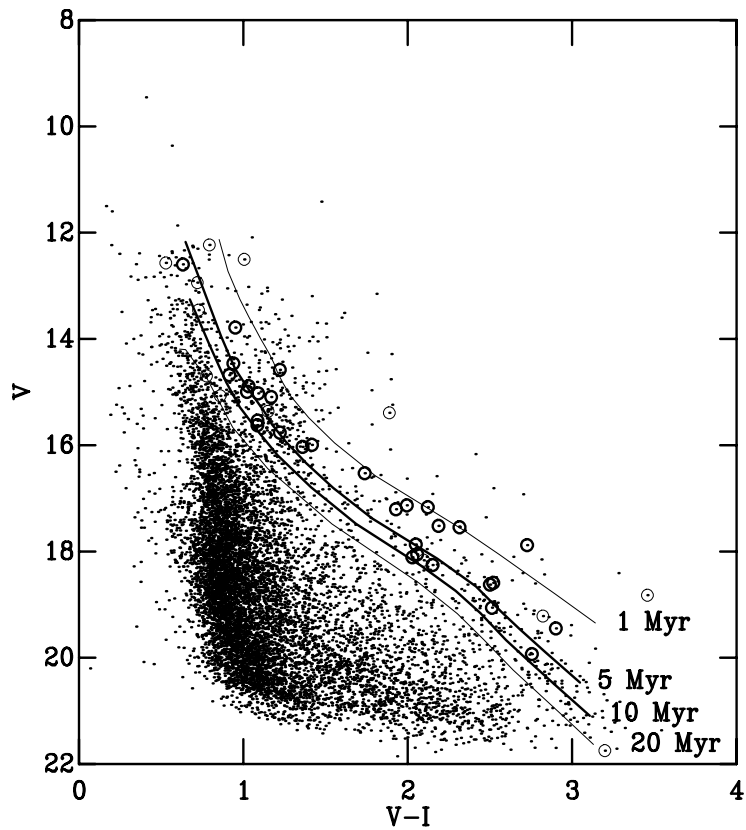


Figure 3.6: The CMD for the fields centred on WR 6 with 1, 5, 10 and 20 Myr isochrones fitted for (intrinsic)  $dM=10.1$  and  $A_V=0.17$ . Circled points indicate X-ray correlated stars. Points marked with faint circles are those cut from the sample in section 4.2.

### 3.6 Conclusions

It seems clear that the low-mass PMS stars detected here are associated with the compact group of stars found by Kaltcheva (2000); Eggen (1981) and Collinder (1931) at a distance of over 1 kpc, originally designated Cr 121. If this cluster were of the extent and at the distance found by de Zeeuw et al. (1999), the discovery of such a concentration of low-mass PMS stars which are so much older than the rest of the association, and with an age spread of 30 Myrs, seems incredible. It is also clear however, that there is a young moving group that was detected using the Hipparcos data by de Zeeuw et al. (1999) at a distance of  $592 \pm 28$  pc, of which WR 6 is likely a member, in the same direction. The characteristics of the group described there, however, seem more in keeping with an OB association, than with the compact open cluster originally described as Cr 121. We argue that the distant open cluster should retain its original designation as Collinder 121, whilst the nearer OB association described by Feinstein (1967); de Zeeuw et al. (1999); Dias et al. (2002) should be re-designated as CMa OB2, following Eggen (1981).

Whilst the Hipparcos census of OB associations within 1 kpc is an invaluable resource for studying recent local star formation, this work demonstrates the importance of interpreting proper-motion and parallax data within the context of age and distance constraints imposed by main-sequence high mass and low-mass PMS stars. This is particularly true when investigating structures that extend beyond the range of the Hipparcos data.

This work has demonstrated how the consideration of the C-M distribution of a PMS population can provide insights into the structural nature of the group of which they are members. Studies of the type described here are limited however, as the PMS selection is biased towards only selecting X-ray bright objects. As such, some method of making an unbiased selection of PMS objects on the CMD is required if other properties of the group such as its mass function, or apparent age spread, are to be studied. It is just this subject that will be explored in the next chapter.

## 4 Contamination and exclusion in the $\sigma$ Orionis young group.

### 4.1 Introduction

In this chapter the issues of contamination by non-members, and exclusion of bona-fide members from photometric PMS selections will be explored. The selection of candidate members of OB associations and young clusters by location on a CMD is an extremely cost effective way of identifying PMS stars. Clearly it is not possible to be confident of an individual object's PMS status based purely on its location in colour-magnitude (C-M) space. However, where statistical studies of PMS populations are concerned photometric selection has the potential to prove extremely useful. Before such a selection technique may be used with confidence, an estimate of the level of contamination by non-members must be obtained. It must also be determined if appreciable numbers of bona-fide members lie beyond the proposed selection area on the CMD. Such a selection technique would be of particular use for studies of the low-mass end of the initial mass function (IMF). The following work has been published in a MNRAS paper (Burningham et al., 2005b).

Studies of the low-mass and sub-stellar IMF provide the opportunity to constrain theories of star formation and investigate environmental influences on the final results of the formation process. Whilst the high and intermediate mass regions of the IMF have been well studied and found to be essentially universal in the field and in clusters (e.g. Hillenbrand, 2003; Garmany et al., 1982, and references therein), this is not the case for low and sub-stellar masses. Although there have been a number of studies of the low-mass IMF in the field (e.g. Reid et al., 1999; Kroupa, 2001), due to their inherent faintness only the most nearby of field T dwarfs are detected, leading to poor statistics at these masses. Searches for brown dwarfs in intermediate age ( $10^8$  yrs) clusters such as the Pleiades have proved fruitful (e.g. Moraux et al., 2003; Basri, 2000, and references therein). Unfortunately, to derive an IMF from the mass function of an intermediate age cluster requires corrections for the effects of stellar and dynamical evolution over the age of the cluster.

Young clusters and associations are the ideal places to study this region of the IMF. This is because many of the problems associated with measuring the IMF at the lowest masses disappear in such young regions. Firstly no correction need be made for the effects of stellar or dynamical

evolution, the regions are sufficiently young that the measured mass function *is* the IMF. Also, the objects at sub-stellar masses are much easier to observe at ages of less than 10 Myrs since they still shine brightly as gravitational potential is released. In addition, a supposed advantage of clusters and associations with ages of less than 2 Myrs is the lack of contaminating sources due to the fact that such young clusters are often still associated with their natal molecular cloud, which will tend to obscure the background to high extinctions. The Orion Nebula Cluster (ONC) has been extensively studied for just these reasons (e.g. Muench et al., 2002; Luhman et al., 2000; Lucas & Roche, 2000). However, inspection of the methods which must be employed for such studies reveals that association with a molecular cloud brings with it its own, unavoidable, problems.

Since there is often a spread of ages in young star forming regions, it is preferable to use photometric magnitudes and spectroscopically derived temperatures in conjunction with PMS models to determine the age and mass for each object in the sample. Unfortunately due to the high extinctions present along sight-lines toward young, partially embedded, clusters it is generally not possible to obtain spectroscopy for the lowest mass objects. Since there is also normally a large range of reddening toward objects within such clusters it is not possible to determine the age and mass for each object, and a distribution of ages and reddening must be assumed to obtain the IMF from the luminosity function (LF) (Muench et al., 2002). Another effect of the high extinction is that LFs must be constructed in the K- and L-band to avoid biasing the sample to the least extinguished objects and to ensure a good level of completeness. However, it has been observed in the young clusters such as the ONC that up to 85% of the objects have circumstellar discs, which are responsible for infra-red excesses (e.g. Lada et al., 2000), making mass functions derived from K- and L-band LFs unreliable. These problems are avoided if star forming regions between 2 and 10 Myrs old are used for IMF studies. At these ages the clusters have often emerged fully from their natal cloud, presumably due to the UV flux from the massive stars evaporating the molecular gas. The lower extinction allows the luminosity function to be constructed in the I-band, which is less affected by circumstellar discs than the K-band, in addition to making spectroscopy possible down to very low masses. Since we need such regions to be as nearby as possible, to allow studies of the lowest mass objects, the number of prospective laboratories is very small. The most promising candidate is the  $\sigma$  Orionis ( $\sigma$  Ori) young group, a constituent of the Orion OB1b association, which has age estimates in the range 1.7 - 5 Myrs (Warren & Hesser, 1978; Brown et al., 1994). The low

extinction,  $E(B - V) = 0.05$  (Lee, 1968), and small distance,  $D \approx 350$  pc (Perryman et al., 1997), make it ideal for studies of the low mass IMF.

Béjar et al. (2001) have carried out an investigation of the sub-stellar IMF in the  $\sigma$  Ori region. They used a sample of 9 spectroscopically confirmed members to define the locus of the cluster sequence between M6 and L4 spectral types. They then used the location of this sequence in C-M space to identify cluster members, and construct an I-band LF. Using several different models to construct their IMF, Béjar et al. (2001) found a mass spectrum  $(dN/dm) \propto m^{-\alpha}$  with an exponent of  $\alpha = 0.8 \pm 0.4$  between  $0.2$  and  $0.01M_{\odot}$ , i.e. the number of objects per mass bin continues to increase with decreasing mass down to below the deuterium burning limit and into the realm of planetary mass objects. This corresponds to an IMF  $\xi(m) \propto M^{-\gamma}$  with an exponent  $\gamma = -0.2$ . The low extinction, however, means that background contamination cannot be ruled out, even in the locus of the cluster sequence. Barrado y Navascués et al. (2001) obtained spectral types for roughly one quarter of the photometrically selected candidates, confirming a high proportion of them as cool objects. Whilst such a method is effective at removing reddened background objects from a sample, it is not robust against interloping field dwarfs.

When the number of objects in each mass bin is so small, however, a small number of contaminants can have a significant effect on the derived mass function. Whilst Béjar et al. (2001) are careful with their photometric selection to avoid contamination, this could, in itself, lead to poorly understood completeness. Without empirically determining how far into the expected background region of the CMD bona fide members are still found, any photometric selection which minimises contamination may well exclude a significant fraction of member objects.

The likelihood of age spread in such a young cluster makes this consideration crucial. Kenyon et al. (2005) obtained fibre spectroscopy for a sample of over 70 candidate members, drawn from a *RI* catalogue, with masses between  $0.055$  and  $0.3M_{\odot}$  (they assume a cluster age of 5 Myrs). They found that contamination from background objects was limited for the reddest region of each magnitude bin in the I/R-I CMD, but the PMS objects were poorly correlated with isochrones in this colour. They found better correlation in I/I-J, the colours used by Béjar et al. (2001), but the contamination was found to be considerably worse, becoming more prevalent at the faintest magnitudes. Additionally, the CMDs of Kenyon et al. (2005) show that any strict cut along isochrones in either set of colours would exclude a significant number of members.

It is clear that the only way to obtain a reliable IMF for this region is to use a spectroscopically confirmed sample of members, drawn from a broad region of colour magnitude space. Kenyon et al. (2005) used the presence of Li I absorption at 6708 Å to confirm youth and thus membership for objects in their sample. This technique, however, is limited to objects with  $M \geq 0.06M_{\odot}$ . Objects below this mass never attain high enough temperatures in their cores to burn lithium (Chabrier & Baraffe, 1997). Old foreground T-dwarfs, therefore, cannot be distinguished from bona fide members based on Li absorption alone.

If a reliable IMF is to be derived for the lowest masses, another method of distinguishing members must be found. It is with this in mind that we have obtained fibre spectroscopy of the Na I doublet at 8183, 8195 Å for a photometrically selected sample of objects in the direction of the  $\sigma$  Ori cluster. Using this doublet has several benefits. Cool objects such as low-mass stars and brown dwarfs are brightest in the NIR and IR regions, where night sky emission can severely affect observations. The Na I doublet lies at a wavelength which is relatively unaffected by bright sky emission lines. Also the Na I doublet is a relatively strong spectral feature in cool stars, and so should be easy to observe at moderate S/N.

In this chapter we have two aims. Firstly, to measure the level of contamination from non-members in the expected PMS region of the CMD and to determine if many bona fide members are excluded by photometric selection techniques. Our second aim is to investigate the use of radial velocity, as measured from the Na I doublet, as a membership diagnostic. Whilst Li absorption would be an effective diagnostic for much of our sample, this work is concerned with developing a spectroscopic technique for use at magnitudes and colours where foreground contaminants may lie below the Li burning limit.

The rest of the chapter will be laid out as follows. In Section 4.2 we will discuss the rationale behind our target selection and our observations. In Section 4.3 we will describe our data reduction technique and our method for sky subtraction. In Section 4.4 we will describe our sample selection, the cross correlation of spectra to obtain radial velocities and the calculation of membership probabilities. Section 4.5 will contain a discussion of the results. A summary of our conclusions will be given in Section 4.6.

## 4.2 Optical spectroscopy using AF2/WYFFOS

### 4.2.1 Target selection

We obtained spectra for 117 objects using the AF2/WYFFOS fibre spectrograph on the William Herschel Telescope at the Observatorio del Roque de Los Muchachos, La Palma. The targets were selected from the photometric *RI* catalogue described by Kenyon et al. (2005) and were chosen to compliment the sample for which spectroscopic observations have already been obtained (Kenyon et al., 2005). Since many of the reddest objects have already been observed, particularly at the brighter magnitudes, we were able to cut deep into the region which is thought to be background contamination, see Figure 4.1. This method of target selection has served a dual purpose: 1) it allows us to investigate the possibility of contamination in the PMS region of colour magnitude space; 2) it allows us to investigate the number of member objects which might be lost in more conservatively drawn samples. The distribution of the targets, in relation to  $\sigma$  Ori, and the WYFFOS/WHT FoV is shown in Figure 4.2. The fibre configuration files for use with AF2/WYFFOS were compiled by Dr. Stuart Littlefair.

### 4.2.2 Observations

We observed our targets using the small fibre (1.6", 159 fibres) setup on the nights of the 3<sup>rd</sup> and 4<sup>th</sup> January 2003. Observations on the first of these nights were carried out by Dr. Stuart Littlefair and Prof. Tim Naylor. The observations on the second night were carried out by the author and Prof. Tim Naylor. Conditions were dark, and cloud was only present during the first half of the second night. We observed in 3rd order echelle mode, with a central wavelength of 8300 Å. This gives a dispersion of 0.57 Å/pixel and we achieved a resolution of approximately 1.4 Å. We elected to observe the Na I doublet at high resolution so as to avoid broadening the bright sky emission lines and obscuring the doublet.

We achieved a total exposure time of 9.5 hours for the faintest targets. This time was split between 4 configurations to maximise the number of objects we could observe (see Table 4.1). The brightest targets were only observed in the shortest set-ups, with fainter ones observed using a combination of set-ups to achieve appropriate integration times. Each set of exposures was subdivided

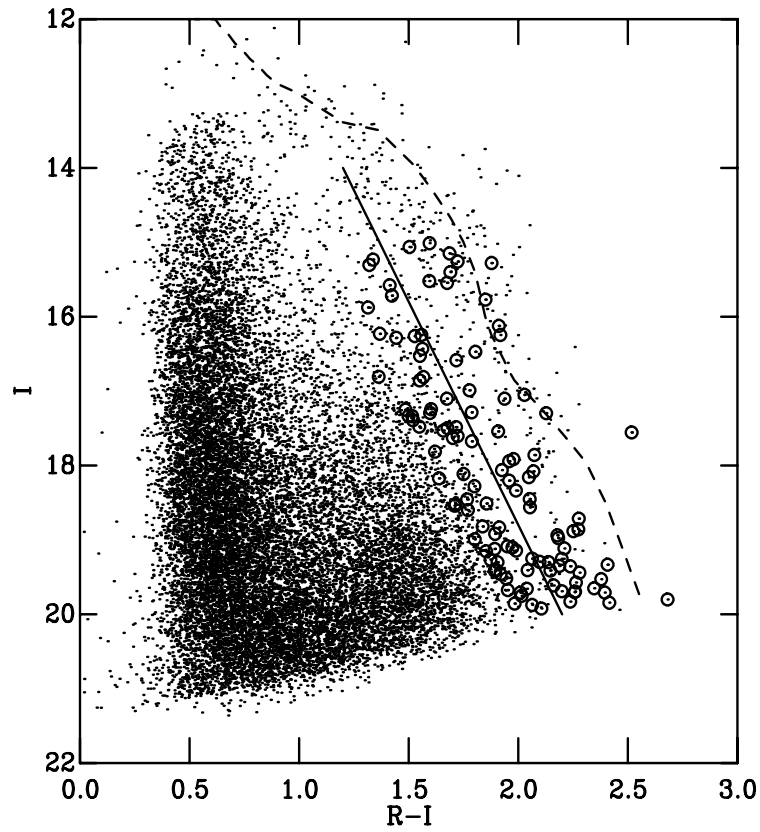


Figure 4.1: The CMD for the optical  $RI$  catalogue from which targets were selected (Kenyon et al., 2005). Targets for this survey are shown as circles. The dotted line follows a NextGen 5 Myr isochrone (Chabrier & Baraffe, 1997; Baraffe et al., 2002). We define the expected background region to be blueward of the solid line, and the PMS region to be redward of it (see section 5).

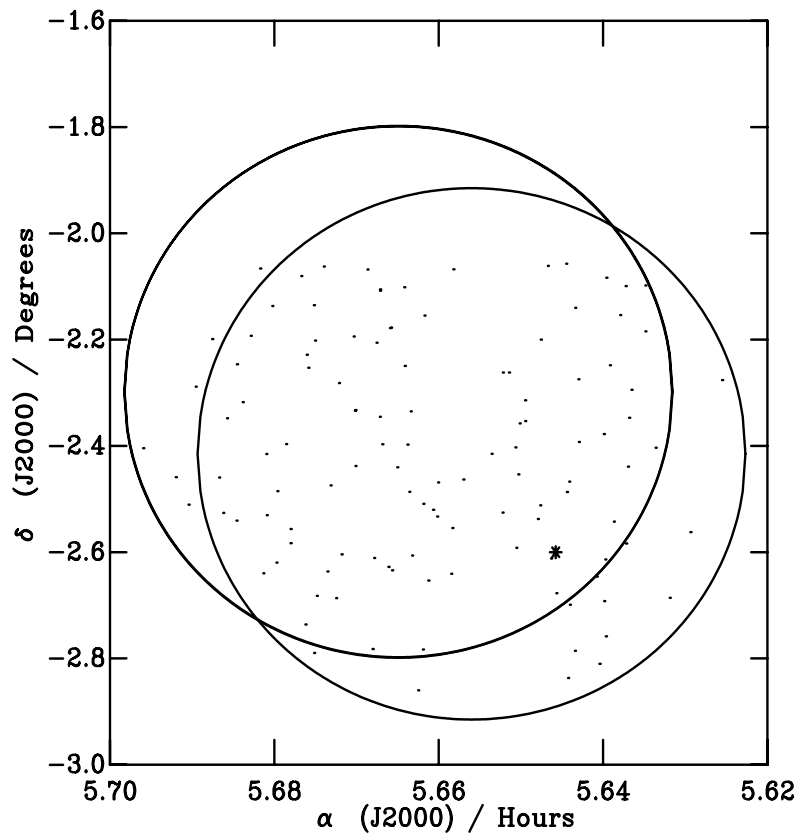


Figure 4.2: The locations of our targets and WHT FoVs.  $\sigma$  Ori is shown as an asterisk, whilst our targets are shown as dots. The WHT FoVs are shown as large circles.

into Sections of 900s or 1800s, depending on the total exposure required for the set-up. Between exposures of the target objects, the telescope was moved such that  $\sigma$  Ori lay over a fibre, and a spectrum of  $\sigma$  Ori was obtained for the purposes of telluric correction. Copper-Neon arc frames were also obtained for both positions of the telescope at these times. To maximise our exposure times we did not observe offset sky fields, as is advised by Wyse & Gilmore (1992), for estimating the relative throughput of the fibres prior to sky subtraction. However, the relative throughput of the fibres in the small fibre bundle is considerably more homogeneous than it had been for the older large fibre bundle (see <http://www.ing.iac.es/Astronomy/instruments/af2/index.html>), and we have an alternative method for achieving sky subtraction, which will be described later. We also observed several stars for use as radial velocity standards, these observations are detailed in Table 4.2, along with the identifier of the telluric reference observed.

Unfortunately, many of the spectra we obtained suffered from poor signal-to-noise, and others had no detectable signal at all. We have correlated the *RI* photometric catalogue used to select our targets with a 2MASS catalogue for the same region and find the RMS in the residuals of the coordinates to be approximately  $0.2''$  in both axes. As such, we rule out errors in the astrometry of the *RI* catalogue as an explanation for our missed targets. We also rule out proper motion as a factor. At the target selection stage the 2MASS catalogue for our potential targets was correlated against the SuperCosmos sky survey catalogue for the same region and objects with large coordinate residuals were excluded. Whilst source variability, well known in T Tauri stars, may have had an influence on the signal detected from some of the targets, we believe the failure to achieve the desired signal-to-noise in so many spectra is the result of two problems with the AF2/WYFFOS field of view (FoV). Firstly, the point spread function (PSF) is highly variable across the FoV, becoming very smeared out beyond a radius of 25 arcminutes. As such, when using the small fibre bundle a large proportion of the signal from a target star in the outer area of the FoV will be lost. This effect explains the poor signal-to-noise found in the spectra of some objects. The second problem is that the astrometric distortion in the AF2/WYFFOS FoV is poorly constrained, meaning that many objects were simply missed by their assigned fibre. The method employed for selecting our sample from the available spectra is discussed in Section 4.4.1.

Table 4.1: Summary of the exposure times and sky fibre allocations for the 4 configurations used.

Configuration	Integration Time (s)	No. of Sky Fibres
Long1	12600	58
Long2	12600	49
Medium	5400	35
Short	3600	29

## 4.3 Data reduction

### 4.3.1 Extraction of spectra

The spectra were extracted and dispersion corrected using the WYFFOS data reduction routines within the RGO package in the IRAF environment (Lewis, 1996). The spectra were bias subtracted using the mean bias level in the overscan region of the Tek6 detector. Flatfielding was achieved using tungsten flatfields, which were also used for aperture detection. Although flatfielding is best achieved by dividing the whole CCD for a target frame by a normalised flatfield frame prior to extraction, this was not possible. Due to the nature of the instrument, there was no way of evenly illuminating the chip to obtain a suitable flatfield. Instead, flatfielding was carried out after extraction by dividing each target spectrum by the same spectrum extracted from the flatfield frame. Such a method is acceptable so long as the form of the spectrum's profile in the spatial direction is roughly the same in both frames.

The tungsten flatfields were also used to identify the location of the spectrum from each fibre on the chip. The aperture detection algorithm determined over how many pixels each spectrum was spread, and traced the shape of the spectrum on the chip, since this was not generally a straight line. The flatfield spectra were traced using steps of 5 pixels and fitted using a 2<sup>rd</sup> order spline function. The reduction software would then assign an aperture number to each spectrum. This could then be used by the software to identify which fibre a spectrum had come from by comparison to a reference table of aperture numbers, and thus obtain information regarding the target. Unfortunately, such a table was not available for the small fibre set-up. As such, information

regarding the target of a fibre was not reunited with its spectrum until later in the process. The aperture detection process was interactive and allowed the user to reject false detections and mark spectra that had been missed.

Spectra were then optimally extracted from target,  $\sigma$  Ori and arc frames. The optimal extraction of spectra is analogous to the optical extraction of photometry. Pixels in the spatial direction are summed according to weights that reflect their S/N. Thus, pixels on the edge of the spectrum in the spatial direction, where the signal is of the same order as the readout noise of the chip have lower weights. This reduces the contribution of readout noise to the final extracted spectrum significantly. Since the spaces between the spectra on the chip are small in the small fibre set-up it was not possible to construct a good model of scattered light incident on the detector. For this reason scattered light correction was neglected in this reduction.

Dispersion correction was achieved by first fitting a 4<sup>th</sup> order Chebyshev function to the wavelength vs. pixel relationship obtained by manually identifying spectral lines in the middle aperture of the appropriate arc frame. An automated procedure then obtained solutions using the same lines in the remaining apertures. The RMS deviation about the dispersion solution across the apertures in the arc frames was typically 0.01-0.02 Å. These solutions were then applied to spectra from the same apertures in the target frame.

The final stage of the initial reduction and extraction procedure was to reunite the spectra with the information regarding their target. As mentioned previously, the standard method provided by the reduction software was not available since no aperture reference table had yet been constructed for the small fibre set-up. Instead a table was constructed, using the flatfield frames as a reference, which related the central pixel number of a spectrum to its fibre number. This was made possible by the fact that parked fibres resulted in distinct dark columns on the chip, and thus provided reference points to prevent mix ups. By inspecting flatfields associated with several different set-ups, where there were different parked fibres, a reliable reference table was arrived at. The output format of the reduction software associated each spectrum with the range of pixels it covered at a point halfway along its length, and this allowed the spectra to be finally associated with their fibres.

### 4.3.2 Telluric correction and sky subtraction

Absorption features due the Earth’s atmosphere can influence the results of cross-correlation, by biasing the result towards zero velocity. As such the effects of the atmospheric, or telluric, absorption must be corrected for. It is normal for an O-star, whose spectrum should be nearly featureless, to be used to as a reference spectrum for telluric correction. This can lead to difficulty when the reference star is well separated from the targets, as one is required to assume that the telluric absorption is uniform in both time and position. Fortunately,  $\sigma$  Ori itself provides us with an appropriate reference spectrum, and is located within our FoVs. As such, we need only assume that the telluric absorption is uniform over short periods of time.

Telluric correction was carried out on spectra from each sub-exposure using the temporally closest  $\sigma$  Ori spectrum. Radial velocity standard spectra were corrected using a telluric reference observed immediately before or after each exposure, and chosen to be close-by on the sky, and these are listed in Table 4.2. In each case the object spectrum was divided by a rectified version of the telluric reference spectrum, thus removing absorption features originating in the Earth’s atmosphere.

The object spectra from the sub-exposures of each configuration were combined by median stacking prior to sky subtraction. We calculated the uncertainties in flux at this point as the standard error about the median. Two master sky spectra were constructed for each configuration by calculating (i) the weighted mean and (ii) the median of median stacked spectra from each sub-exposure. The sky spectra used for constructing the median sky for each sub-exposure were selected on the basis of being free of cosmic rays in the region of interest ( $8100 \text{ \AA} \leq \lambda \leq 8300 \text{ \AA}$ ). Since our target region is well separated from the nebular emission near the Horsehead, the background is flat. As such, use of a master sky spectrum for each set-up is appropriate (see below also).

Since no offset sky frames were obtained, it was not possible to estimate the relative throughput of each fibre and use this to scale the master sky spectrum to each fibre for subtraction. Instead we have iteratively scaled the master sky frame until the subtraction is optimised for the removal of sky lines. The method we use is identical to that used by Beekman et al. (2000) for removing the, relatively sharp-spiked, secondary star spectrum from that of a cataclysmic variable (CV). In this case the master sky frame is treated as a template secondary star spectrum, and the tar-

get+sky as the CV spectrum. First we subtract the master sky frame with no scaling and smooth the residual with a smoothing length of 50 pixels. The smoothed residual is then subtracted from the unsmoothed residual and the  $\chi^2$  per pixel calculated. This procedure is then repeated with a series of different scale factors. The scale factor that results in the lowest value of  $\chi^2$  is the one which is then applied to master sky spectrum prior to subtraction from the data. An example of the success of this method of sky subtraction is shown in Figure 4.3. This method was carried out using both versions of the master sky frames. As can be seen in Figure 4.3, sky emission lines lie at similar wavelengths to the Na I doublet of interest. As such it is crucial that the sky lines are not over-subtracted, giving rise to spurious absorption features. To assess the effectiveness of each sky subtraction we used the two emission lines just blueward of 8150 Å as diagnostic lines. Since these lines were found to be more intense than those situated over Na I doublet in the spectra from all sky fibres, they are good indicators of over-subtraction. A problem would arise if the relative strengths of these lines varied significantly across the field of view, or over the period of time that a set-up was observed for. To assess this potential problem we have tested the sky subtraction on a number of sky fibres from across the field of view and from different exposures in a set-up. No cases were found where over-subtraction had taken place but was not evidenced by absorption in the diagnostic lines. Figure 4.4 shows a selection of these test subtractions to illustrate this point.

The visual inspection of the residual spectra resulted in a preferred version of the sky frames to be used for each object in a configuration, and this was forced to be the same across all configurations for a given object to ensure a consistent method. In the vast majority of cases the median stacked sky frames performed better. It should be noted that since the spectra have not been corrected for the relative throughput of the fibres, it is not possible to flux calibrate spectra that have been sky subtracted in this manner. At this stage spectra for objects obtained in different configurations were co-added to arrive at the final spectra. These spectra are available on-line via the CDS service or from the Cluster collaboration homepage<sup>1</sup>.

---

<sup>1</sup><http://www.astro.ex.ac.uk/people/timn/Catalogues/description.html>

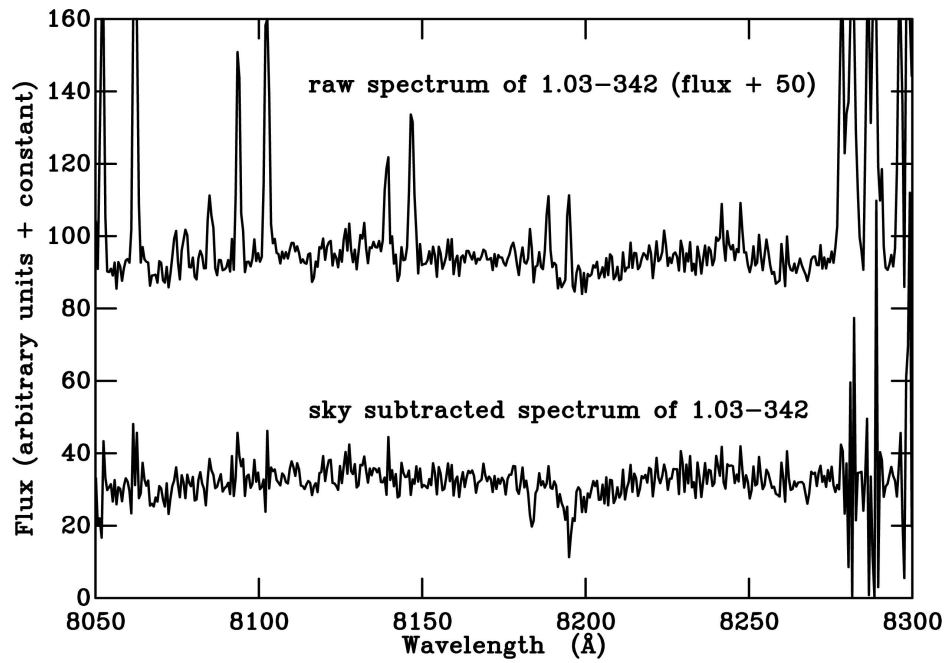


Figure 4.3: An example of the effectiveness of our method for sky subtraction. In this case, the median stacked exposures from 3.5 hours of the 7 hour total exposure time for our target 1.03-342 are sky subtracted using the method described above.

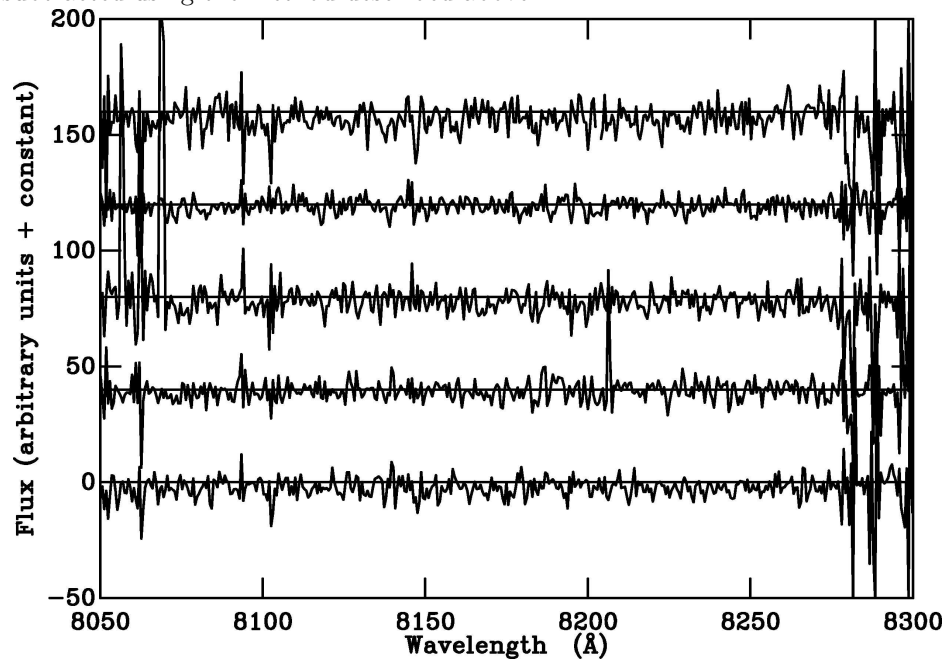


Figure 4.4: Examples of sky subtracted sky spectra used to check validity of using the diagnostic lines near 8150 Å

## 4.4 Selecting members by radial velocity

### 4.4.1 Sample selection

As discussed in Section 4.2.1, we did not obtain good data for every object in the sample. To avoid biasing our sample at this stage we opted to apply a signal-to-noise cut to select our sample. We measured the equivalent width of the Na I doublet, hereafter EW(Na I), in all the spectra obtained. We used two continuum bands: 1) 8151-8173 Å; 2) 8233-8255 Å. The wavelength range for continuum band 2 was selected to avoid the TiO band which lies redward of 8200 Å. We integrated EW(Na I) over the range 8180-8202 Å. Those objects which had a sufficiently small uncertainty to allow a  $2\sigma$  detection of the doublet at an equivalent width (EW) of 3 Å, i.e.  $\sigma \geq 1.5$  Å, were included in the sample. This EW was chosen as most brown dwarfs detected by Martín et al. (2004) in the Upper Scorpius OB association displayed an EW(Na I) above this value. The selected objects and their values for EW(Na I) are listed in Table 4.3. Our objective measure for the presence of Na I absorption was an EW(Na I) measured at a significance of  $2\sigma$  or greater. Our objective measure failed to detect Na I in 11 of the selected sample objects. We rule out the presence of Na I in a further 5 objects, despite the objective measure suggesting its presence. Using a  $2\sigma$  detection threshold, rather than a  $3\sigma$  detection threshold, made our selection more prone to false detections. However, since many objects in this study suffered from poor signal-to-noise, we decided that such a selection criterion was necessary if Na I were to be detected in a sufficient number of objects. False detections were then identified and removed on a subjective basis. These false detections were caused in two cases (1.03-460, 1.03-612) by the small sky line residuals affecting the continuum estimate. One false detection (8.03-396) was caused by over-subtracted sky lines within the EW integration band. The other two false detections (8.04-50, 8.04-77) were caused by unidentified absorption features encroaching on the EW integration band. Since no radial velocity can be obtained when Na I is not detected, we do not include such objects in our cross correlation nor do we calculate membership probabilities.

All of the objects with a failed Na I detection are fainter than I=17. The strength of the Na I doublet is gravity dependant, getting stronger with increasing surface gravity. As such it has been used as a discriminator between field dwarfs and giants (e.g. Schiavon et al., 1997) and field dwarfs

and young brown dwarfs (Martín et al., 2004). Failure to detect Na I in the spectrum of an object could indicate that it is a giant with a sufficiently low surface gravity to weaken Na I beyond our detection threshold. However, since very young brown dwarfs also have low surface gravity the same might be expected from members of the  $\sigma$  Ori group. Surface gravities are typically higher in young (age  $\leq 5$  Myrs) brown dwarfs,  $\log(g) \sim 3.5$ , than in M-giants,  $\log(g) \sim 0$  (Gorlova et al., 2003), so we might expect to be able to distinguish between extremely low surface gravity giants and young brown dwarfs. This will be discussed further in Section 4.5.

#### 4.4.2 Cross correlation of spectra to obtain radial velocities

We obtained radial velocities for objects in our sample which displayed Na I absorption by cross correlating their spectra against those of stars with known velocities and similar spectral types to our targets. The stars observed as radial velocity standards are detailed in Table 4.2. The wavelength range used for the cross correlation was restricted to 8175 - 8205 Å to minimise the effects of noise in the spectra. We restricted the range of acceptable correlations to be  $\pm 100 \text{ km s}^{-1}$ , and as a result velocities were not found for some objects on some cross correlations. Uncertainties for each velocity measurement were estimated by perturbing the value of the flux at each data point in the target spectrum by some value drawn from a Gaussian based on the uncertainty in the flux. This was repeated 100 times and the resulting spectra were cross correlated against the standards in the same manner as the original data. The uncertainty in velocity was taken to be the standard deviation in the distribution of velocities from the perturbed spectra. The quality of all cross correlation functions were assessed by visual inspection and none were found to have any evidence of the multiple peaks that might be expected if the sky subtraction introduced spurious features.

Although the 4 different velocity standards gave similar results, the use of GJ3517 gave the most successful correlations. As such, this is the one we chosen to use for further analysis. The velocities and uncertainties resulting from cross correlations against GJ 3517 are given in Table 4.3.

Table 4.2: Details of stars observed as radial velocity standards and details of their observations. Radial velocities listed are barycentric. Equivalent widths for Na I are measured with continuum bands at (8151-8173 Å) and (8233-8255 Å), and integrated over the range (8180-8202 Å).

Star	$\alpha$ (J2000)	$\delta$ (J2000)	Sp. Type	I	Integration time (s)	$V_{rad}$ / $\text{kms}^{-1}$	EW(Na I) / Å	$\sigma_{EW}$	Telluric reference
WX UMa	11 05 30.31	+43 31 16.6	M6		200	68 <sup>1</sup>	8.28	0.10	SAO 43460
GJ412A	11 05 28.58	+43 31 36.4	M0.5		10	68 <sup>1</sup>	2.18	0.09	SAO 43460
GJ3517	08 53 36.11	-03 29 32.4	M9	14.44	400	9 <sup>2</sup>	5.04	0.38	SAO 136434
LP213-67	10 47 12.65	+40 26 43.7	M6.5	13.17	600	5 <sup>3</sup>	6.55	0.21	SAO 62257

References for radial velocities: 1) Delfosse et al. (1998); 2) Tinney & Reid (1998); 3) Reid et al. (2002).

Table 4.3: Equivalent widths and radial velocities measured using the Na I doublet. The field number and object number refer to designations found in Kenyon et al. (2005). Quality flags for I and R-I are as described in Burningham et al. (2003). The continuum was measured from bands at 8151-8173 Å and 8233-8255 Å. The EWs were integrated over the range 8180-8202 Å. Radial velocities were measured by cross correlating against GJ3517, and corrected to give barycentric radial velocities.

Field	Object	$\alpha$ (J2000)	$\delta$ (J2000)	$I$	$\sigma_I$	Flag	$R - I$	$\sigma_{R-I}$	Flag	EW Å	$\sigma_{EW}$ Å	$V_{bar}$ kms <sup>-1</sup>	$\sigma_V$ kms <sup>-1</sup>	$P_{vel}$ %
1.01	319	05 39 48.911	-02 29 11.05	15.012	0.007	VV	1.595	0.011	VV	3.23	0.11	24.25	0.86	77.3
8.02	179	05 39 47.696	-02 36 22.96	15.064	0.005	OO	1.508	0.008	OO	3.04	0.10	26.37	1.13	99.9
4.03	229	05 38 23.536	-02 41 31.66	15.149	0.008	OO	1.686	0.013	OO	2.31	0.25	27.61	2.38	98.8
1.01	253	05 40 51.369	-02 31 49.93	15.232	0.007	OO	1.337	0.011	OO	3.21	0.30	10.48	4.91	0.0
8.02	143	05 39 56.445	-02 38 3.43	15.258	0.005	OO	1.725	0.007	OO	2.17	0.11	31.18	1.00	100.0
3.01	67	05 38 46.835	-02 36 43.38	15.278	0.016	OO	1.878	0.038	OO	0.64	0.10	32.11	1.32	100.0
2.03	260	05 39 30.561	-02 38 26.89	15.304	0.007	OO	1.320	0.011	OO	3.84	0.12	18.98	1.12	0.00
4.03	237	05 37 54.857	-02 41 9.15	15.400	0.006	VV	1.690	0.010	VV	1.32	0.39	33.86	3.56	89.5
1.03	60	05 40 30.179	-02 12 6.13	15.520	0.007	VV	1.594	0.011	VV	4.13	0.76	31.87	6.26	84.3
1.03	108	05 39 57.370	-02 10 41.98	15.545	0.007	OO	1.675	0.011	OO	3.59	0.18	29.15	1.93	100.0
8.04	188	05 40 42.887	-02 23 47.43	15.577	0.005	OO	1.413	0.007	OO	3.39	0.35	-32.22	2.00	0.00
3.01	51	05 38 23.070	-02 36 49.32	15.716	0.014	OO	1.423	0.022	OO	1.57	0.27	34.50	2.51	92.1
2.03	63	05 40 34.389	-02 44 9.52	15.770	0.007	OO	1.850	0.011	OO	3.28	0.17	33.15	1.24	100.0
4.03	29	05 38 22.824	-02 45 30.43	15.876	0.006	OO	1.314	0.010	OO	3.34	0.35	-10.71	7.19	0.00
4.03	368	05 38 26.833	-02 38 46.04	16.123	0.006	OO	1.911	0.011	OO	2.22	0.30	30.38	3.21	99.6
2.03	191	05 40 29.437	-02 40 55.91	16.229	0.005	OO	1.368	0.007	OO	3.48	0.25	XC failed	-	-
8.01	333	05 40 52.870	-02 38 23.49	16.246	0.005	OO	1.558	0.008	OO	2.46	0.47	29.98	3.38	99.4
4.04	481	05 38 36.374	-02 47 8.22	16.260	0.006	OO	1.527	0.011	OO	5.35	0.45	11.41	8.52	2.0
1.02	237	05 38 58.168	-02 21 11.70	16.283	0.007	VV	1.443	0.012	VV	2.32	0.24	-10.48	2.10	0.00
4.03	215	05 38 38.589	-02 41 55.86	16.472	0.006	OO	1.804	0.011	OO	2.65	0.39	31.11	4.10	97.3
1.01	343	05 40 23.389	-02 28 27.51	16.527	0.005	OO	1.551	0.008	OO	5.02	0.41	2.29	3.06	0.00
1.01	348	05 39 36.324	-02 28 8.18	16.808	0.008	OO	1.363	0.013	OO	3.37	0.84	-9.63	17.60	0.4
1.02	87	05 39 8.076	-02 31 32.22	16.811	0.008	OO	1.567	0.013	OO	3.05	0.24	-42.90	5.12	0.0
1.02	157	05 39 25.246	-02 27 48.15	16.856	0.008	OO	1.550	0.013	OO	3.64	0.28	28.86	2.47	99.8
3.01	480	05 38 38.888	-02 28 1.63	16.989	0.008	OO	1.777	0.013	OO	3.42	0.43	35.94	5.78	60.1
8.04	77	05 41 25.629	-02 30 38.53	17.050	0.007	OO	2.028	0.012	OO	6.83	0.85	-	-	-
1.03	110	05 39 56.919	-02 10 38.35	17.102	0.009	OO	1.674	0.015	OO	6.13	1.29	18.32	9.70	20.9

Table 4.3 (continued).

Field	Object	$\alpha$ (J2000)	$\delta$ (J2000)	$I$	$\sigma_I$	Flag	$R - I$	$\sigma_{R-I}$	Flag	EW Å	$\sigma_{EW}$ Å	$V_{bar}$ kms $^{-1}$	$\sigma_V$ kms $^{-1}$	$P_{vel}$ %
8.04	185	05 41 45.472	-02 24 16.24	17.102	0.007	OO	1.937	0.012	OO	0.56	1.47	-	-	-
1.01	237	05 39 36.726	-02 31 58.88	17.249	0.009	OO	1.485	0.015	OO	5.11	0.65	-9.78	3.46	0.0
8.04	128	05 41 12.228	-02 27 34.40	17.285	0.007	OO	1.787	0.013	OO	1.54	1.25	-	-	-
2.03	233	05 39 40.571	-02 39 12.32	17.293	0.009	OO	1.597	0.015	OO	2.80	0.67	39.84	6.23	25.9
4.03	285	05 38 44.487	-02 40 37.65	17.297	0.008	OO	2.127	0.017	OO	1.90	0.99	-	-	-
1.01	581	05 39 30.077	-02 33 16.14	17.337	0.009	OO	1.516	0.015	OO	4.25	0.85	-18.90	3.52	0.00
2.03	336	05 40 18.589	-02 36 14.57	17.392	0.006	OO	1.519	0.009	OO	4.69	0.70	-12.86	1.91	0.00
8.02	412	05 39 49.737	-02 23 51.80	17.484	0.007	OO	1.716	0.011	OO	6.49	0.50	15.06	5.34	1.0
8.04	50	05 41 10.419	-02 31 34.50	17.541	0.008	OO	1.908	0.019	OO	4.32	1.31	-	-	-
1.03	460	05 40 48.927	-02 08 12.06	17.555	0.013	OO	2.517	0.033	OO	1.70	0.65	-	-	-
1.03	557	05 40 7.241	-02 04 4.41	17.603	0.011	OO	1.723	0.019	OO	2.76	0.60	-23.74	6.44	0.00
1.03	493	05 40 1.742	-02 06 28.83	17.814	0.012	OO	1.620	0.020	OO	3.99	0.74	13.57	15.79	16.2
1.02	366	05 39 2.030	-02 35 30.30	18.062	0.023	OV	1.925	0.077	OV	4.52	1.13	-0.73	7.41	0.00
8.04	225	05 41 4.584	-02 32 25.98	18.079	0.010	OO	2.069	0.023	OO	2.55	0.68	27.42	2.07	99.4
1.03	342	05 40 3.305	-02 12 20.57	18.114	0.014	OO	1.750	0.026	OO	3.70	0.38	1.61	2.51	0.00
8.03	147	05 41 1.913	-02 19 3.99	18.203	0.011	OO	1.958	0.024	OO	1.11	0.88	-	-	-
2.03	617	05 40 24.775	-02 38 10.88	18.336	0.009	OO	1.989	0.019	OO	1.39	0.53	32.26	6.36	82.4
1.03	1094	05 40 36.238	-02 04 49.07	18.452	0.022	OO	2.052	0.047	OO	1.70	0.96	-	-	-
1.02	672	05 39 7.958	-02 15 43.04	18.540	0.019	OO	1.709	0.036	OO	1.00	0.59	-	-	-
1.01	800	05 40 12.537	-02 26 16.49	18.821	0.013	OO	1.838	0.027	OO	1.31	1.35	-	-	-
1.03	1029	05 39 51.156	-02 06 5.43	18.919	0.027	OO	1.894	0.056	OO	1.06	0.63	-	-	-
1.04	1100	05 40 19.740	-02 16 54.11	18.976	0.027	OO	2.182	0.066	OO	7.93	1.00	31.09	11.66	57.5
1.03	612	05 40 33.842	-02 13 42.97	19.295	0.038	OO	2.097	0.088	OO	2.52	0.77	-	-	-
8.03	457	05 40 58.366	-02 11 34.65	19.333	0.029	OO	2.407	0.079	OO	-1.82	0.69	-	-	-
8.03	396	05 41 4.416	-02 14 47.07	19.411	0.028	OO	2.146	0.070	OO	2.03	0.88	-	-	-
1.03	933	05 40 30.717	-02 08 6.78	19.573	0.053	OO	2.263	0.132	OO	2.22	1.19	-	-	-
8.02	2051	05 39 54.188	-02 26 25.25	19.709	0.031	OO	2.010	0.070	OO	-1.93	1.17	-	-	-

### 4.4.3 Membership probabilities

A histogram of the velocities obtained in the previous Section (Figure 4.5) shows that there is no simple velocity cut that will separate members of the  $\sigma$  Ori group from non-members. Also the velocities derived in the previous Section have a range of uncertainties, due the range of signal-to-noise in the different spectra, so a simple  $n\sigma$ -cut from a mean cluster velocity will tend to preferentially select poor signal-to-noise objects as members. Instead we can assign a probability of membership,  $P_{mem}$ , to each object for which we have a velocity. This probability is the product of the probability that the object is at an appropriate velocity to be considered a member,  $P_{vel}$ , and the probability that an object at that velocity is not a radial velocity contaminant,  $(1 - P_{cont})$ . The first question that must be answered, then, is what constitutes an appropriate velocity for membership of the cluster? We have plotted the cumulative probability distribution of the sample by summing Gaussians constructed from the velocities and uncertainties for all objects with a radial velocity. As can be seen in Figure 4.6, there is a strong peak in this distribution centred at  $29.5 \text{ kms}^{-1}$ . Since we do not resolve the velocity dispersion of the cluster, we can take the full width at the level of the background as the range of velocities occupied by cluster members.  $P_{vel}$  is then simply found as the fraction of the Gaussian derived from an object's velocity and error that lies within the cluster range. We take the cluster range to be  $24\text{-}37 \text{ kms}^{-1}$ , based on the peak's full width at the level of the background.

The value we find for the group velocity,  $29.5 \text{ kms}^{-1}$  (and the range of  $24\text{-}37 \text{ kms}^{-1}$ ), is consistent with that measured by Kenyon et al. (2005) of  $31.2 \text{ kms}^{-1}$ , and with the mean of values for members of this group measured by Muzerolle et al. (2003) of  $30.9 \text{ kms}^{-1}$ . It is also consistent with the mean radial velocity of  $\sigma$  Orionis itself of  $29.2 \pm 2.0 \text{ kms}^{-1}$  (Wilson, 1953). This is at odds with the value measured by Zapatero Osorio et al. (2002) of  $37.3 \text{ kms}^{-1}$ , but it is not clear why they have measured such a high velocity for this young group.

As can be seen in Table 4.3 our velocity uncertainties are typically much lower than the inherent velocity resolution of the spectrograph set-up of approximately  $50 \text{ kms}^{-1}$ . The size of our velocity range is dominated by the uncertainties in our measured velocities, and is not representative of the velocity dispersion of the  $\sigma$  Ori young group. OB associations typically have velocity dispersions of a few  $\text{kms}^{-1}$ . As such, we would require much higher resolution observations, and/or

considerably better signal-to-noise to resolve the velocity dispersion of this young group.

The probability that an object at the velocity of the cluster is a radial velocity contaminant can be taken as the ratio of the probability in Figure 4.6 integrated over a velocity interval equal in size to the cluster range (but lying in the non-cluster region) to the probability integrated over the cluster peak in Figure 4.6. We find  $P_{cont} = 0.2$  for this sample. We emphasise that this probability applies to the entire sample, i.e. over the entire C-M space examined. The value of  $P_{cont}$  will change if, for example, one limits ones attention to the ‘‘PMS’’ region of the CMD (see below). As such we only list values of  $P_{vel}$  in Table 4.3 so as to avoid misinterpretation of the results.

## 4.5 Discussion

In the following discussion we refer to the region redward of the solid line in Figure 4.7 as the expected PMS region. The region that lies blueward of this line is referred to as the background region. This locus was selected as the dividing line as it corresponds to a liberal photometric selection, and so provides an interesting case for investigating exclusion of members and contamination by non-members.

### 4.5.1 Are there members outside the ‘‘PMS’’ region?

The simplest way to answer this question is to examine the cumulative probability distribution of the velocities for the objects in the ‘‘background’’ region of the CMD. We have plotted this distribution with a dotted line in Figure 4.6. It is clear from this plot that there is no over-density in the probability distribution at the cluster velocity. Inspection of Figure 4.7 reveals that three objects with  $P_{vel} > 80\%$  lie in the expected background region of the CMD. This is consistent with the number of radial velocity contaminants that would be expected from inspection of Figure 4.6. This implies that there are not a significant number of members in the background region of the CMD, and hence photometric selection techniques are not excluding members of the  $\sigma$  Ori young group. This is the principal conclusion of this work.

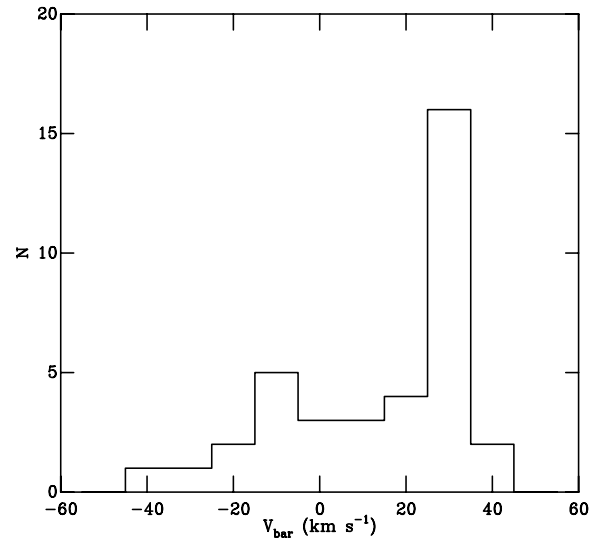


Figure 4.5: A histogram of the velocities measured from our sample.

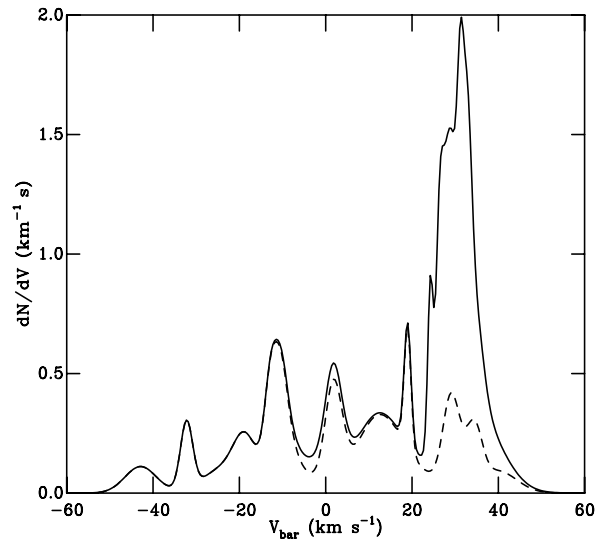


Figure 4.6: A plot of the cumulative probability distribution of our sample. The strongest peak is centred at  $29.5 \text{ km s}^{-1}$ . The dotted line traces the cumulative probability distribution of the objects in the “background” region of the CMD (see Figure 4.7).

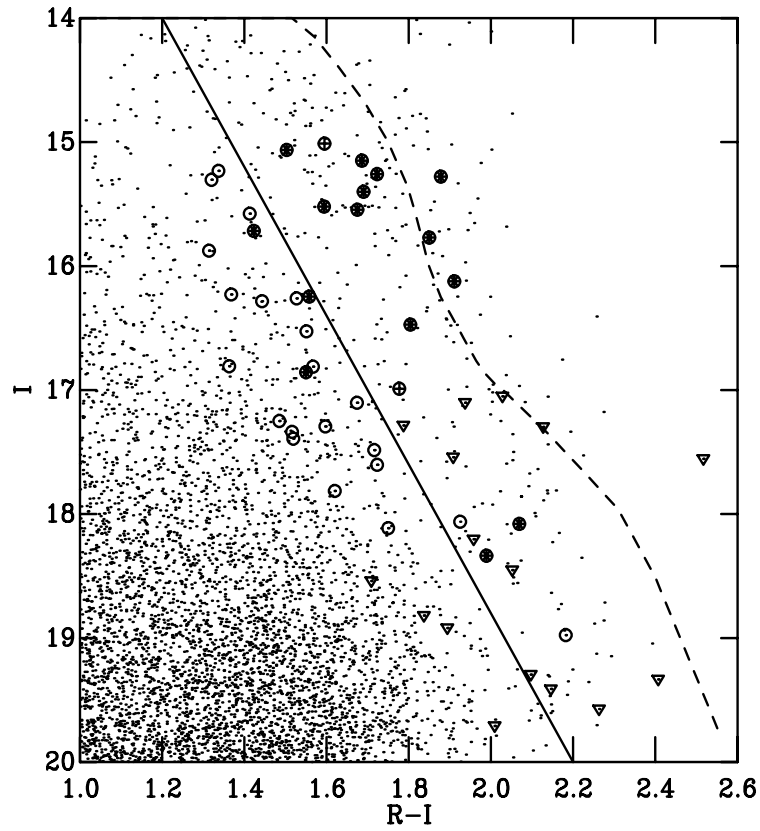


Figure 4.7: The CMD as in Figure 4.1. Objects with detected Na I are shown as open circles. Objects with  $P_{vel} > 80\%$  are circles filled with asterisks, whilst circles filled with crosses are objects with  $P_{vel} > 60\%$ . Objects for which no Na I was detected are shown with open triangles. The dotted line follows a NextGen 5 Myr isochrone (Chabrier & Baraffe, 1997; Baraffe et al., 2002). Our expected PMS region is defined as redward of the solid line.

### 4.5.2 Contamination within the “PMS” region

As can be seen in Figure 4.7, at magnitudes brighter than about  $I = 17$  we find that all of the objects in the expected PMS region have  $P_{vel} > 80\%$  except one, which has  $P_{vel} = 77.3\%$ . This is consistent with the result of Kenyon et al. (2005) that essentially all objects in the PMS region of the CMD are members of the  $\sigma$  Ori young group.

Fainter than  $I = 17$  the situation is somewhat different. We only detect Na I in 13 out of 29 objects in this part of our sample. The failure to detect Na I in so many objects in this part of the CMD makes a discussion of the contamination problems in this region impossible. However, this failure is itself worthy of some discussion. As already mentioned, the signal-to-noise threshold used to select our sample was chosen by comparison to Martín et al. (2004), who find  $EW(\text{Na I}) \geq 3 \text{ \AA}$  for all but 2 of their members of the 5 Myr old Upper Scorpius association. As such we expected that the majority of members of the similar aged  $\sigma$  Ori group might share this property. By comparing the EWs of members in both associations we can assess any differences between them. It would be simplest to compare the EWs of likely members in the two associations using  $J - I$  colours, since this is a fair proxy to spectral type, however 2MASS colours are only available for the 10 brightest of our likely members. Instead we compare the EWs in the two samples using the I-band magnitudes, corrected for the differing distances to the two associations.

Figure 4.8 shows that the likely members from our sample display weaker Na I EWs than the Martín et al. (2004) members of Upper Scorpius. This is not surprising in the case of the objects brighter than  $I = 17$  as they will be of earlier spectral type than any of the Martín et al. (2004) objects, and the Na I doublet gets weaker with increasing temperature at a given value of  $\log(g)$  (Schiavon et al., 1997). By this token, we might expect the fainter objects, presumably with later spectral types, to display stronger Na I absorption, however this does not seem to be the case. Both of the likely members with  $I > 17$  have  $EW(\text{Na I}) < 2.5 \text{ \AA}$ . Inspection of the measured EWs for the failed detections (see Table 4.3) indicates that the majority of them are consistent with values of  $EW(\text{Na I}) < 2 \text{ \AA}$ . This is somewhat lower than the typical values seen in the Martín et al. (2004) sample. Thus we are presented with two options: 1) the failed detections are interloping giants and sub-giants with low surface gravities; 2) many of the failed detections are member brown dwarfs which display weak Na I absorption. Option 1 requires many giant stars to be located at great

distance and along our line of sight, yet with colours that coincide with the expected PMS region of C-M space. Since the line of sight towards  $\sigma$  Ori is elevated  $-17.3^\circ$  from the galactic plane, it is hard to see that option 1 is feasible. Option 2, however, requires the low-mass objects in  $\sigma$  Ori to display consistently weaker Na I absorption in the 8183, 8195 Å doublet than has been observed in Upper Scorpius by Martín et al. (2004).

Upper Scorpius is thought to be marginally older than  $\sigma$  Ori, 5-10 Myrs versus 1-5 Myrs, so we might expect to see weaker Na I absorption in  $\sigma$  Ori, as  $\log(g)$  will be lower in the younger group. Mohanty et al. (2004) derive surface gravities for a number of low-mass objects in Upper Scorpius, and compare them to model predictions. They find that  $\log(g)$  changes from about 3.7 to 4.2 between 1 and 10 Myrs for a  $0.04 M_\odot$  brown dwarf ( $I = 18$  at the distance of  $\sigma$  Ori), and even less of a change at lower masses. Given that giants have  $\log(g) \approx 0$ , and display  $\text{EW}(\text{Na I}) \approx 1 \text{ \AA}$  (Schiavon et al., 1997), it is difficult to see how such a small change in  $\log(g)$  could give rise to the factor 2 discrepancy between the  $\text{EW}(\text{Na I})$  measured here for objects in  $\sigma$  Ori and those measured for objects in Upper Scorpius by Martín et al. (2004). The discrepancy between the two sets of EWs can likely be explained without resorting to a physical interpretation. The spectra used by Martín et al. (2004) are significantly lower resolution ( $R=900$ ) than those used here, and this could lead to placing the pseudo-continuum over blended absorption features such as the TiO band just redward of the Na I doublet. Thus we suggest that option 2 is the most likely explanation for these results. We can not determine if this is due to a physical difference between the two regions or if it has resulted from a difference in measurement techniques.

This result implies that it will be very hard to distinguish between background giants and member brown dwarfs based on the strength of Na I absorption.

The low values of  $\text{EW}(\text{Na I})$  implied for faint objects in our sample suggest that to avoid biasing such samples against finding members, observations should be made to a sufficient signal-to-noise to detect the Na I doublet in giant stars. Unfortunately, this destroys one of the main benefits of using the Na I doublet for radial velocity determination in main sequence stars, the ability to measure it at low signal-to-noise due to its strength. This is offset, however, by the fact the gravity sensitive nature of this doublet can provide a second diagnostic for contaminants

A possible weakness in use of radial velocities to define membership of young groups is the fact that bona fide members can be ruled out when they are members of binary systems. Dolan

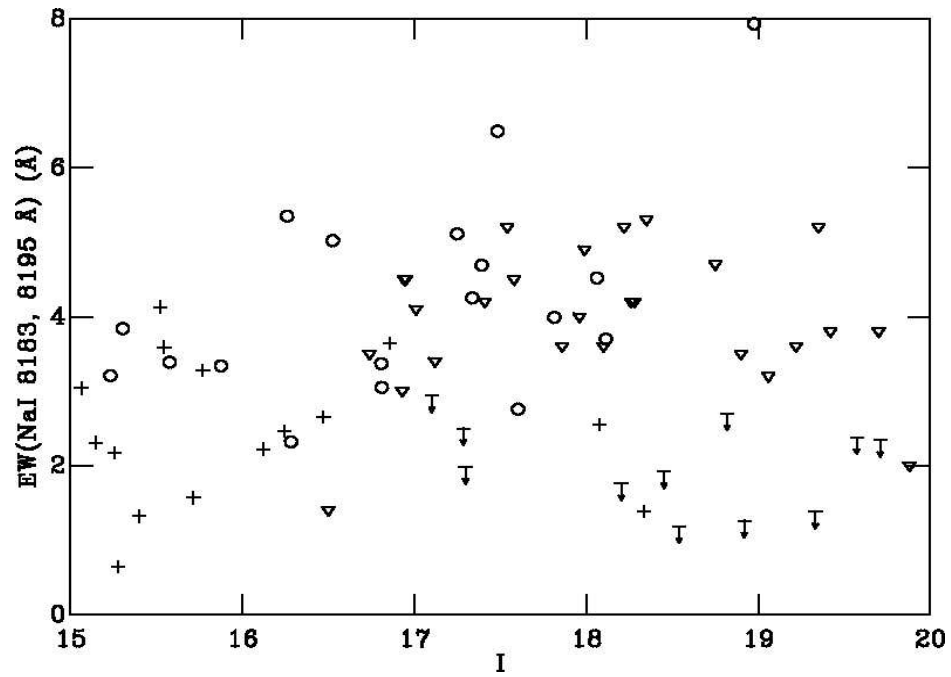


Figure 4.8: A plot of  $EW(\text{Na I})$  versus I-band magnitude for our objects with  $P_{vel} > 80\%$  (crosses),  $P_{vel} < 60\%$  (open circles) and Martín et al. (2004) members of Upper Scorpius (triangles). The magnitudes for the Upper Scorpius objects have been scaled for the distance to  $\sigma$  Ori. Also plotted are  $EW(\text{Na I})$  upper limits for the 11 objects for which our objective measure failed to detect Na I.

& Mathieu (2001) use the radial velocities in concert with the presence of lithium absorption at 6708 Å to identify 266 likely members of the  $\lambda$  Ori young group. They find that 9 objects with  $EW(\text{Li})$  consistent with youth are double lined binaries, while 3 appeared to be single line binaries. Whilst double lined binaries can be recognised as such, and not ruled out of membership lists, the single lined binaries would be ruled out in the absence of additional evidence of their membership. If we assume a similar binary fraction and distribution of properties as that seen by Dolan & Mathieu (2001) in  $\lambda$  Ori, we can estimate that for our sample of 18 likely members, we would not expect to identify any double lined binaries, or to miss any single lined ones. Since we cannot use  $EW(\text{Na I})$  to identify members, we cannot assess whether we have ruled out any single lined binaries from our membership lists. However, a significant departure from behaviour elsewhere in the Orion OB1 association would be required for a significant number of members to be ruled out due to binarity.

We have cross-correlated our sample against the candidate membership lists of Béjar et al. (1999, 2001). We find that only one object, 3.01 480, correlates in position with an object, SORI 68, from their sample. However, we do not believe that they are the same object since there is a nearly 6 magnitude discrepancy in their I-band brightness ( $I=16.99$  vs.  $I=23.78$ ). The fact that we do not share objects with the Béjar et al. (1999, 2001) sample is explained by a number of factors. Firstly, our  $RI$  catalogue excludes the regions immediately adjacent to the  $\sigma$  Ori multiple system, whereas the Béjar et al sample does not. In addition, our catalogue covers a much larger Section of sky (Kenyon et al., 2005), so there are many objects that Béjar et al were simply unable to select as candidates. Finally, we draw our sample from a wider region of C-M space than Béjar et al, and so we simply miss some of their candidates due to a lower density of selected objects.

## 4.6 Conclusions

We have carried out high resolution spectroscopy of the Na I doublet at 8183, 8195 Å of a sample of candidate low-mass stellar and sub-stellar members of the  $\sigma$  Ori young group drawn from a broad region of C-M space. We have selected a sample of 54 objects which displayed sufficient signal-to-noise to detect Na I with  $EW(\text{Na I}) = 3 \text{ \AA}$  at a significance of  $2\sigma$ , a criterion based on observations of brown dwarfs in Upper Scorpius by Martín et al. (2004). Significant ( $EW(\text{Na I}) > 2\sigma_{EW}$ )

Na I was detected in 38 of the 54 sample objects, and these were cross-correlated against an M9V standard to obtain radial velocities, which were then used to calculate membership probabilities. We find that 13 objects are likely radial velocity members ( $P_{vel} \geq 80\%$ ) of the  $\sigma$  Ori young group in the approximate mass range  $0.04M_{\odot} < M < 0.3M_{\odot}$ , assuming an age of 5 Myrs. Based on these probabilities, and the values measured for EW(Na I) we arrive at the following conclusions.

- 1) Photometric selection techniques do not exclude significant numbers of bona fide members of the  $\sigma$  Orionis young group
- 2) At I brighter than 17 ( $M \gtrsim 0.05M_{\odot}$  for an age of 3 Myrs) the expected PMS region of the CMD does not contain a significant number of contaminating non-members of the  $\sigma$  Orionis young group.
- 3) Very low-mass objects in the  $\sigma$  Ori young group appear to have weaker EW(Na I) than found by Martín et al. (2004) for low-mass members of the Upper Scorpius OB association. We have no explanation for why this is so, although we suggest measurement effects could account for this.
- 4) High resolution observations of the Na I doublet at 8183, 8195 Å offer the possibility of 2 membership diagnostics for very low-mass objects from a single observation. Ensuring observations are made to sufficient signal-to-noise to detect the doublet in the spectrum of a ( $\log g \approx 0$ ) giant star will avoid biasing a sample against bona fide members with lower than expected EW(Na I).

## 5 Can variability account for apparent age spreads in OB association colour-magnitude diagrams?

### 5.1 Introduction

In this chapter the theme of studying the statistical properties of PMS stars on a CMD will be continued. Having explored the reliability of photometric selection techniques in Chapter 4, such a selection will be used to study the origin of the spread of PMS stars on the CMD. As is discussed below, identifying the origin of this spread is of great interest in the context of determining the timescale for star formation. The following work has been published as a paper in the Monthly Notices of the Royal Astronomical Society (MNRAS) (Burningham et al., 2005a).

How long star formation takes is a significant unresolved question. Whether we are considering the entire process from the state of neutral interstellar hydrogen to the ZAMS, or just the portion of the process from the fragmentation of a giant molecular cloud (GMC) onwards, there is no consensus as to how long star formation takes. There are two competing paradigms of star formation currently proposed in the literature, which each give rise to very different timescales for star formation.

#### 5.1.1 Slow star formation

Shu (1977) put forward the model of star formation which we will refer to as slow star formation (SSF), which was reviewed by Shu et al. (1987). In this model, molecular cloud complexes are in dynamical equilibrium, with lifetimes of several tens of megayears and are supported against free fall collapse by magnetic fields. However, in clumps where the density is  $n \gtrsim 10^5 \text{ cm}^{-3}$ , the ionisation fraction can be sufficiently low that the neutral molecular material may diffuse through the magnetic field, removing flux from the core (ambipolar diffusion), leading to higher degrees of central condensation. Eventually the field can no longer support the, now prestellar, core against gravitational collapse to form a hydrostatic protostar.

Typically, predicted ambipolar diffusion timescales lie in the range 5-10 Myrs. This is consistent with the observed lifetimes of pre-stellar cores with  $10^5 < n < 10^6 \text{ cm}^{-3}$  found by Ward-

Thompson et al. (1994) to be  $\sim 10^6$  yrs, through comparison of the number of starless cores versus protostellar cores. However, Jijina et al. (1999) performed a more comprehensive study of protostellar cores using ammonia emission. They found the ratio of starless to stellar cores to be too small to be consistent with that expected if the ambipolar diffusion timescale governed core lifetimes. This suggests that the timescale of the starless core phase is much less than the ambipolar diffusion timescale.

### 5.1.2 Rapid star formation

More recently, an alternative paradigm for pre-stellar core formation and collapse has been discussed in the literature (e.g. Ballesteros-Paredes et al., 1999; Hartmann et al., 2001; Hartmann, 2001; Elmegreen, 2000). In this model the star formation rate is regulated by supersonic turbulence, not magnetic fields. Since supersonic turbulence in self-gravitating clouds is expected to decay rapidly, the cloud support mechanism in this picture leads to a short cloud lifetime compared to that in SSF (Pringle et al., 2001). So, rather than being long-lived structures, GMCs are treated as transient objects that form through interactions between supersonic flows in the interstellar medium. The whole process from formation of the GMCs through to the arrival of the pre-main-sequence (PMS) stars on the birthline is expected to take around 3 Myrs, with collapse of cores to form protostars occurring almost immediately. As such we will refer to this model as rapid star formation (RSF). RSF has a number of distinct advantages over SSF, both observationally and theoretically which are reviewed by Mac Low & Klessen (2004).

### 5.1.3 Age spreads

The presence of apparent age spreads has been observed in a number of young clusters (e.g. Herbst & Miller, 1982; Sung et al., 1998) and associations (e.g. Pozzo et al., 2003; Dolan & Mathieu, 2001) and their sizes have been presented as evidence in favour of both SSF and RSF. Palla & Stahler (2000) investigated apparent age spreads in a number of young star forming regions and found evidence of accelerating star formation, which they use to argue in favour of SSF. A further study by the same authors into the age spread in the Taurus-Auriga region also found evidence of accelerating star formation (Palla & Stahler, 2002). The evidence of accelerating star formation

in the regions studied by these authors came in the form of distributions of stellar ages that were, generally, strongly peaked at 1 - 2 Myrs, with few PMS stars older than this. As Hartmann (2003) pointed out, this surely implies there is something special about the last 1-2 Myrs, if such widely separated regions have formed the majority of their stars at the same time, whilst their overall lifetimes are  $\sim 10$  Myrs. Such an uncomfortable, special, state of affairs is not required if the one accepts the RSF paradigm. This is because the strong peaking of age distributions at 1-2 Myrs follows naturally if this is the timescale for cloud and star formation (Hartmann, 2003).

Elmegreen (2000) found that the ages spreads seen in a number of OB associations and clusters are comparable to the inferred crossing time for the parent cloud. The conclusion that is drawn from this is that the age spread is indicative of the timescale for star formation, and that this is comparable to the crossing time, as expected for RSF. However, his data reveal that the age spreads also scale with the mean ages for the groups he uses. This scaling of apparent age spreads with mean age for clusters and associations suggests that the age spreads originate from a photometric scatter of given magnitude. The size of this spread is much larger than any photometric uncertainties. Since PMS objects move more slowly through colour-magnitude space at older ages, a given photometric scatter will naturally imply larger age spread as the mean age rises. The correlation of spread with inferred crossing time may also arise as a result of the fact that older open clusters and associations are larger and thus a longer crossing time is inferred for the parent cloud.

Hartmann (2001, 2003) disputed the results and conclusions of Palla & Stahler (2000, 2002), arguing that the actual age spreads are much smaller than those observed, but accepted that the presence of such large age spreads ( $10^7$  yrs) would be a problem for the RSF paradigm. Additionally, it is not clear that the interpretation of the age spreads being indicative of timescale is correct. Tassis & Mouschovias (2004) pointed out that interpretation of age spreads in this manner already assumes a core formation timescale that is essentially instantaneous with respect to the lifetime of the molecular cloud,  $\tau_{mc}$ . In reality, an age spread could only tell us the difference between  $\tau_{mc}$  and the timescale for forming a body that will survive the destruction of the molecular cloud, the core formation timescale,  $\tau_{cf}$ . So:  $\tau_{spread} = \tau_{mc} - \tau_{cf}$ . As such, interpretation of any spread in ages is dependent on knowledge of either  $\tau_{cf}$  or  $\tau_{mc}$ .

Incidentally, this point is also relevant to the argument put forward by Hartmann et al.

(2001) that, since very few young clusters or associations older than 3 Myrs are associated with their parent cloud, star formation must occur on a timescale of about 3 Myrs. This also implicitly assumes that  $\tau_{cf}$  is short. The same observational evidence could indicate that star formation is slow, but that the cloud is disrupted quickly after the first PMS stars arrive at the birthline. However, as pointed out by Hartmann et al. (2001), the vast majority of local molecular cloud complexes show evidence of star formation. This must imply that  $\tau_{cf}$  should be short, or the question must surely be asked as to the whereabouts of the clouds which are still mostly in the pre-stellar phase of star formation. This is reflected in the results of Jijina et al. (1999), described earlier, that the ratios of pre-stellar to stellar cores found in molecular clouds are far below the 3 to 30:1 range required by SSF.

It is important to recognise, however, that the reality of apparent age spreads has not been well established. The principal evidence for spreads of ages actually comes from an observed spread of PMS stars in colour-magnitude (C-M) space. A single age would be expected to give rise to a much more narrow distribution of stars about an isochrone. There are a number of plausible alternatives that could explain such C-M spreads for a population that in reality arrived at the birthline simultaneously. For example accretion-driven age spread (Tout et al., 1999) could give rise to an apparent spread of ages for an ensemble of objects with differing accretion histories. Hartmann (2001) explored a number of other factors that might be expected to influence the degree of observed age spread. These included variable extinction, photometric variability, differences in accretion luminosities and the presence of unresolved binaries. Establishing the influence of variability and binarity on the width of the PMS in OB association-like environments is the aim of this work. We have obtained 2 epoch, 2 colour photometry for 2 regions with differing photometric spreads to investigate this effect. The 2 regions studied here are within well known OB associations: Cep OB3b and the  $\sigma$  Orionis young group (part of the Orion OB1b association). We have simulated the degree of spread introduced by variability on timescales of less than 1 year in Cep OB3b and less than 4 years in  $\sigma$  Ori. By comparing 2 colour catalogues of PMS objects within these associations we have estimated their variability, and used this to simulate the PMS in C-M space, assuming a single isochronal age for the objects.

#### 5.1.4 PMS variability

Photometric variability in PMS stars occurs across a wide range of timescales and amplitudes. Typically smallest in amplitude is the periodic variability thought to be associated with rotation of cool regions in the photosphere. Such variability has been used by a number of authors to derive rotation periods for PMS stars (e.g. Littlefair et al., 2005; Makidon et al., 2004). Periods are found to range from a few hours to several weeks, with I-band amplitudes typically smaller than 0.5 mags. Where multicolour observations have been used, amplitudes are found to decrease with increasing wavelength, as expected if the variations are caused by the rotation of cool, dark, photospheric spots (Herbst et al., 1994). Variability attributable to cool spots is most easily observed in WTTSs, however, analogous variations caused by the rotation of hot spots are observed in CTTSs. These hot spots are understood as the footprints of magnetically channelled accretion columns. Amplitudes for these variations are larger, though typically they remain smaller than 1 magnitude in the V-band (Herbst et al., 1994).

Non-periodic variability in PMS stars takes several forms. Irregular ‘flickering’ on timescales of several days has been observed frequently for CTTSs, with amplitudes of up to approximately 1.5 mags in the I-band (e.g. Littlefair et al., 2005; Herbst et al., 1994). This has commonly been attributed to variations in the accretion rate. Occultation of the photosphere by disk material has been suggested as a mechanism for longer timescale irregular variability, as in the case of the PMS star UX Ori (Herbst et al., 1994) or, more recently, KH15D (Hamilton et al., 2001). This type of variation has been observed on timescales of days, weeks and years. It is typified by a dips in brightness, typically of less than 1 magnitude from the mean, though some objects vary by more than 3 magnitudes (Herbst & Shevchenko, 1999).

The most spectacular variations that are observed in PMS stars are FU Ori outbursts. During one of these events the brightness of a PMS star may increase by several magnitudes. In the case of the prototypical outburst of 1936-37, the brightness FU Ori increased by 6 magnitudes in  $B$  over the course of a few months, but declined by less than a magnitude during the subsequent four decades (Herbig, 1977). Several examples of objects that have undergone such events are now known, with timescales for reaching maximum ranging from a few months to decades (e.g. Herbig, 1977; Ibragimov, 1997; Hartmann & Kenyon, 1996). The FU Ori phenomenon is attributed to

episodes during which the mass accretion rate through the circumstellar disk of a T Tauri star rises as high as  $10^{-4}M_{\odot}yr^{-1}$ , from the low state of typically  $10^{-7}M_{\odot}yr^{-1}$  (e.g. Hartmann & Kenyon, 1985, 1987; Kenyon et al., 1988).

### 5.1.5 PMS binaries

The presence of unresolved binary systems is expected to broaden the PMS in C-M space as binary systems will be brighter, and, in the cases where the mass ratio ( $q$ ) is less than 1, redder than the expected colour and magnitude for the primary. Determining properties such as binary fraction, mass ratio and period distribution in PMS populations has been attempted for the last 20 years or so. The Taurus-Auriga (Tau-Aur) T-association has been intensively studied by a number of authors. Leinert et al. (1993) found  $42\pm 6\%$  of systems to be multiple systems. In a review of work on PMS binaries, Mathieu (1994) drew several studies together to arrive at lower limit of 51% for multiple systems in the same region. The results of several studies into the period distribution of PMS binaries are also drawn together in the same review. The distribution of orbital periods is found to peak at between 4 and 6 days, which is similar to what is found for main-sequence binaries. Ghez et al. (1993) found a somewhat smaller proportion of binary systems in the Scorpius-Ophiucus region of  $34\pm 7\%$ .

Reipurth & Zinnecker (1993) investigated binary systems with separations of between 150 and 1800 AU, and found that  $16\pm 3\%$  of systems in the southern hemisphere within 150 pc are of that type. The same study also found that the frequency of such binaries decreased with increasing separation. Mathieu (1992), on the other hand, found that short period binaries were less common than intermediate period binaries in Tau-Aur. More recently, Kraus et al. (2005) found binary fraction of  $33\pm 17\%$  in the Upper Scorpius OB association, considerably lower than the lower limit of 51% found by Mathieu (1994) for Tau-Aur. Siess et al. (1997) simulated the H-R diagram for the Pleiades, and found that a binary fraction of  $40\pm 5\%$  was required for a good match the real H-R diagram.

The distribution of mass ratios for low-mass PMS binaries is not well constrained at this time, due to the small number of PMS spectroscopic binaries that have been identified in any one star forming region. For low-mass main-sequence stars, however, the mass ratio distribution has

been found to be bimodal, with peaks located at  $q \sim 0.8$  and  $q \sim 0.2$  (Goldberg et al., 2003). Most recently, Burgasser et al. (2006) have characterised the mass ratio distribution for very low-mass objects as being strongly peaked at equal masses (with  $q > 0.8$ ), with most binaries being found with small separations.

The rest of this chapter is laid out as follows. In Section 5.2 we describe our observations and data reduction. In Section 5.3 we describe how we have simulated the spreads in each of our associations in turn, and give the basic results. These results are discussed in Section 5.4, and our conclusions are summarised in Section 5.5.

## 5.2 Observations and data reduction

All observations were carried out using the Wide Field Camera (WFC) mounted on the Isaac Newton Telescope (INT) at the Roque de los Muchachos Observatory, La Palma. Our first epoch data set for  $\sigma$  Ori is the same as that presented by Kenyon et al. (2005). It was made up of observations taken on the nights of 27-30 September 1999 of 5 fields of view (FoV) in the Harris  $R$  and Sloan  $i'$  filters. We carried out observations of 4 FoVs coincident with Kenyon et al's survey on the night of 7 September 2003, using the same filters. The new observations are detailed in Table 5.1. We have obtained new data for both epochs for our Cep OB3b survey. We have observed a single WFC FoV in this region, chosen to cover the area with the highest density of PMS objects identified by Pozzo et al. (2003). Observations were taken on the nights of 12 September 2003 and 28 September 2004 using Harris  $V$  and Sloan  $i'$  filters. Again the observations are detailed in Table 5.1. The observations of 28 September 2004 were carried out by Dr. Stuart Littlefair and Mr. Eric Saunders.

Data obtained in 2003 and 2004 were reduced in an identical manner. Flatfields and data frames were linearised using the 2003 August coefficients<sup>1</sup>, and then bias subtracted using a median bias frame specific to each night. We flat fielded the data using frames constructed from twilight sky flatfields taken during the same observing runs as the data being corrected. The  $i'$ -band frames were successfully defringed using a fringe frame from 2001 September, obtained from the web pages

---

<sup>1</sup>See <http://www.ast.cam.ac.uk/~wfcsur/technical/foibles/index.php> for details

of the Cambridge Astronomy Survey Unit (CASU).

Optimal photometry was performed using the method laid out by Naylor (1998) and Naylor et al. (2002), and described in detail in Chapter 2. We have allowed the profile correction to vary with position on each chip, and fitted it with a 3rd order polynomial in the x-axis and a 5th order polynomial in the y-axis. We do not apply the ‘ill-determined sky’ flag for the Cep OB3b data, and we allow the thresholds for its application to vary from field to field for the  $\sigma$  Ori data. For obvious reasons we did not apply the ‘variable’ data quality flag to reject objects that showed evidence of variability. An astrometric solution was obtained through comparison with a 2MASS catalogue for each FoV. The RMS of the residuals to the 6-coefficient fits were all less than 0.1 arcsec.

As described in Chapter 2, overlap regions between pointings were used to normalise the catalogues for each pointing onto a single system. We have used the same method to bring observations from 2 epochs for each of our target regions to the same system. In the case of the  $\sigma$  Ori data, the way in which flatfields were normalised had changed between the two epochs, so the data from each epoch were treated slightly differently. When the 1999 data were reduced, the flatfield for each chip on the WFC was normalised separately. By the time the 2003 data were reduced, the reduction software had been changed such that the flatfields for all 4 chips in each pointing were normalised together. As such, prior to catalogue normalisation, the 1999 exposures were combined to produce 1 catalogue for each chip, whilst the 2003 exposures were combined to produce 1 catalogue for each pointing. The overlap regions between the interlocking pointings were then used to normalise the catalogues onto a single system.

To verify that there were no major sources of error introduced at the image processing stage we checked that the distribution of positive and negative differences between observations were uniform with position on the sky for the  $\sigma$  Ori data. We found that the trends in the differences between observations were correlated with the pixel coordinates on each chip from the 1st epoch catalogue. Kenyon et al. (2005) found the RMS of differences between overlap stars seen in their data to be 0.05 mags and speculated that it was due to problems with the flatfield, which is consistent with what has been seen here. They state that the camera was suffering from light leaks during their observing run, and it is likely that this is the origin of the problem. We fitted the trends in the differences in x and y for each chip with 1st and 2nd order polynomial functions, and corrected the magnitudes of the objects in the 1st epoch catalogue accordingly, prior to re-

normalising the 2 epochs. The RMS of the differences in the magnitudes in the interlocking overlap regions after normalisation suggested that an additional magnitude independent uncertainty of about 0.01 mags was also present. As in Naylor et al. (2002), this uncertainty was included in the uncertainty estimate for all objects. Following this we found that positive and negative differences for the  $\sigma$  Ori data were spatially uncorrelated.

Since no overlap regions were present in the Cep OB3b data sets, we could not use the results of the normalisation to determine the size of any additional uncertainty, so we applied the same value as found for the  $\sigma$  Ori data set. The distribution of positive and negative differences were found to be spatially uncorrelated in the Cep OB3b data set.

We have not applied a measured photometric calibration to our final catalogues as this would have involved transforming our Harris and Sloan magnitudes and colours into the Cousins system. Such a transformation would risk introducing spurious correlations between variability and colour, whilst not improving our experiment in any way. As such we have simply applied mean zero points to our magnitudes and colour coefficients to our colours to construct our CMDs.

## 5.3 Simulation of photometric spreads

### 5.3.1 The $\sigma$ Ori subgroup

The  $\sigma$  Ori young group has been the subject of a number of spectroscopic studies aimed at identifying bona fide members. In particular two campaigns (Kenyon et al., 2005; Burningham et al., 2005b) were successful in identifying a large number of members present in the catalogue obtained from the 1st epoch observations. The latter of these is described in Chapter 4 of this thesis. Importantly, these spectroscopic surveys also demonstrated that photometric selection of the PMS objects in this region is not subject to serious contamination, and does not miss significant numbers of bona fide members. As such we have used the membership lists from these studies to define a PMS region in the CMD, with minimal contamination, from which we have drawn our sample (see Figure 5.1). Only objects with little doubt as to their membership have been used to guide the photometric selection. In the case of the Burningham et al. (2005b) catalogue this meant objects with greater than 90% membership velocity probability. In the case of the Kenyon et al. (2005)

catalogue this meant objects which displayed strong Li absorption, evidence of low surface gravity and the appropriate radial velocity.

To test if the observed C-M spread is affected by variability we have assumed a single age for the young group and then simulated the PMS using an estimate of each object's variability, derived from our 2 epoch observations. This method implicitly includes the effect of photometric uncertainty.

To verify that our PMS selection is indeed more variable than the background we have compared the RMSs of the differences between the two sets of observations for the background objects and for the PMS selection. To make such a comparison meaningful we have restricted our sample to those  $i'$  magnitudes where the uncertainties are small. In Figure 5.2 we plot the uncertainty in the  $R - i'$  differences (thus incorporating uncertainties from both epochs) against  $i'$  (2nd epoch). As can be seen, the uncertainties rise sharply fainter than  $i' = 18$ , as the uncertainty in the photon counting statistics of the sky begins to dominate. Brighter than  $i' = 16$ , some objects also display higher uncertainties. This is because for these points the 1st epoch data were drawn mainly from a short exposure. In the range  $15 < i' < 18$  the uncertainties are dominated by the small magnitude independent uncertainty measured during the normalisation of the catalogues (see Naylor et al., 2002, and Section 5.2). Based on this plot we restrict our comparison of the RMSs to the range  $15 < i' < 18$ . The RMS of the differences between the two sets of observations indicate that the objects in the photometric PMS selection are significantly more variable than those in the background. The RMS for the differences in  $i'$  are 0.05 for the background and 0.09 for the PMS region. In  $R - i'$  the RMSs are smaller: 0.02 for the background; 0.04 for the PMS region.

We placed the objects on a single empirical isochrone by fitting a 3rd order polynomial to the photometrically selected PMS in the CMD. Each point used for fitting the polynomial is weighted according to its uncertainty in  $R - i'$ , with the points carrying the greatest uncertainty having the smallest influence on the fit. A point was then placed on this empirical isochrone at the appropriate magnitude for each PMS object. One can view this as moving each point in colour until it falls on the isochrone.

Having placed each point on the isochrone, we simulated the effect of binaries by splitting this empirical isochrone into a single star and an equal mass binary sequence. We did not assume

Table 5.1: Summary of Observations

Field Name	$\sigma$ Ori 1		$\sigma$ Ori 2		$\sigma$ Ori 3		$\sigma$ Ori 4		Cep OB3b	
RA(J2000)	05 40 14.2		05 40 13.1		05 38 07.7		05 38 07.4		22 55 43.3	
Dec(J2000)	-02 20 18.1		-02 51 48.0		-02 20 18.0		-02 51 51.0		+62 40 13.7	
Filter	R	$i'$	R	$i'$	R	$i'$	R	$i'$	V	$i'$
2003-09-07	600s	300s	600s	300s	600s	300s	600s	300s	-	-
2003-09-12	-	-	-	-	-	-	-	-	30s, 2s	13s, 2s
2004-09-28	-	-	-	-	-	-	-	-	30s, 5s	300s, 30s, 5s

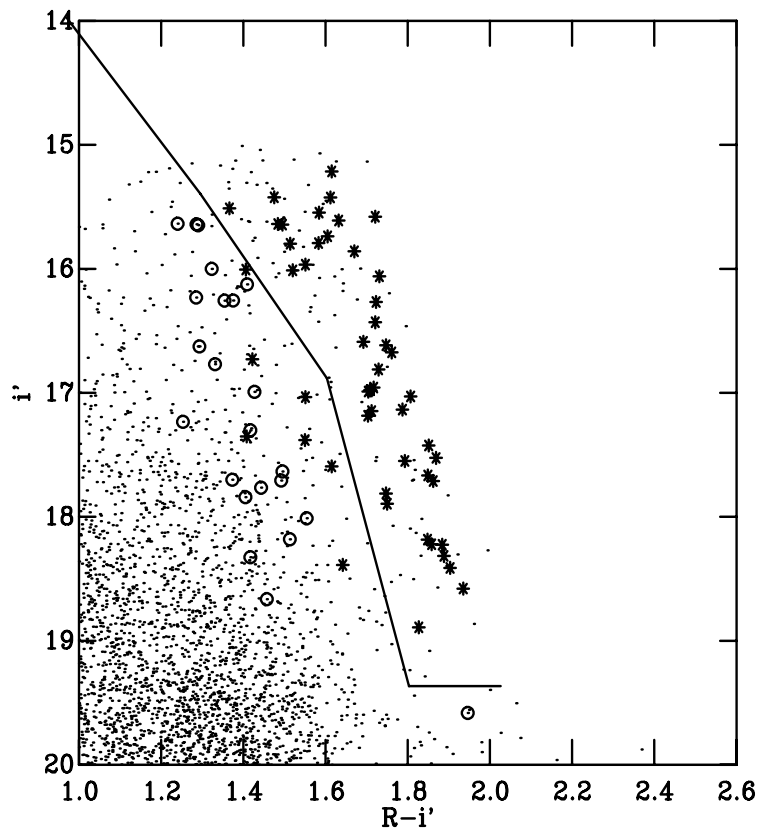


Figure 5.1: The CMD for the 2nd epoch  $Ri'$  catalogue. Spectroscopic members of Kenyon et al. (2005) and Burningham et al. (2005b) are shown as asterisks. Objects identified as non-members in the same studies are shown as open circles. The solid line indicates the location of the cut for our PMS selection.

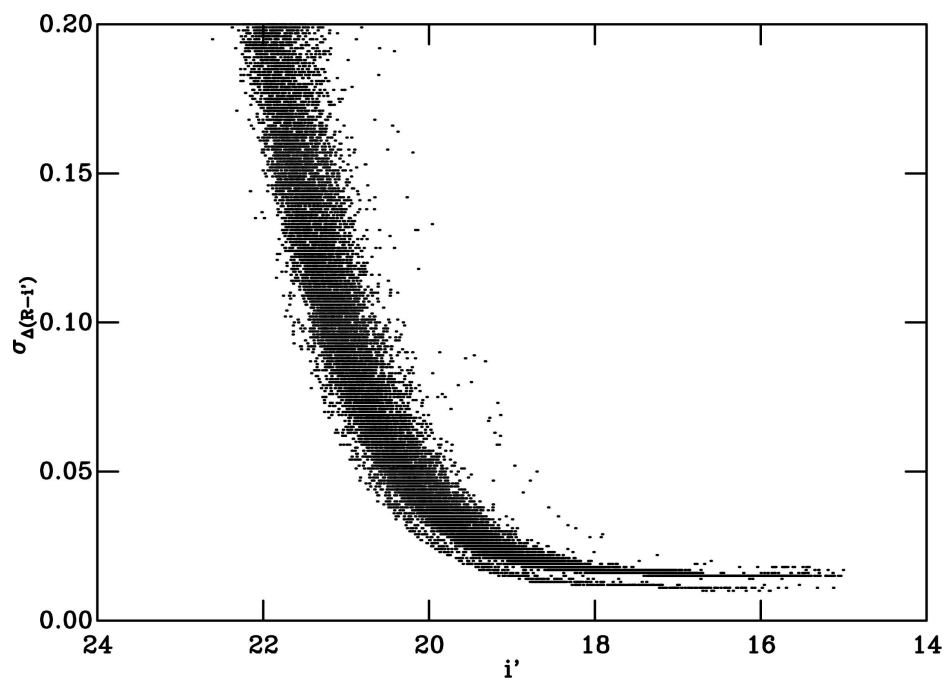


Figure 5.2: A plot of the uncertainty in  $\Delta(R - i')$  against  $i'$  for the FoV centred on the  $\sigma$  Ori subgroup.

a binary fraction, but rather simulated spreads with a range of fractions. For each binary fraction we randomly selected that proportion of objects to be offset in magnitude by an amount equal to  $0.75(1 - f_{bin})$ , and the rest by  $0.75 - 0.75(1 - f_{bin})$ . This gave rise to a difference of 0.75 mag between the two sequences, as would be expected from equal mass binaries. We do not attempt to simulate  $q < 1$  binaries as these would fall within the envelope bounded by our two sequences, and thus would not have a significant impact the results of this investigation.

To simulate the effect of variability we next moved each point by an amount in both magnitude and colour equal to  $(\Delta/\sqrt{2})$ , where  $\Delta$  is the observed difference between the two observations for that point. Characterising the variability in this manner for each object in turn has distinct advantages over parameterising the scatter of the whole sample, as any correlations between  $\Delta i'$  and  $\Delta(R - i')$  have been included without any assumptions as to the source of the variability. Furthermore, any correlation of variability with magnitude has also been included, as has the influence of photometric uncertainty.

A further source of scatter that might influence the observed spread is differential reddening. We have neglected the effects of differential reddening in this simulation since the extinction towards  $\sigma$  Ori is low, with a colour excess of just  $E(B - V) = 0.05$  (Lee, 1968). To select which binary fraction gave the best match to the data, and thus which one would be used for subsequent analysis, we constructed a  $\chi^2_\nu$  estimate for each simulation by comparing a histogram of the residuals in  $R - i'$  from the polynomial fit to the data, with a histogram of the residuals from a polynomial fit to the simulation. The histograms were all constructed in an identical manner: we placed the residuals in bins of width 0.05 mags starting at -0.5 and ending at +0.5. Because we used a random number generator to select the objects that make up the binary sequence, we ran each simulation 1000 times to obtain a mean value for  $\chi^2_\nu$ , thus reducing the noise for the determination of the most likely binary fraction. Figure 5.3 shows a plot of mean  $\chi^2_\nu$  against binary fraction. Clearly there is no sharp minimum in the value of  $\chi^2_\nu$ , but a broad minimum is centred on 50%. We present one realisation of the simulation for a binary fraction of 50% in Figure 5.4.

Comparison of panels (a) and (c) in Figure 5.4 indicates that the combination of variability and binarity are not able to account for the spread in the PMS. In Figure 5.5 we show histograms of the residuals about 3<sup>rd</sup> order polynomial fits to the observed PMS and the simulated PMS (solid and dotted line) for the  $15 < i' < 18$  region of the CMD. Again, it is clear that the combination

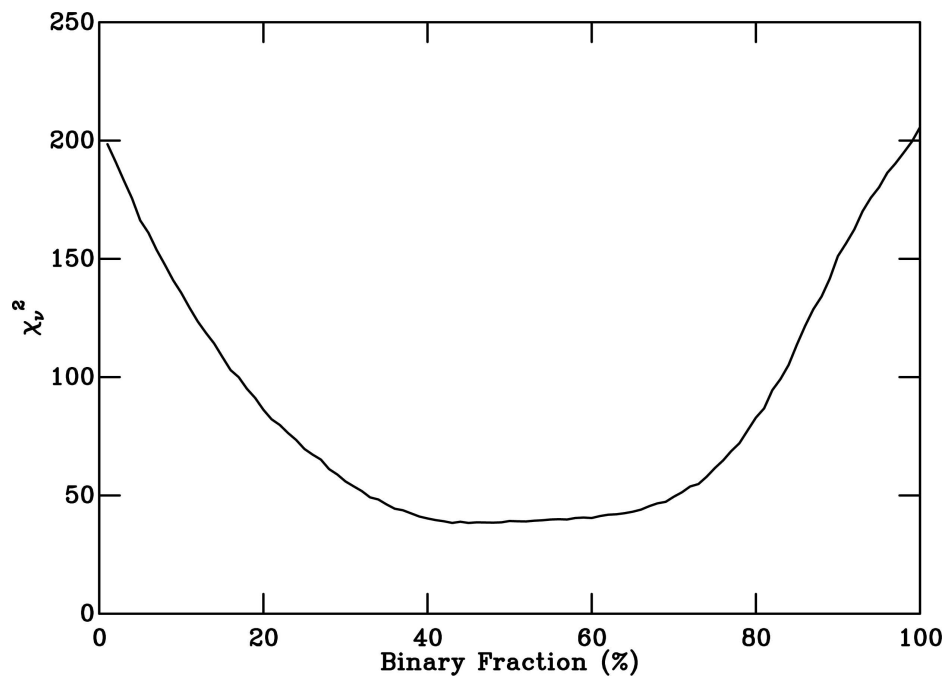


Figure 5.3: The mean  $\chi^2$  for the simulated PMS compared to the observed PMS plotted against binary fraction, shown as a percentage for the PMS objects near  $\sigma$  Ori.

of binarity and variability on timescales of  $\sim 4$  years, are not sufficient to explain the spread in C-M space for this PMS. With such a poor match to the observed spread it is clear why Figure 5.3 displays no sharp minimum in  $\chi_\nu^2$ , but rather a broad minimum centred on 50%. A binary fraction of 50% maximises the size of the spread, for a given estimate of variability. The assumption of a  $q = 1$  binary population also increases the value of  $\chi_\nu^2$  as it introduces a double peak to the spread which is not present in the data. The FWHM of the spread in residuals in  $(R - i')$  about the polynomial fit to the observed PMS, shown in Figure 5.5 is approximately 0.3 mags. This is consistent with the width of the PMS observed by Sherry et al. (2004) in  $V - I$  for more massive members of the same group.

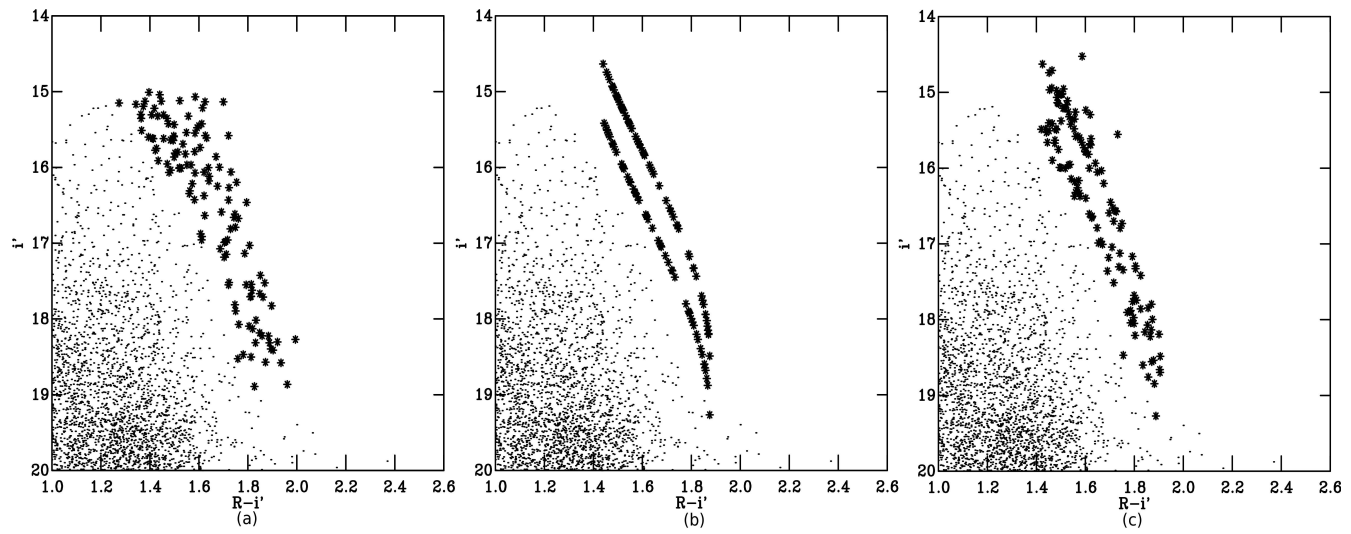


Figure 5.4: CMDs for the  $\sigma$  Ori young group showing: (a) the PMS selected objects as asterisks; (b) the fitted single star and binary sequences for a binary fraction of 50%; (c) the simulated PMS for the same binary fraction.

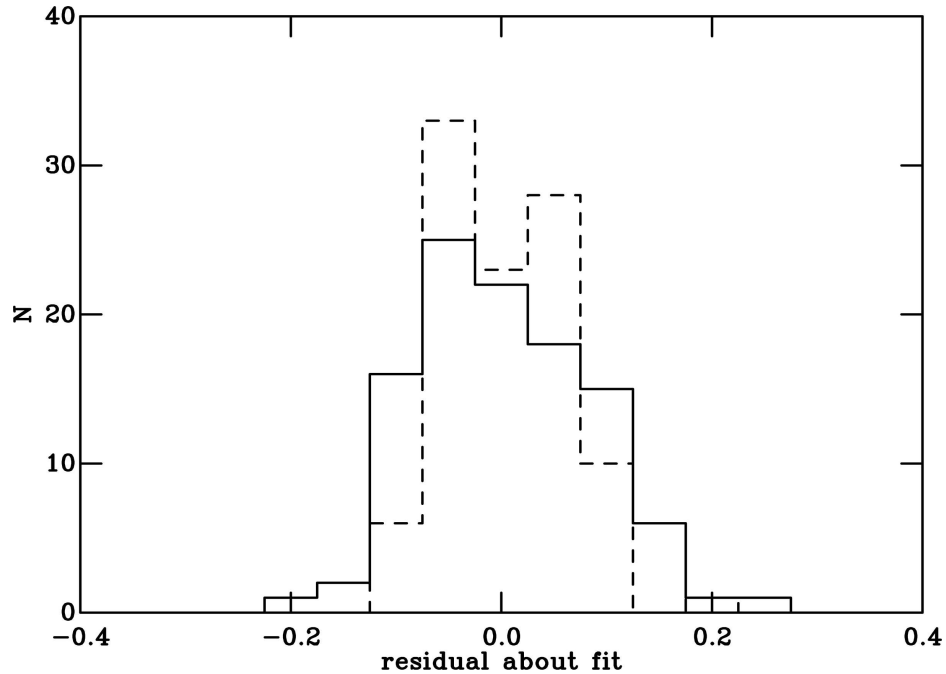


Figure 5.5: Histograms of the residuals in  $R - i'$  about polynomial fits to the observed PMS (solid line) and the simulated PMS (dotted line) for the  $\sigma$  Ori PMS sample (binary fraction 50%).

### 5.3.2 Cep OB3b

In this case we do not have the benefit of such a large spectroscopic sample as in the  $\sigma$  Ori group. As a result, we have no estimate of the likely contamination from field stars, or the true extent of the PMS region in C-M space. There have, however, been a number of studies that have identified likely low-mass members using a variety of techniques. Ogura et al. (2002) used  $H\alpha$  spectroscopy to identify classical T-Tauri stars (CTTSs) in the vicinity of bright rimmed clouds, and found 33 likely members of Cep OB3b, of which 16 are identified in our catalogue. Naylor & Fabian (1999) used ROSAT observations to identify 56 X-ray sources toward Cep OB3b using both HRI and PSPC observations. We have cross correlated their X-ray catalogue with our optical catalogue, matching the brightest star within a radius of  $14''$  for the PSPC positions and  $7''$  for those from

HRI. We find 21 PSPC objects correlate with objects in our catalogue, and 14 HRI objects. We reject all objects that lie in the Galactic background region on the left of the CMD from further use in this study as they are likely non-members (Burningham et al., 2005b), identified by chance correlations with our catalogue. All of these objects were identified by the X-ray study carried out by Naylor & Fabian (1999), which did not correlate optical data with X-ray sources. We accept as likely members those X-ray sources that correlate with objects in the expected PMS region of the  $V_i'$  CMD shown in Figure 5.6. Pozzo et al. (2003) used radial velocities and Li I absorption to identify both CTTSs and Weak T-Tauri stars (WTTSs) in Cep OB3b, and found 5 CTTS members and 5 WTTS members. Of these, all of the CTTSs and all-but-one of the WTTS are found in our catalogue. Pozzo et al. (2003) were also able to rule out membership for a number of objects and these are also indicated on the CMD. Figure 5.6 shows the CMD for the first epoch data, with members from each survey overlaid, along with non-members from Pozzo et al. (2003). Since we are unable to make a reliable PMS selection beyond those members selected by previous authors, we simulate the photometric spread for these 49 likely members. Since more than half our sample has been selected on the basis of X-ray activity, it might be argued that our sample is biased in favour of objects with the greatest rotational variability: WTTSs. On the other hand, WTTS variability is smaller in magnitude than non-periodic CTTS variability. As such, our simulation should still provide an indication of the contribution from variability to the observed spreads.

We have verified the variability of our member sample for Cep OB3b in the same manner as for the  $\sigma$  Ori sample. Figure 5.7 shows the uncertainty in the  $(V - i')$  differences as a function of  $V$  (1st epoch). It is clear that the uncertainties start to increase dramatically fainter than about  $V = 18$ , and step up slightly at brighter than  $V = 13$  for reasons similar to those described in Section 5.3.1. As such we have calculated the RMSs for objects in the range of magnitudes  $14 < V < 17.5$ . The RMS of the differences between the two sets of observations indicates that the likely members are significantly more variable than the rest of the sample. The RMS of the differences in  $V$  are 0.07 for the total sample, compared with 0.11 for the likely members. In  $(V - i')$  the RMSs are smaller: 0.03 for the total sample; 0.07 for the likely members. A similar result is obtained if we attempt to make a photometric PMS selection. This indicates that a high proportion of objects in this region of the CMD may also be PMS members of Cep OB3b.

The member sequence was simulated in the same manner as the PMS sample in the previous

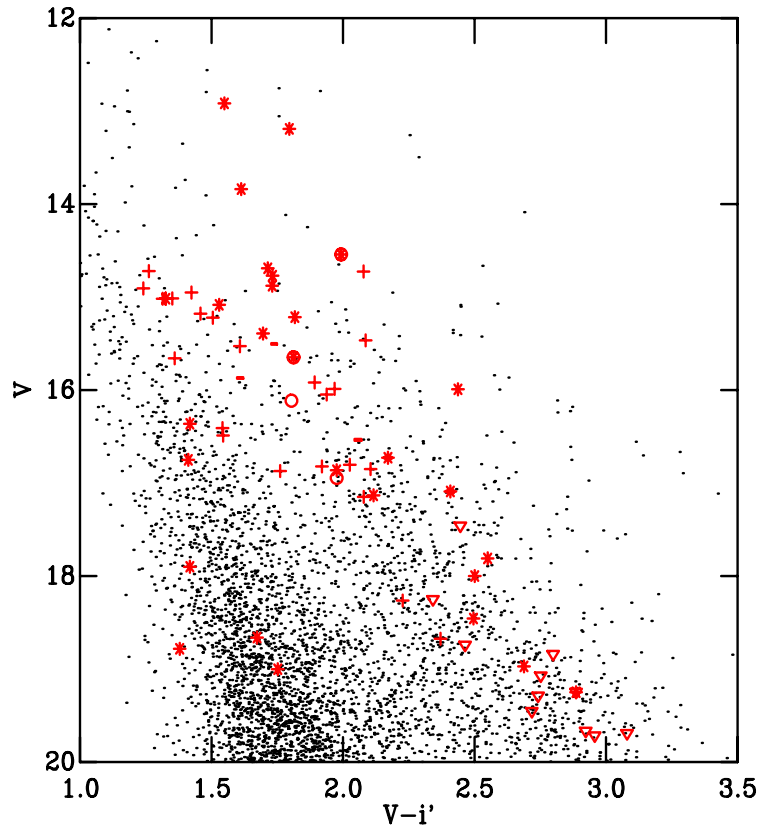


Figure 5.6: The CMD for the 1st epoch Cep OB3b data. Members identified by Ogura et al. (2002) are shown as open triangles, those from Naylor & Fabian (1999) are shown as asterisks, WTTSs from Pozzo et al. (2003) are shown as open circles. Confirmed non-members from Pozzo et al. (2003) are shown as crosses. Those WTTS that were identified in both Naylor & Fabian (1999) and Pozzo et al. (2003) are shown as filled circles. Note the X-ray sources from Naylor & Fabian (1999) that lie in the background region to the left of the CMD. As described in the text, these objects have been excluded from our simulation sample.

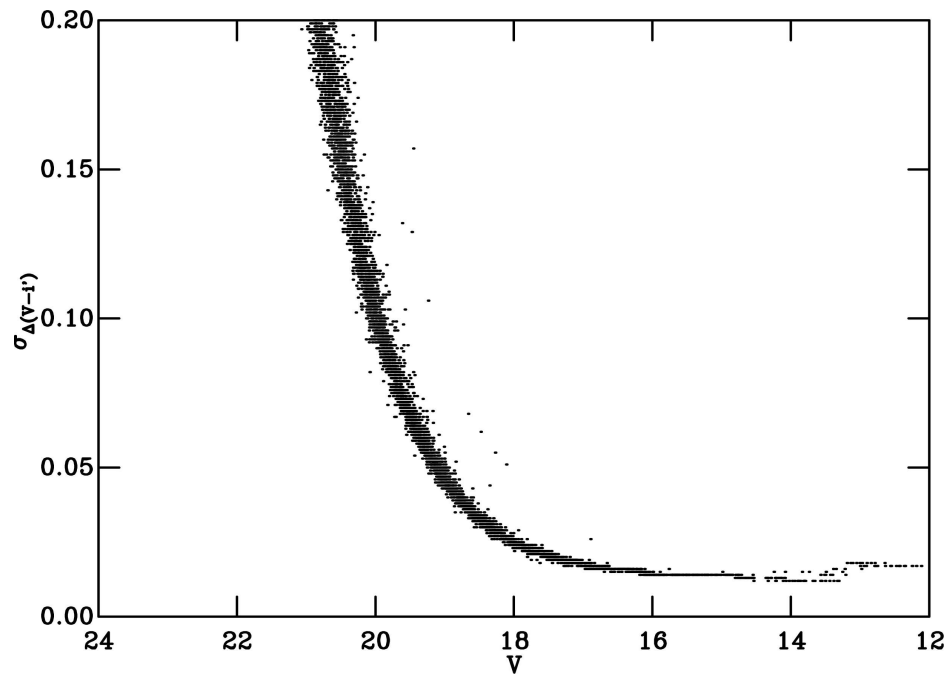


Figure 5.7: A plot of the uncertainty in  $\Delta(V - i')$  against  $V$  for the FoV in Cep OB3b.

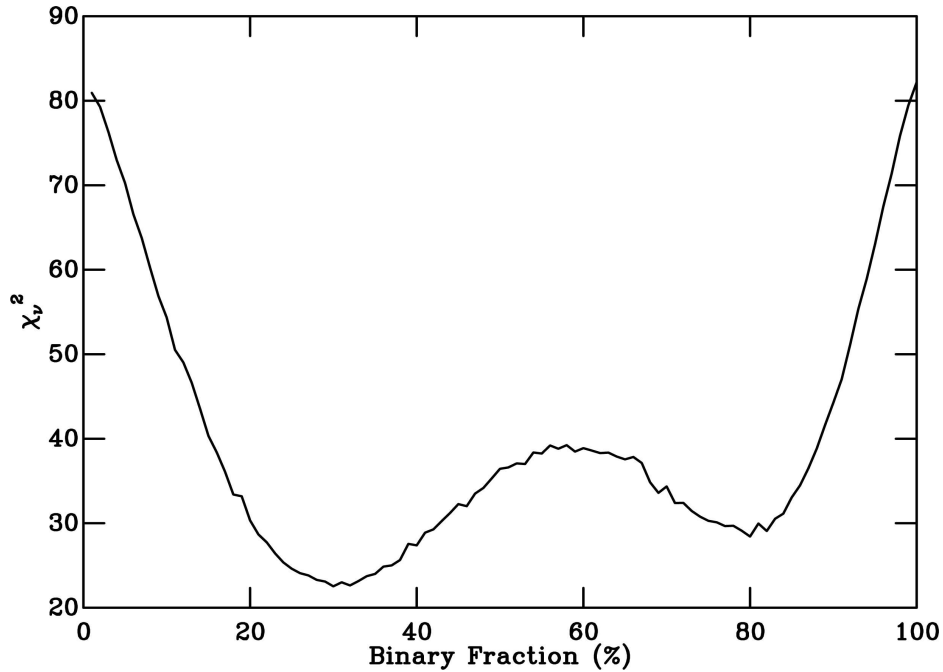


Figure 5.8: The mean  $\chi^2$  for the simulated member sequence compared to the observed member sequence plotted against binary fraction, shown as a percentage for likely members of Cep OB3b.

section. As before, we were able to neglect the effect of differential reddening in our simulation, but for a different reason. Pozzo et al. (2003) found that the reddening vector in a  $V/V - i'$  CMD lies nearly parallel to the PMS for sight-lines toward Cep OB3b. As such the differential reddening is unlikely to add any spread to the observed sequence. The only difference between the two methods is that we have used a different bin size and range when constructing the histograms used for determining  $\chi^2$ . Because the sample size is smaller we used a larger bin width (0.1), whilst extending the range of the bins (-2.0 - +2.0) to include some larger residuals. As can be seen in Figure 5.8, a binary fraction of 25% gives the closest match to the data.

The fitted member sequence for this binary fraction is shown overlaid on CMD (b) in Figure 5.9, whilst the simulated member sequence is shown on CMD (c) of the same figure. In Figure 5.10 we have plotted a histogram of the residuals about the fit to the data and the simu-

lation for the  $14 < V < 17.5$  region of the member sequence for one realisation of the simulation, using a binary fraction of 25%. Inspection of Figures 5.9 and 5.10 indicates that, as was seen in the previous section for the  $\sigma$  Ori young group, the combination of binarity and variability on a timescale of  $\sim 1$  year is not able to explain the spread of members in C-M space.

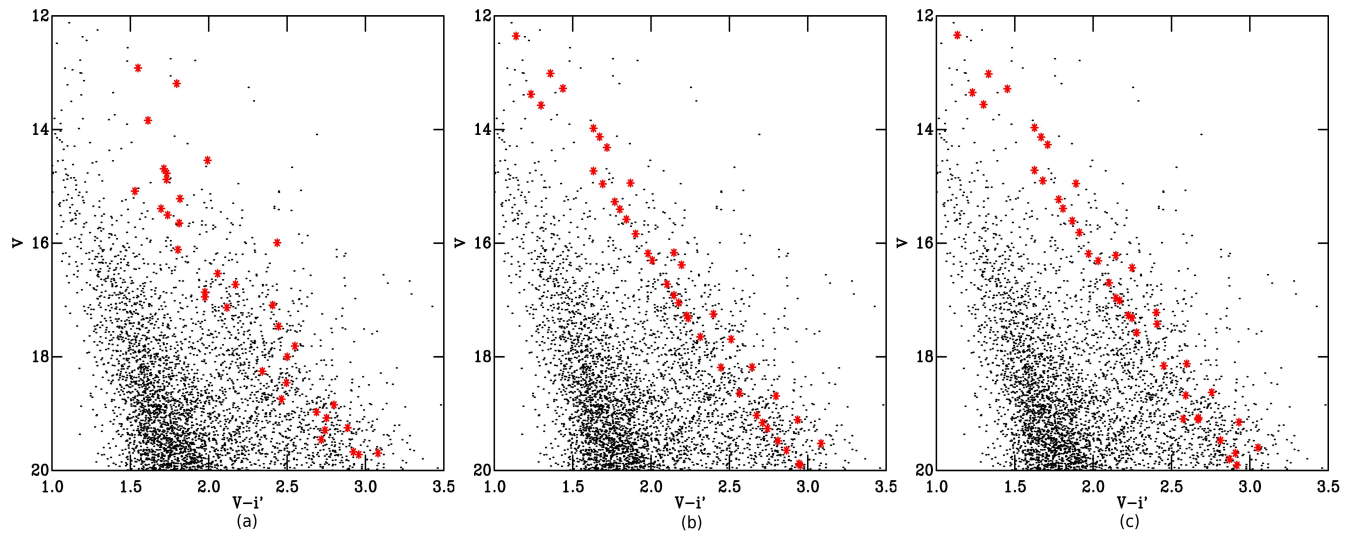


Figure 5.9: A CMD showing the fitted single star and binary member sequences as lines of red asterisks for a binary fraction of 0.25 for the Cep OB3b.

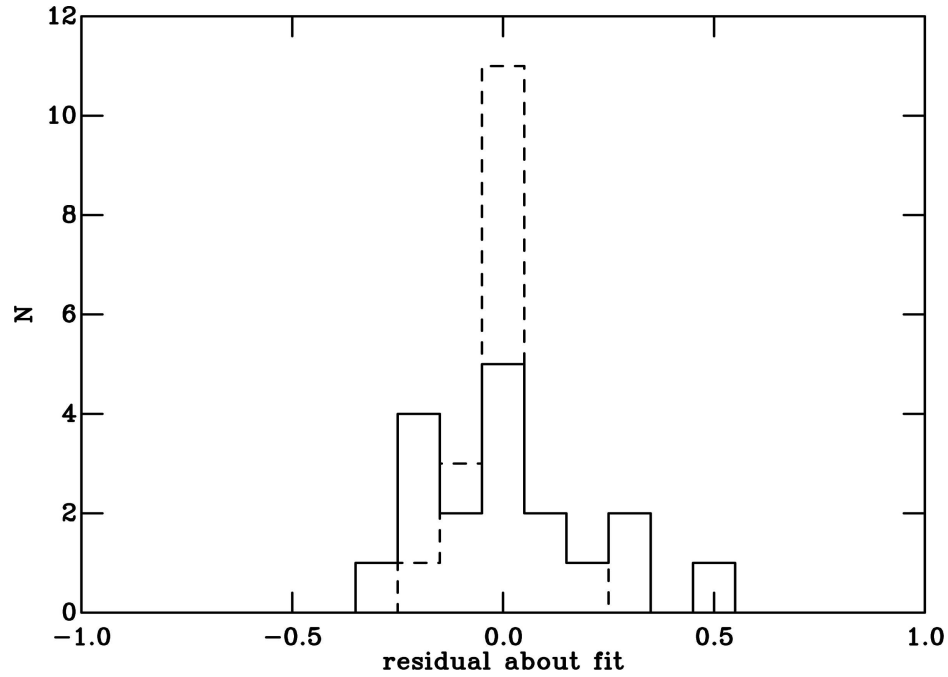


Figure 5.10: Histograms of the residuals in  $V - i'$  about polynomial fits to the observed member sequence (solid line) and the simulated member sequence with a binary fraction of 25% (dotted line) for Cep OB3b.

## 5.4 Discussion

We have shown that photometric variability on timescales of 1-4 years is not able to account for the spread in C-M space occupied by either of our sequences. If we assume that the influence of variability and binarity are added to the underlying distribution in quadrature, we can estimate the proportion of the observed spread that is accounted for here and that which remains unaccounted for. In the case of the  $\sigma$  Ori young group it appears that short term variability can account for about half of the observed spread in  $Ri'$  C-M space. The RMS of the residuals about the polynomial fit is 0.084 mags for the observed PMS, and 0.057 mags for the simulated sequence, which leaves 0.062 mags unaccounted for. Short term variability can only account for about 1/20 of the spread

in Cep OB3b, where the RMSs of the residuals about the polynomial fits are 0.20 mags for the observed member sequence, and 0.075 for the simulated sequence, leaving 0.185 mags unaccounted for.

#### 5.4.1 The nature of the variability

Figures 5.11 and 5.12 show the measured differences in colour and magnitude for the objects in our final sample for each of our regions of interest. The distribution of C-M shifts is clearly different for the two regions, which is not surprising considering the different colours used for each case. The diagonal distribution of the Cep OB3b differences demonstrates that the variability seen here will only tend to move objects up and down an isochrone, and will have little impact on the apparent age spread. These differences, which indicate that objects get bluer when brighter, are consistent with variability arising from hot or cool spots on the surfaces of PMS stars rotating in and out of view. The differences shown in the plot for the  $\sigma$  Ori subgroup display an uncorrelated distribution, which will tend to displace objects across isochrones more. As a result, the simulations carried out for this region display a greater apparent age spread. Since the  $\sigma$  Ori observations are in  $Ri'$ , they are less sensitive to colour changes associated with rotational variability than  $Vi'$  observations (Herbst et al., 1994), and so the different distributions of differences do not necessarily imply a different origin.

Our observations rule out variability on timescales of 1-4 years as the entire cause for the observed C-M spreads. The mechanisms this therefore excludes are rotation of hot or cool spots, and short timescale non-periodic T-Tauri variability, such as that caused by accretion noise or chromospheric flaring. We can also rule out variability associated with rotation of structures in the disc out to a radius of 1 A.U as a source for the C-M spread, since the rotation of such structures should occur within a year. It is also unlikely that rotation of bright structures beyond 1 A.U would be responsible for the C-M spread as the temperature in a thin disc drops rapidly with distance, such that at a radius of 1 A.U the temperature is  $\sim 100$  K. As such the outer disc is only likely to contribute appreciable flux in the far-IR.

The RMS of residuals about the polynomial fit to the simulated PMS is larger in Cep OB3 than the  $\sigma$  Ori young group. Since accreting objects are known to be more variable than non-

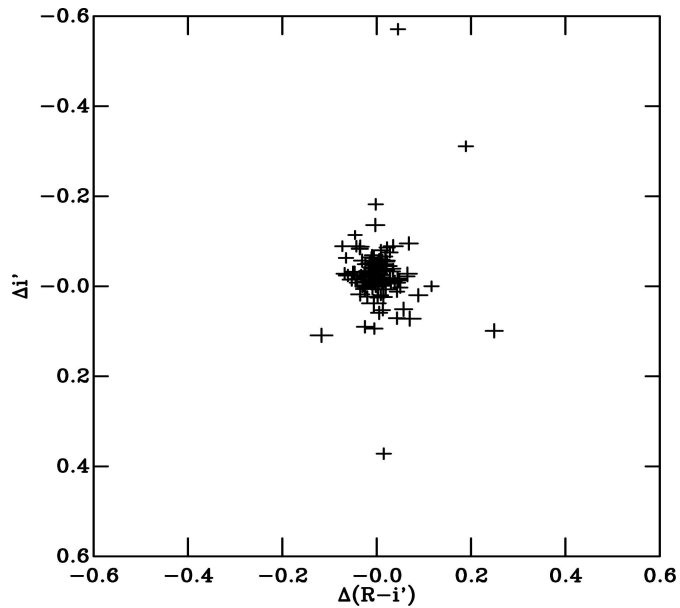


Figure 5.11: A plot of  $\Delta i'$  against  $\Delta(R - i')$  for the  $15 < i' < 18$  region of the PMS in  $\sigma$  Ori. The points are plotted with error bars.

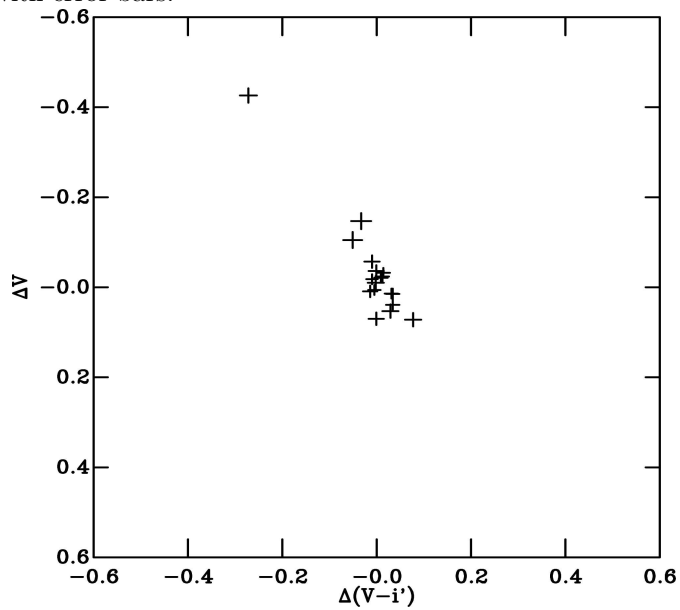


Figure 5.12: A plot of  $\Delta V$  against  $\Delta(V - i')$  for the  $14 < V < 17.5$  region of the member sequence of Cep OB3b. The points are plotted with error bars.

accreting objects, this is consistent with the observed incidence of accretors in the two regions. Kenyon et al. (2005) found the fraction of low-mass accretors to be  $10 \pm 5\%$  in the  $\sigma$  Ori young group, whilst the small number of members identified by Pozzo et al. (2003) in Cep OB3b suggest about 50% of objects there are accretors.

Since longer timescale variability may be the origin of the remaining unexplained spread we cannot confirm the reality of the apparent age spreads. However, what is clear is that the actual size of either age spread is smaller than that observed, and possibly zero. Returning to the RMSs of the residuals about the polynomial fits, we recall that the unaccounted for spread has an RMS of residuals about the fit of 0.062 mags in the case of the  $\sigma$  Ori subgroup, and 0.185 mags in the case of Cep OB3b.

It is tempting read much into the observation that the larger remaining spread is seen in the association whose natal molecular would have had the larger crossing time. However, it should be noted that in the case of the  $\sigma$  Ori subgroup the apparent spread, and thus the underlying one also, may be larger since we were conservative in our PMS selection. As can be seen in Figure 5.1 we have actually excluded some members in order to avoid risking significant contamination by non-members in our photometric selection. The excluded members have the same mean variability as the members that were selected, so the simulated spread has not been altered significantly by their exclusion.

Although we are confident that our selection is not subject to significant contamination (see Burningham et al., 2005b; Kenyon et al., 2005), there will, none-the-less, be some non-members included in the sample. These objects will not increase the size of the observed spread since our confirmed members span the entire selected region of the CMD (see Figure 5.1). However, it is likely that they will reduce the RMS of residuals about the polynomial fit to the simulated spread, as any non-members can be expected to be less variable than the members. If this is the case, then it may still be that the remaining unexplained spread in the  $\sigma$  Ori is very small.

It is still possible that the C-M spreads arise as a result of some other kind of photometric variability. Such variability could arise from variations in accretion flow caused by stellar magnetic cycles (e.g. Armitage, 1995), with time-scales of a few years to decades. Alternatively, much longer time-scale variability such as that resulting from accretion-driven age spreads (ADAS) could be to blame. Fundamentally, the influence of such long term accretion processes on the presence of

apparent age spreads would be best determined through a study of accretion rates across a large number of objects in associations that display a range of apparent spreads, rather than a longer baseline variability study.

### 5.4.2 Apparent age spread and absolute age

As was briefly discussed in Section 5.1.3, the size of age spread inferred from a given photometric spread depends on the median age of the star forming region in question. This should be borne in mind when interpreting any unexplained spread in terms of an age spread. For example, consider the  $\sigma$  Ori young group. If we accept an age of 5 Myrs and a distance of 350 pc, as we did in Chapter 4, then the remaining  $R - i'$  spread of 0.062 mags represents a spread of approximately 4 Myrs (3.5 - 7 Myrs), based on the separation of NextGen isochrones (Chabrier & Baraffe, 1997; Baraffe et al., 2002) at  $i' = 16.5$ . If on the other hand we adopt the age found by Sherry et al. (2004) of 2.5 Myrs and the distance they used for that estimate, 440 pc, we find the remaining ( $R - i'$ ) spread corresponds to an age spread of approximately 2 Myrs (2 - 4 Myrs). Since the degree of age spread permitted in the RSF paradigm is similar to the timescale for star formation, this remaining spread is compatible with that scenario.

In the case of the Cep OB3b association, Pozzo et al. (2003) found the ages of PMS objects to range from  $< 1$  Myr to nearly 10 Myrs using isochrones laid onto a  $V/V - I$  CMD. As has been shown here, variability and binarity can only account for a small fraction of this spread. Such a large remaining spread is hard to reconcile with the RSF paradigm.

## 5.5 Conclusions

We have used 2 epoch, 2 colour photometry to investigate the influence of photometric variability on the apparent age spreads in CMDs. We have found that the combination of binarity and variability on timescales of  $\sim$  years cannot account for the observed spread in C-M space. We argue that the remaining unexplained spread must either reflect a genuine spread of ages, or longer timescale variability associated with the changes in the accretion flow onto the PMS objects.

## 6 Conclusions

### 6.1 Discussion and conclusions

Nearly one hundred years ago the first CMDs and H-R diagrams were plotted. They had an immediate impact on how the evolution of stars was understood. As tools for comparing theory to observation in astrophysics such diagrams are no less important today than they were then. Over the last four chapters the use of CMDs in the study of PMS stellar evolution and star formation has been explored. It has been demonstrated that use their is central to these studies.

In Chapters 2 and 3, X-ray data was used in conjunction with  $VI$  CMDs to identify low-mass PMS stars in an OB association and a young cluster. In the latter of these cases the location and number of PMS stars was used to help resolve a long standing controversy over the nature of Cr 121, confirming its status as a young cluster at a distance of just over 1 kpc, as found by Eggen (1981) and Kaltcheva (2000).

Whilst X-ray selection on CMDs has been shown to be an effective way of identifying PMS stars, it is biased toward selecting X-ray bright objects. As such it cannot be the method of choice when selecting samples for studying fundamental observables of star formation such as the IMF or the existence of age spreads. The investigation detailed in Chapter 4 concluded that selecting samples of PMS objects in OB associations based on their location on a CMD does not exclude significant numbers of bona-fide members. It also confirmed that for  $I < 17$  such selections are not subject to significant contamination by non-members. The work presented in that chapter also highlighted the potential for the use of the 8183, 8195 Å Na I doublet as an unbiased, two pronged, membership diagnostic (radial velocity and surface gravity) for identifying very low-mass objects beyond the lithium burning limit (i.e. for  $M < 0.06M_{\odot}$ ). The use of lithium absorption in combination with radial velocities remains the most efficient and robust method for selecting members within the lithium burning mass range. However, below this range I conclude that observations of the 8183, 8195 Å Na I doublet at sufficient signal-to-noise to measure  $EW(\text{NaI}) < 1 \text{ \AA}$  provide the most robust and efficient diagnostic for young members of OB associations below  $0.06 M_{\odot}$ . Such observations would ideally be carried out using fibre spectroscopy of large numbers of candidate objects, selected from  $V/V - I$  and  $I/R - I$  CMDs, on

an 8 m class telescope. An instrument such as FLAMES on the VLT would be ideal for this kind of work.

In Chapter 5 the work continued to focus on the statistical properties of PMS stars on the CMD: the role of photometric variability in giving rise to apparent age spreads on CMDs for OB associations was investigated. Two epoch optical photometry was used to simulate the spread on CMDs that could be attributed to the combined effects of variability, binaries and photometric uncertainty. Two OB association-like environments were used for this study: the  $\sigma$  Orionis subgroup and a FoV within the Cep OB3b association. It was concluded that the combination of factors accounted for in this experiment could not account for the entire C-M spread in either case. In the case of the  $\sigma$  Orionis subgroup the simulation was able to account for about half the observed spread. The remaining spread in this case is compatible with the rapid star formation paradigm. In the case of Cep OB3b the simulation was only able to account for about one twentieth of the observed spread. The large remaining apparent age spread in Cep OB3b is not consistent with the rapid star formation paradigm.

The projects described in this document have explored the different roles that CMDs can play in the study of star formation and PMS evolution. It has been demonstrated that:

- CMDs provide the ideal observational plane in which to identify PMS objects with the aid of ancillary data;

- the location of PMS objects on CMDs in conjunction with models of PMS evolution can be used to resolve the structural nature of groups along a sight-line;

- photometric sample selection of PMS objects using the  $RI$  CMD for the  $\sigma$  Orionis young group does not exclude significant numbers of bona-fide members;

- at  $I < 17$  ( $M \gtrsim 0.05M_{\odot}$  for an age of 5 Myrs) photometric sample selection using the  $RI$  CMD for the  $\sigma$  Orionis young group is not subject to severe contamination;

- radial velocities measured using the 8183, 8195 Å Na I doublet can provide an unbiased

estimator of both contamination and exclusion in photometric samples;

- apparent age spreads on CMDs for OB associations cannot be accounted for by the combined effects of photometric variability on timescales of 1-4 years, binaries and photometric uncertainty;

## 6.2 Future work

The techniques developed in Chapter 4 for assessing membership of OB associations using the 8183, 8195 Å Na I doublet should be applied to a range of OB associations at a range of galactic longitudes and latitudes to get a broader understanding of how contamination of photometric samples might change with sight-line, and at fainter magnitudes. The samples of low-mass PMS stars obtained as part of such a study would also allow for a study of how luminosity functions (LFs) change with the age of OB associations. This comparison of LFs with age would be a valuable tool for refining PMS models, and would pave the way for more precise estimates of the IMF over a range of environments. I have already obtained a *BVI* imaging survey of over 130 FoVs centred on early-type B-stars, O-stars and WR stars with a view to this task being performed. Approximately 70 FoVs have had a preliminary data reduction carried out, and apparent PMSs are visible on approximately 20 of the CMDs. Recently Tim Naylor and Nathan Mayne obtained fibre spectroscopy of candidate PMS targets in several of these FoVs with a view to confirming their PMS status through lithium absorption and H $\alpha$  emission.

In the near future early releases of the UK infrared deep sky survey (UKIDSS) will become available. This survey will facilitate the identification of candidate low-mass PMS stars and brown dwarfs irrespective of OB association membership. As such it will provide useful incite to the distribution of low-mass objects beyond the usual borders of OB associations, as defined by their higher mass members. One draw back of this kind of survey, however, is the fact that contamination from background giants in the PMS region can be expected to be higher on IR CMDs. Since the portion of UKIDSS which would be of use for this task is restricted to within about a degree of the Galactic plane, it will complement the O-star survey described above excellently. This is because the O-star survey described above avoided precisely this region due to the high level of

extinction frequently found along sight-lines with  $|b| \lesssim 1^\circ$ . It will also allow the identification of more embedded clusters.

Identifying differences in the very low-mass region of the IMF in different environment would be of great importance for constraining theories of star formation. Whilst the O-star survey described above would make a good starting point for searching for such differences, it excludes the lowest mass regions: T associations. The INT/WFC Photometric H-alpha Survey (IPHAS) of the northern Galactic plane will fill this gap. This survey will be particularly sensitive to CTTSs, and can be expected to identify new T-associations. Currently only a handful of T associations are known, so this survey can be expected to greatly increase the sample size for studies of this kind of region.

The conclusion that the apparent age spreads on CMDs of OB associations could not be accounted for by the combined effects of photometric variability, binaries and photometric uncertainty left a number of alternative explanations for the C-M spreads available. One of these was the possibility that the apparent age spread could arise as a result of longer term variability associated with accretion processes, or from a range of accretion rates (and thus luminosities) across the sample of PMS objects. A series of observations to test this possibility has been obtained by Tim Naylor and Nathan Mayne. Measuring the veiling of spectral lines can provide an estimate of the contribution due to accretion flux to an object's magnitude. By assessing if there is a correlation between apparent age spread and scatter of accretion fluxes it will be possible ascertain the importance of this mechanism in producing photometric spreads.

## Bibliography

- Adams F. C., Lada C. J., Shu F. H., 1987, *ApJ*, 312, 788
- Ambartsumian V. A., 1947, *Stellar Evolution and Astrophysics*. Erevan: Acad. Sci. Armenian SSR
- Ambartsumian V. A., 1955, *The Observatory*, 75, 72
- Andre P., Ward-Thompson D., Motte F., 1996, *A&A*, 314, 625
- Appenzeller I., Mundt R., 1989, *A&A Rev.*, 1, 291
- Ardila D., Martín E., Basri G., 2000, *AJ*, 120, 479
- Armitage P. J., 1995, *MNRAS*, 274, 1242
- Béjar V. J. S., Martín E. L., Zapatero Osorio M. R., Rebolo R., Barrado y Navascués D., Bailer-Jones C. A. L., Mundt R., Baraffe I., Chabrier C., Allard F., 2001, *ApJ*, 556, 830
- Béjar V. J. S., Zapatero Osorio M. R., Rebolo R., 1999, *ApJ*, 521, 671
- Ballesteros-Paredes J., Hartmann L., Vázquez-Semadeni E., 1999, *ApJ*, 527, 285
- Baraffe I., Chabrier G., Allard F., Hauschildt P., 2001, in *ASP Conf. Ser. 243: From Darkness to Light: Origin and Evolution of Young Stellar Clusters Pre-Main Sequence Models for Low-Mass Stars and Brown Dwarfs*. pp 571–+
- Baraffe I., Chabrier G., Allard F., Hauschildt P. H., 1998, *A&A*, 337, 403
- Baraffe I., Chabrier G., Allard F., Hauschildt P. H., 2002, *A&A*, 382, 563
- Barrado y Navascués D., Zapatero Osorio M. R., Béjar V. J. S., Rebolo R., Martín E. L., Mundt R., Bailer-Jones C. A. L., 2001, *A&A*, 377, L9
- Barrado y Navascués D., Bouvier J., Stauffer J. R., Lodieu N., McCaughrean M. J., 2002, *A&A*, 395, 813
- Basri G., 2000, *ARA&A*, 38, 485
- Beekman G., Somers M., Naylor T., Hellier C., 2000, *MNRAS*, 318, 9

- Bessell M. S., Castelli F., Plez B., 1998, *A&A*, 333, 231
- Bethe H. A., 1939, *Physical Review*, 55, 434
- Blaauw A., 1952, *Bull. Astron. Inst. Netherlands*, 11, 405
- Bohr N., 1913, *Philosophical Magazine*, 26, 9
- Briceño C., Luhman K. L., Hartmann L., Stauffer J. R., Kirkpatrick J. D., 2002, *ApJ*, 580, 317
- Brown A. G. A., de Geus E. J., de Zeeuw P. T., 1994, *A&A*, 289, 101
- Burgasser A. J., Reid I. N., Siegler N., Close L., Allen P., Lowrance P., Gizis J., 2006, *ArXiv Astrophysics e-prints*
- Burningham B., Naylor T., Jeffries R. D., Devey C. R., 2003, *MNRAS*, 346, 1143
- Burningham B., Naylor T., Littlefair S. P., Jeffries R. D., 2005a, *MNRAS*, 363, 1389
- Burningham B., Naylor T., Littlefair S. P., Jeffries R. D., 2005b, *MNRAS*, 356, 1583
- Cabrit S., Edwards S., Strom S. E., Strom K. M., 1990, *ApJ*, 354, 687
- Chabrier G., Baraffe I., 1997, *A&A*, 327, 1039
- Chabrier G., Baraffe I., Allard F., Hauschildt P., 2000, *ApJ*, 542, 464
- Collinder P., 1931, *Annals of the Observatory of Lund*, 2, 1
- Costado M. T., Béjar V. J. S., Caballero J. A., Rebolo R., Acosta-Pulido J., Manchado A., 2005, *A&A*, 443, 1021
- D'Antona F., Mazzitelli I., 1994, *ApJS*, 90, 467
- D'Antona F., Mazzitelli I., 1997, *Mem. Soc. Astron. Ital.*, 68, 807
- de Zeeuw P. T., Hoogerwerf R., de Bruijne J. H. J., Brown A. G. A., Blaauw A., 1999, *AJ*, 117, 354
- DeGioia-Eastwood K., Throop H., Walker G., Cudworth K. M., 2001, *ApJ*, 549, 578

- Delfosse X., Forveille T., Perrier C., Mayor M., 1998, *A&A*, 331, 581
- Dias W. S., Alessi B. S., Moitinho A., Lépine J. R. D., 2002, *A&A*, 389, 871
- Dias W. S., Lépine J. R. D., Alessi B. S., 2001, *A&A*, 376, 441
- Dolan C. J., Mathieu R. D., 1999, *AJ*, 118, 2409
- Dolan C. J., Mathieu R. D., 2001, *AJ*, 121, 2124
- Eddington A. S., 1924, *MNRAS*, 84, 308
- Edwards S., Hartigan P., Ghandour L., Andrulis C., 1994, *AJ*, 108, 1056
- Eggen O. J., 1981, *ApJ*, 247, 507
- Elmegreen B. G., 2000, *ApJ*, 530, 277
- Feigelson E. D., Casanova S., Montmerle T., Guibert J., 1993, *ApJ*, 416, 623
- Feigelson E. D., Gaffney J. A., Garmire G., Hillenbrand L. A., Townsley L., 2003, *ApJ*, 584, 911
- Feigelson E. D., Montmerle T., 1999, *ARA&A*, 37, 363
- Feinstein A., 1967, *ApJ*, 149, 107
- Flaccomio E., Micela G., Sciortino S., Damiani F., Favata F., Harnden F. R., Schachter J., 2000, *A&A*, 355, 651
- Flower P. J., 1996, *ApJ*, 469, 355
- Garmany C. D., Conti P. S., Chiosi C., 1982, *ApJ*, 263, 777
- Ghez A. M., Neugebauer G., Matthews K., 1993, *AJ*, 106, 2005
- Goldberg D., Mazeh T., Latham D. W., 2003, *ApJ*, 591, 397
- Gorlova N. I., Meyer M. R., Rieke G. H., Liebert J., 2003, *ApJ*, 593, 1074
- Greene T. P., Meyer M. R., 1995, *ApJ*, 450, 233
- Hambly N. C., Davenhall A. C., Irwin M. J., MacGillivray H. T., 2001, *MNRAS*, 326, 1315

- Hambly N. C., MacGillivray H. T., Read M. A., Tritton S. B., Thomson E. B., Kelly B. D., Morgan D. H., Smith R. E., Driver S. P., Williamson J., Parker Q. A., Hawkins M. R. S., Williams P. M., Lawrence A., 2001, MNRAS, 326, 1279
- Hamilton C. M., Herbst W., Shih C., Ferro A. J., 2001, ApJ, 554, L201
- Hartigan P., Strom K. M., Strom S. E., 1994, ApJ, 427, 961
- Hartmann L., 2001, AJ, 121, 1030
- Hartmann L., 2003, ApJ, 585, 398
- Hartmann L., Ballesteros-Paredes J., Bergin E. A., 2001, ApJ, 562, 852
- Hartmann L., Kenyon S. J., 1985, ApJ, 299, 462
- Hartmann L., Kenyon S. J., 1987, ApJ, 312, 243
- Hartmann L., Kenyon S. J., 1996, ARA&A, 34, 207
- Herbig G. H., 1977, ApJ, 214, 747
- Herbst W., Herbst D. K., Grossman E. J., Weinstein D., 1994, AJ, 108, 1906
- Herbst W., Miller D. P., 1982, AJ, 87, 1478
- Herbst W., Shevchenko V. S., 1999, AJ, 118, 1043
- Hertzsprung E., 1911, Publikationen des Astrophysikalischen Observatoriums zu Potsdam, 63
- Hertzsprung E., 1922, Annalen van de Sterrewacht te Leiden, 14
- Hertzsprung E., 1923, Bull. Astron. Inst. Netherlands, 2, 15
- Hillenbrand L. A., 2003, ArXiv Astrophysics e-prints
- Ibragimov M. A., 1997, Astronomy Letters, 23, 103
- Jeffries R. D., Oliveira J. M., 2005, MNRAS, 358, 13
- Jeffries R. D., Thurston M. R., Hambly N. C., 2001, A&A, 375, 863

- Jeffries R. D., Tolley A. J., 1998, MNRAS, 300, 331
- Jessop N. E., Ward-Thompson D., 2000, MNRAS, 311, 63
- Jijina J., Myers P. C., Adams F. C., 1999, ApJS, 125, 161
- Kaltcheva N. T., 2000, MNRAS, 318, 1023
- Kastner J. H., Crigger L., Rich M., Weintraub D. A., 2003, ApJ, 585, 878
- Kendall T. R., Bouvier J., Moraux E., James D. J., Ménard F., 2005, A&A, 434, 939
- Kenyon M. J., Jeffries R. D., Naylor T., Oliveira J. M., Maxted P. F. L., 2005, MNRAS, 356, 89
- Kenyon S. J., Hartmann L., 1995, ApJS, 101, 117
- Kenyon S. J., Hartmann L., Hewett R., 1988, ApJ, 325, 231
- Kenyon S. J., Hartmann L. W., 1990, ApJ, 349, 197
- Knobloch E., Rosner R., Weiss N. O., 1981, MNRAS, 197, 45P
- Kraus A. L., White R. J., Hillenbrand L. A., 2005, ApJ, 633, 452
- Kroupa P., 2001, MNRAS, 322, 231
- Kuiper G. P., 1937, ApJ, 86, 176
- Lada C. J., Muench A. A., Haisch K. E., Lada E. A., Alves J. F., Tollestrup E. V., Willner S. P., 2000, AJ, 120, 3162
- Lada C. J., Wilking B. A., 1984, ApJ, 287, 610
- Landolt A. U., 1992, AJ, 104, 340
- Larson R. B., 1969, MNRAS, 145, 271
- Lee T. A., 1968, ApJ, 152, 913
- Leggett S. K., Allard F., Berriman G., Dahn C. C., Hauschildt P. H., 1996, ApJS, 104, 117

- Leinert C., Zinnecker H., Weitzel N., Christou J., Ridgway S. T., Jameson R., Haas M., Lenzen R., 1993, *A&A*, 278, 129
- Lewis J. R., 1996, *WYFFOS Data Reduction Manual*. Royal Greenwich Observatory, Madingley Road, Cambridge CB3 0HJ
- Littlefair S. P., Naylor T., Burningham B., Jeffries R. D., 2005, *MNRAS*, 358, 341
- Littlefair S. P., Naylor T., Harries T. J., Retter A., O'Toole S., 2004, *MNRAS*, 347, 937
- Lockyer J. N., 1878a, *Proceedings of the Royal Society of London*, 28, 432
- Lockyer J. N., 1878b, *Proceedings of the Royal Society of London*, 28, 283
- Lockyer J. N., 1887, *Proceedings of the Royal Society of London*, 43, 117
- Lodieu N., McCaughrean M. J., Barrado Y Navascués D., Bouvier J., Stauffer J. R., 2005, *A&A*, 436, 853
- Lucas P. W., Roche P. F., 2000, *MNRAS*, 314, 858
- Luhman K. L., Rieke G. H., Young E. T., Cotera A. S., Chen H., Rieke M. J., Schneider G., Thompson R. I., 2000, *ApJ*, 540, 1016
- Mac Low M., Klessen R. S., 2004, *Reviews of Modern Physics*, 76, 125
- Makidon R. B., Rebull L. M., Strom S. E., Adams M. T., Patten B. M., 2004, *AJ*, 127, 2228
- Martín E. L., Delfosse X., Guieu S., 2004, *AJ*, 127, 449
- Mathieu R. D., 1992, in Kondo Y., Sistero R., Polidan R. S., eds, *IAU Symp. 151: Evolutionary Processes in Interacting Binary Stars Disks in the Pre-Main Sequence Binary Environment*. pp 21–+
- Mathieu R. D., 1994, *ARA&A*, 32, 465
- Melnik A. M., Efremov Y. N., 1997, *VizieR Online Data Catalog*, 902, 10013
- Mihalas D., Dappen W., Hummer D. G., 1988, *ApJ*, 331, 815

- Mohanty S., Basri G., Jayawardhana R., Allard F., Hauschildt P., Ardila D., 2004, ArXiv Astrophysics e-prints
- Monck W. H. S., 1892, AJ, 12, 147
- Monck W. H. S., 1898, ApJ, 8, 28
- Monck W. L. S., 1895, The Journal of the British Astronomical Association, 5, 418
- Montmerle T., Koch-Miramond L., Falgarone E., Grindlay J. E., 1983, ApJ, 269, 182
- Moraux E., Bouvier J., Stauffer J. R., Cuillandre J.-C., 2003, A&A, 400, 891
- Muench A. A., Lada E. A., Lada C. J., Alves J., 2002, ApJ, 573, 366
- Muzerolle J., Calvet N., Hartmann L., 1998, ApJ, 492, 743
- Muzerolle J., Hillenbrand L., Calvet N., Briceño C., Hartmann L., 2003, ApJ, 592, 266
- Naylor T., 1998, MNRAS, 296, 339
- Naylor T., Fabian A. C., 1999, MNRAS, 302, 714
- Naylor T., Totten E. J., Jeffries R. D., Pozzo M., Devey C. R., Thompson S. A., 2002, MNRAS, 335, 291
- Neuhaeuser R., Sterzik M. F., Torres G., Martin E. L., 1995, A&A, 299, L13+
- Nielsen A. V., 1963, Centaurus, 9, 219
- North J., 1994, The fontana history of astronomy and cosmology. London : Fontana Press, 1994.
- Ogura K., Sugitani K., Pickles A., 2002, AJ, 123, 2597
- Palla F., Stahler S. W., 2000, ApJ, 540, 255
- Palla F., Stahler S. W., 2002, ApJ, 581, 1194
- Payne C. H., 1925, Proceedings of the National Academy of Science, 11, 192

- Perryman M. A. C., Lindegren L., Kovalevsky J., Hoeg E., Bastian U., Bernacca P. L., Cr ez e M., Donati F., Grenon M., van Leeuwen F., van der Marel H., Mignard F., Murray C. A., Le Poole R. S., and 5 other authors 1997, *A&A*, 323, L49
- Pozzo M., Jeffries R. D., Naylor T., Totten E. J., Harmer S., Kenyon M., 2000, *MNRAS*, 313, L23
- Pozzo M., Naylor T., Jeffries R. D., Drew J. E., 2003, *MNRAS*, 341, 805
- Preibisch T., Brown A. G. A., Bridges T., Guenther E., Zinnecker H., 2002, *AJ*, 124, 404
- Preibisch T., Feigelson E. D., 2005, *ApJS*, 160, 390
- Preibisch T., Kim Y.-C., Favata F., Feigelson E. D., Flaccomio E., Getman K., Micela G., Sciortino S., Stassun K., Stelzer B., Zinnecker H., 2005, *ApJS*, 160, 401
- Preibisch T., Zinnecker H., 1999, *AJ*, 117, 2381
- Preibisch T., Zinnecker H., Herbig G. H., 1996, *A&A*, 310, 456
- Pringle J. E., Allen R. J., Lubow S. H., 2001, *MNRAS*, 327, 663
- Reid I. N., Kirkpatrick J. D., Liebert J., Burrows A., Gizis J. E., Burgasser A., Dahn C. C., Monet D., Cutri R., Beichman C. A., Skrutskie M., 1999, *ApJ*, 521, 613
- Reid I. N., Kirkpatrick J. D., Liebert J., Gizis J. E., Dahn C. C., Monet D. G., 2002, *AJ*, 124, 519
- Reipurth B., Zinnecker H., 1993, *A&A*, 278, 81
- Ritter A., 1883, *Wiedemann's Annalen Phys. Chemie*, 20, 137
- Ritter A., 1898, *ApJ*, 8, 293
- Rogers F. J., Swenson F. J., Iglesias C. A., 1996, *ApJ*, 456, 902
- Russell H. N., 1910, *AJ*, 26, 147
- Russell H. N., 1913, *The Observatory*, 36, 324
- Russell H. N., 1914, *The Observatory*, 37, 165
- Russell H. N., 1929, *ApJ*, 70, 11

- Russell H. N., Adams W. S., Joy A. H., 1923, *PASP*, 35, 189
- Salpeter E. E., 1955, *ApJ*, 121, 161
- Saumon D., Chabrier G., van Horn H. M., 1995, *ApJS*, 99, 713
- Saxton R. D., Ashley J., Vallance R., 2000, *ASTERIX Data Analysis, User Note 005*. School of Physics and Astronomy, Birmingham University
- Schiavon R. P., Barbuy B., Rossi S. C. F., Milone A., 1997, *ApJ*, 479, 902
- Schönberg M., Chandrasekhar S., 1942, *ApJ*, 96, 161
- Shapley H., 1913, *ApJ*, 38, 158
- Shapley H., 1917a, *ApJ*, 45, 118
- Shapley H., 1917b, *ApJ*, 45, 164
- Sherry W. H., Walter F. M., Wolk S. J., 2004, *AJ*, 128, 2316
- Shu F. H., 1977, *ApJ*, 214, 488
- Shu F. H., Adams F. C., Lizano S., 1987, *ARA&A*, 25, 23
- Siess L., Dufour E., Forestini M., 2000, *A&A*, 358, 593
- Siess L., Forestini M., Dougados C., 1997, *A&A*, 324, 556
- Skinner S. L., Zhekov S. A., Güdel M., Schmutz W., 2002, *ApJ*, 579, 764
- Stahler S. W., Palla F., 2004, *The formation of stars*. The formation of stars, by S.W. Stahler and F. Palla. New York, NY: Wiley, 2004
- Stassun K. G., Ardila D. R., Barsony M., Basri G., Mathieu R. D., 2004, *AJ*, 127, 3537
- Strom K. M., Strom S. E., 1994, *ApJ*, 424, 237
- Strömngren B., 1932, *Zeitschrift für Astrophysics*, 4, 118
- Strömngren B., 1933, *Zeitschrift für Astrophysics*, 7, 222

- Sung H., Bessell M. S., Lee S., 1998, *AJ*, 115, 734
- Tassis K., Mouschovias T. C., 2004, *ApJ*, 616, 283
- Tassoul J., Tassoul M., 2004, *A concise history of solar and stellar physics. A concise history of solar and stellar physics*, by Jean-Louis Tassoul and Monique Tassoul. Princeton, NJ: Princeton University Press, 2004
- Tinney C. G., Reid I. N., 1998, *MNRAS*, 301, 1031
- Tout C. A., Livio M., Bonnell I. A., 1999, *MNRAS*, 310, 360
- Trumpler R. J., 1925, *PASP*, 37, 307
- Trumpler R. J., 1930, *Lick Observatory Bulletin*, 14, 154
- Walker M. F., 1956, *ApJS*, 2, 365
- Ward-Thompson D., Andre P., Scott P. F., Hills R. E., 1997, in *IAU Symp. 182: Herbig-Haro Flows and the Birth of Stars Vol. 182, ISOPHOT observations of a pre-stellar core*. pp 257P+
- Ward-Thompson D., Motte F., Andre P., 1999, *MNRAS*, 305, 143
- Ward-Thompson D., Scott P. F., Hills R. E., Andre P., 1994, *MNRAS*, 268, 276
- Warren W. H., Hesser J. E., 1978, *ApJS*, 36, 497
- Waterfield R. L., 1956, *The Journal of the British Astronomical Association*, 67, 1
- Wilson R. E., 1953, *Carnegie Institute Washington D.C. Publication*, pp 0–+
- Wolk S. J., 1996, *Ph.D. Thesis*
- Wood J. H., Naylor T., Hassall B. J. M., Ramseyer T. F., 1995, *MNRAS*, 273, 772
- Wyse R. F. G., Gilmore G., 1992, *MNRAS*, 257, 1
- Zapatero Osorio M. R., Béjar V. J. S., Pavlenko Y., Rebolo R., Allende Prieto C., Martín E. L., García López R. J., 2002, *A&A*, 384, 937